

Ultrafast Dynamics of Nanoparticles in Highly Intense X-Ray Pulses

vorgelegt von

M. Sc.

Maximilian Jakob Bucher

geb. in Frankfurt am Main

von der Fakultät II - Mathematik und Naturwissenschaften
der Technischen Universität Berlin
zur Erlangung des akademischen Grades

Doktor der Naturwissenschaften

- Dr. rer. nat. -

genehmigte Dissertation

Promotionsausschuss:

Vorsitzender: TBA

Berichter/Gutachter: Prof. Dr. Thomas Möller

Berichter/Gutachter: TBA

Tag der wissenschaftlichen Aussprache: TBA

Berlin 2017

Maximilian Jakob Bucher

Argonne National Laboratory

Chemical Sciences and Engineering Division

Argonne, IL 60439, United States

SLAC National Accelerator Laboratory

Linac Coherent Light Source

Menlo Park, CA 94025, United States

Technische Universität Berlin

Institut für Optik und Atomare Physik

10623 Berlin, Germany

E-Mail: max@max-bucher.de

Web: <https://www.max-bucher.de>

This document is written in \LaTeX and \BibTeX using the KOMA-Script class. It was electronically compiled on 2017-01-29 using pdf \LaTeX and biber via MiKTeX 2016, TeXnicCenter, and SumatraPDF.

This work is licensed under a Creative Commons “Attribution 4.0 International” license.



More information can be found under

<https://creativecommons.org/licenses/by/4.0/deed.en>

Abstract

With the advent of lightsources of the fourth generation, such as the X-ray free electron laser (XFEL) the Linac Coherent Light Source (LCLS), structural studies on non-repetitive and non-reproducible nanoparticles such as single biomolecules appear imminent. A key challenge to increasing the resolution of single particle imaging is radiation damage. Only a sound understanding of the underlying damage processes, such as the nanoplasma phase transition, can overcome this challenge and will ultimately lead to higher resolutions. Sacrificial tamper layers have been proposed to slow sample damage but this has not been shown experimentally in aerosol nanoparticles.

This work investigates the nanoplasma transition in superfluid He-, bulk Xe- and mixed HeXe-clusters using an ultrafast, XFEL accelerator-based X-ray pump–X-ray probe technique. A first X-ray pulse triggers the nanoplasma transition in the sample at intensities of $\sim 10^{17} \text{ W cm}^{-2}$, and a second X-ray pulse probes the system at a later time, Δt , at power densities of $\sim 10^{18} \text{ W cm}^{-2}$. The delay Δt is varied from (0 to 800) fs delay. The probe creates a diffraction image of the (~ 30 to ~ 1000) nm sized objects and coincidentally ions are captured via time-of-flight (TOF) spectroscopy. He- and Xe-clusters are generated through a supersonic gas expansion into a vacuum. Mixed HeXe-clusters are created when He-droplets pick up Xe-atoms in a doping unit.

The study reveals single-shot snapshots of Xe-, He- and HeXe-clusters that undergo the nanoplasma phase transition. The reconstruction of a ~ 25 nm radius Xe-cluster with ~ 6 nm is shown. A large-scale structural analysis of the size and number of scatterers in Xe-clusters show a rapidly expanding particle, thus structural damage. Expansion speeds and electron temperatures of the superheated nanoplasma are derived and compared to IR pump–X-ray probe studies. TOF spectroscopy reveals a time delay Δt dependent ionization pattern in Xe-atoms and HeXe-clusters, while pristine He-droplets do not exhibit this dependency. The structural analysis of few hundred nanometer radius HeXe-clusters show that the doped Xe-atoms arrange in small clusters of a plum-pudding type. The He-droplet acts thereby as a shell and the Xe-clusters as a sample. The X-ray pump–X-ray probe study on HeXe-clusters shows structural damage in the He-droplet, while Xe-clusters do not show structural damage 800 fs after the pump-pulse. Sample damage in pristine He-droplets is found and compared to Xe- and HeXe-clusters.

Contents

1. Introduction	1
2. Fundamental Concepts	4
2.1. Why X-ray free electron lasers?	4
2.1.1. From bending magnets to undulators	6
2.1.2. Self-amplification by spontaneous emission	8
2.1.3. Soft X-ray self-seeding	11
2.1.4. Novel X-ray pump–X-ray probe techniques	13
2.2. Rare-gas clusters	17
2.2.1. Generation of homogenous clusters	17
2.2.2. Creation of heterogeneous clusters: The pickup principle	22
2.3. Fundamental processes of soft X-rays and nanoparticles	24
2.3.1. Photoionization and core-hole decay	26
2.3.2. From Thomson scattering to diffractive imaging	30
2.3.3. Generalized index of refraction	34
2.4. Clusters in intense X-ray pulses	36
2.4.1. Formation and expansion of a nanoplasma	36
2.4.2. Sacrificial layers slow the nanoplasma expansion	40
3. Experimental Considerations	44
3.1. The X-ray beam transport to the LAMP end-station	45
3.2. The LAMP end-station at the AMO instrument	47
3.3. The large area pnCCD detectors	51
3.4. Sample delivery	54
3.4.1. Sample jet timing at LCLS	56
3.5. Time-of-flight mass-spectrometer	59
3.6. Focus characterization	62
3.6.1. Focus characterization using a TOF spectrometer	62
3.6.2. Focus characterization via imprint study	62

4. Methods	65
4.1. The computing environment at LCLS	65
4.2. pnCCD photon detectors	67
4.2.1. Combining multiple pnCCD detectors	69
4.2.2. Impact of the X-ray pump–X-ray probe on diffraction pattern	71
4.3. Phase retrieval from a single diffraction pattern	74
4.3.1. Principle of phase retrieval	75
4.3.2. 2D reconstructions and image resolution	76
4.3.3. 1D projections and phase reconstructions	80
4.4. 2D electron density and diffraction image simulations	80
4.5. Acqiris data sampling considerations	83
4.6. Data filtering	85
5. Results and discussion	87
5.1. Structural damage in Xe-clusters induced by intense X-rays	87
5.2. Time-dependent response of Xe-atoms due to an X-ray pump–probe beam	94
5.3. Time-resolved response of highly ionized He- and HeXe-clusters	95
5.4. Condensation of xenon in helium cluster: Plum-pudding type cluster	98
5.5. Understanding structural damage in the plum-pudding type clusters	103
5.6. Sacrificial layers: Comparison of structural damage in He- and HeXe-cluster	105
6. Summary and outlook	108
7. Appendix	110
7.1. Matlab code on spherical integrations	110
7.2. Python code on combining detectors	111
8. Bibliography	114
A. Publikationsliste	A
B. Eidesstattliche Versicherung	C
C. Acknowledgment	D

List of Figures

1.1.	Computer simulations of aluminum spheres with tamper layers	3
2.1.	Aerial view of the Linac Coherent Light Source.	5
2.2.	Schematics of several X-ray generating methods.	7
2.3.	Undulator gain curve correlated to microbunching.	9
2.4.	SASE single-shot and average spectra.	10
2.5.	Schematic setup of soft X-ray self-seeding system.	11
2.6.	Soft X-ray self-seeding spectra and brilliance of various lightsources. . . .	12
2.7.	Schematic setup of an undulator based pump–probe scheme.	15
2.8.	Schematic setup of a bunch based pump-probe setup.	16
2.9.	Schematic of a supersonic gas expansion into a vacuum.	19
2.10.	Schematic of a pickup (gas-)source.	23
2.11.	Total cross-section of atomic carbon.	25
2.12.	Schematic illustration of common charge transfer processes	26
2.13.	Total absorption cross-sections for helium and xenon.	27
2.14.	Fluorescence peaks from xenon and neon K-LL Auger spectrum. . . .	29
2.15.	Principle of scattering rays of an atom.	31
2.16.	Schematic of the nanoplasma creation and expansion.	36
2.17.	Measurement and simulation of the nanoplasma expansion in Xe-clusters. .	39
2.18.	Experiment that shows early evolution of the nanoplasma transition. . . .	40
2.19.	Tamper layers and nanoparticles that undergo a nanoplasma formation. .	42
3.1.	Schematic overview of the AMO beamline instrumentation.	46
3.2.	Overview of the AMO instrument in the LAMP end-station configuration. .	48
3.3.	Inside view of the C1 chamber showcasing the interaction region.	49
3.4.	Rear and front pnCCD detector geometry in the LAMP instrument. . . .	50
3.5.	Geometry of a single pnCCD module.	52
3.6.	Sideview of double sample jet configuration.	54
3.7.	Schematic of the Parker-Hannifin Series 99 valve.	56
3.8.	Schematic of LCLS EVR timing system.	57

3.9.	Event receiver time delay at LCLS for supersonic gas jets.	58
3.10.	Drawing of the time-of-flight spectrometer.	60
3.11.	Sideview of the spectrometer showing ion, electron and photon trajectories. .	61
3.12.	Focal spot analysis using a time-of-flight ion spectrometer.	62
3.13.	Focal spot analysis via an ex-situ microscope imprint study.	63
4.1.	Diagram of the computing environment at LCLS and DAQ traffic.	66
4.2.	ADU histograms from electronic noise of unilluminated pnCCDs.	68
4.3.	Front and rear pnCCD arranged to combine measured diffraction image. .	72
4.4.	Spherical projection of 2D diffraction image onto 1D.	73
4.5.	Influence of X-ray pump–X-ray probe study in diffraction image.	73
4.6.	Example of a phase retrieval algorithm.	75
4.7.	Illustration of resolution enhancement and diffraction image cropping. .	78
4.8.	Used electron densities in 2D real and Fourier space simulations. . . .	81
4.9.	Comparison of analytical derived scattering and numerical simulations. .	82
4.10.	First data point in Acqiris sampling.	83
4.11.	Using light peak to find absolute time zero in Acqiris traces.	84
4.12.	Average cluster size correlated to measured intensity on front pnCCD. .	85
5.1.	Single Xe-cluster size distribution at varying time delay Δt	88
5.2.	Time-resolved behavior of number of scatterers due to nanoplasma expansion	89
5.3.	Single-shot 2D reconstructions of ~ 25 nm radius Xe-clusters.	90
5.4.	Single-shot 1D reconstruction of ~ 30 nm radius Xe-cluster	91
5.5.	Recovered Amplitudes $ A $ and phase factor of 1D reconstruction	92
5.6.	Single-shot diffraction pattern of Xe-cluster at varying time delays . . .	93
5.7.	Time-resolved answer of atomic xenon in TOF spectroscopy.	94
5.8.	Time-resolved answer of He-clusters in TOF spectroscopy.	95
5.9.	TOF spectra of HeXe-clusters with $\sim 0.6\%$ Xe-doping at various delays Δt . .	96
5.10.	TOF spectra of HeXe-clusters with $\sim 0.06\%$ Xe-doping at various delays. .	98
5.11.	Reconstruction of HeXe-clusters and simulated electron densities.	99
5.12.	Hypothetical arrangement of Xe-clusters within He-droplets.	100
5.13.	Simulated structural damage scenarios in HeXe-clusters.	102
5.14.	Simulation and exp. data: Structural damage in He-droplet.	104
5.15.	Single-shot diffraction images of He-droplets at different time delays . .	105
5.16.	Single-shot diffraction patterns of HeXe-cluster at different time delays .	106

List of Tables

2.1.	Parameter K_{gas} values for rare-gases.	21
2.2.	Differential absorption cross-sections and ionization potentials for xenon. .	27
2.3.	Absorption cross-sections and ionization potentials for xenon and helium .	28
2.4.	Atomic scattering factors for helium and xenon.	33
3.1.	Summary of LCLS beam parameters during experiment.	47
3.2.	pnCCD gain modes and typical ADU values at 1k eV photons.	53
3.3.	Installed vacuum pumps in the experiment.	55
3.4.	Applied voltages to the time-of-flight spectrometer (ion side use only). .	61
4.1.	Typical parameters used in the Hawk software package.	77
5.1.	Relative comparison of measured scattering versus expected scattering. .	106

1. Introduction

Following the discovery of *X-radiation* at the end of the 19th century by Röntgen [1], X-rays have been used to understand and investigate matter in unprecedented ways. Soon after this discovery, X-rays were used to take the first medical image. Later, X-rays lead to the understanding of fundamental aspects of atoms [2] and crystals [3, 4]. Today, the success story continues in various fields of science. A large and active scientific field is structural biology. Here, X-rays are being used to study the structure of proteins through crystallography. Proteins are the so-called “workhorse” in the human body and the structure of a protein defines its biological function. Unfortunately not all proteins can be grown into large crystals making the molecular structure determination challenging. However, new lightsources, namely *X-ray free electron lasers* (XFELs) [5] have more and more peak *brightness* allowing the structure determination of smaller and smaller protein-crystals [6].

The first hard XFEL was built at Stanford University and is called the Linac Coherent Light Source (LCLS) [7]. It is a multikilometer long machine that produces X-rays with wavelengths from (4.6 to 0.1) nm, has intensities of up to $\sim 10^{18}$ W cm⁻², and has ultra-short pulses ranging from (1 to 500) fs. Scientists from various disciplines can apply to use this lightsource for their experiments that are conducted in several instruments. The Atomic, Molecular, and Optical (AMO) physics instrument at LCLS was the first of seven instruments in operation and is a focal point for experiments ranging from biological imaging to basic science [8].

The beam parameters that are available at the AMO instrument opened up an entirely new method for structural biologists, which is the *single particle imaging* (SPI). With SPI, the shape of single bio-molecules can be determined through *diffractive imaging* [9]. First experiments have successfully delivered single-shot diffraction images of biological particles, such as viruses [10] and non-biological particles, such as rare-gas clusters [11]. It has been a rapidly developing field that has recently succeeded in visualizing 3D images of nano-objects [12, 13].

1. Introduction

But the highly-intense pulses that enable diffractive imaging lead to unusual questions. When an intense soft X-ray pulse irradiates a nanoparticle, the particle will simultaneously absorb and diffract X-rays with the absorption cross-section being much larger than the scattering cross-section. From the first moment of light-matter interaction, the absorption will lead to inner atomic-shell vacancies [14] and these vacancies make the above cross-sections time-dependent. Subsequent ionization cascades, such as the *Auger-decay*, occur only a few femtoseconds later and the nanoparticle is thus transformed into a nanoplasma on the femtosecond timescale. Several forces will expand the plasma [15] until eventually, the nanoplasma disintegrates into its atomic components.

The underlying principle of diffractive imaging, which is that intense X-ray pulses diffract from a single macromolecular structure before they destroy it, is now challenging since sample damages occur while the pulse propagates through the nanoparticle. Changing scattering factors and trapped, delocalized electrons will affect the diffraction image. While diffractive imaging is still feasible, these reasons will limit the achievable resolution in single particle imaging. Several ideas have been proposed to address radiation damage. Computer models can account for known processes [16]; molecule alignment prior imaging provides additional information [17]; and sacrificial tamper layers can compensate for radiation damage processes [18, 19]. While experimental data exists for the first two ideas, sacrificial tamper layers that are placed around aerosol injected particles have until now not been studied experimentally and are in focus of this work.

Sacrificial tamper layers supply electrons to the photoionized sample and transport kinetic energy away from the sample. This delays the nanoplasma expansion of the sample (see Figure 1.1). An effective tamper layer would ideally be thin and uniform around the sample to minimize its background signal. A first idea of a tamper layer is water, since bio-molecules typically have a water-based layer when injected into the imaging setup via an aerosol gas jet. However, water-based layers become disordered in thicker layers and are usually uneven around macro-molecules [20]. An alternative are helium-based layers, where, for example, a sample particle is placed inside a helium-droplet.

This thesis discusses experimental data of sacrificial tamper layers, which are in form of a helium-droplet, that has been placed around xenon-clusters, which represent the aerosol sample. The data is complemented by the study of pristine Xe- and He-clusters. A novel *X-ray pump–X-ray probe* method was employed to study the nanoplasma formation in those samples. Here, the pump-pulse triggers the nanoplasma formation and

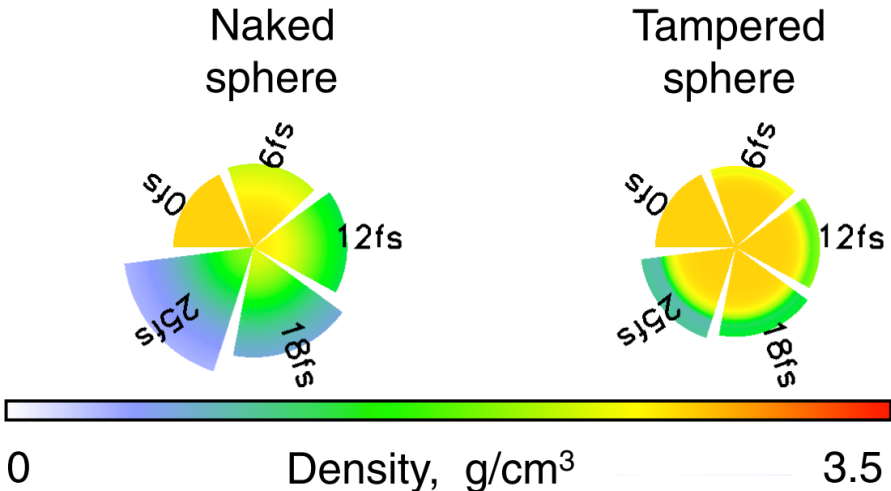


Figure 1.1.: Computer simulations of 7.5 nm radius aluminum spheres that are illuminated by intense soft X-rays with a fluence of $2.5 \cdot 10^8 \text{ J cm}^{-2}$. On the left is a pristine Al-sphere and on the right is a Al-sphere with a 2.5 nm thick silicon tamper layer. From [19]. Reprinted with permission from APS.

the probe-pulse creates a “snapshot” at a later time. Coincident diffraction imaging and time-of-flight mass spectroscopy data is measured and further analyzed with phase-retrieval algorithms to yield real-space images of single, aerosol nanoparticles with thus far unprecedented resolution. This analysis answers the following questions:

- How does an X-ray induced nanoplasma-transition affect Xe-clusters?
- How do mixed HeXe-clusters self-organize as nanoparticles?
- Does helium compare to sacrificial tamper layers in mixed HeXe-clusters?

This document is organized as follows. Chapter 2 discusses fundamental aspects that are used throughout this study; Chapter 3 describes the experimental setup at the AMO instrument at LCLS and in particular the LAMP end-station with its detectors; Chapter 4 discusses several computational methods. Chapter 5 presents the results of the pump-probe study; and Chapter 6 summarizes the present work and provides an outlook for further studies.

2. Fundamental Concepts

This chapter condenses the theoretical concepts that will reoccur throughout this thesis. The chapter starts off in Section 2.1 with an introduction to the key aspects of X-ray free electron lasers (XFEL), including the beam operating modes *self-amplified spontaneous emission* (SASE), *self-seeding* and *multipulse* operations. Section 2.2 is about the formation of rare-gas clusters via supersonic jets and pickup sources. We then dive into the interaction of light and matter in Section 2.3 that discusses coherent, elastic X-ray scattering, and inelastic processes in atoms. The chapter ends with Section 2.4, describing the nanoplasma formation in pristine cluster and core-shell systems.

2.1. Why X-ray free electron lasers?

X-rays were first created through *Bremsstrahlung*, where an electron beam with kinetic energies of (0.1 to 100) keV hit a block of copper and the deceleration of electrons in the copper led to the creation of X-rays. Since then, there has been tremendous progress in the creation of X-rays. For scientific purposes, X-rays are commonly created in X-ray synchrotron lightsources and are often referred to as “synchrotron facility”. In a synchrotron facility, electrons are produced in bursts by an *electron gun* and formed to a collimated *electron bunch*. Then, these electrons are accelerated near the speed of light, with kinetic energies, γ , of $\gamma >$ MeV, and injected into a *synchrotron* that keeps the kinetic energy of the electrons constant. In a synchrotron, the electrons are deflected by bending magnets to travel around a closed-loop path. The deflection of the electrons at the bending magnet leads to the emission of X-rays. Typically, electrons are bunched together to increase the amount of emitted photons and a storage ring can store many electron bunches allowing a high repetition rate of light pulses on the order of megahertz. The X-ray pulses are characterized through a parameter that is called spectral brightness [21] or sometimes brilliance. We can define the spectral brightness as [22]

$$B = \frac{n}{A \Theta \Delta E}, \quad (2.1)$$

2.1. Why X-ray free electron lasers?



Figure 2.1.: Aerial view of the Linac Coherent Light Source (LCLS). LCLS uses the last third of the SLAC Linear Accelerator but is overall a multikilometer long machine. The accelerator and buildings are stretched far because of the light generation process. From [23]

with n being the number of photons per second, A the source area, Θ the divergence of the beam, and ΔE being the spectral bandwidth of the light pulse. The spectral brightness is an overall measure of the quality of a light source. The development of modern synchrotron light sources is hence often measured and compared to previously achieved brightness values. The motivation to improve the peak brightness is manifold and follows the recipe to let a sample interact with as many photons possible, in the shortest time possible, and with the best energy resolution possible. In other words, higher peak brightness light sources enable imaging of even smaller particles, or investigate dynamics that are even faster.

To get a numerical understanding, let us look at non-linear absorption dynamics in atoms and molecules. One can conservatively estimate that a typical absorption cross section for soft X-rays¹ is around $\sigma = 1$ megabarn (Mb) [24]. Typical X-ray focii² are $A = 1 \mu\text{m}^2$ such that the number of photons, n_{in} , needed to absorb just one photon per atom, n_{abs} , is

$$n_{in} = \frac{n_{abs}A}{\sigma} = \frac{10^{-8} \frac{\text{cm}^2}{\text{sr}}}{10^{-18} \frac{\text{cm}^2}{\text{Mb}}} = 10^{10} \quad \text{photons.} \quad (2.2)$$

We can compare this to a modern synchrotron source, e.g., NSLS-II. This synchrotron facility produces $1.7 \cdot 10^4$ photons per pulse in the Si(111) bandwidth at pulse durations of a few tens of picoseconds [25]. That is far out of reach for investigating non-linear, or multi-photon, processes. While this back of the envelope type of calculation might be

¹Soft X-rays have wavelengths of (10 to ~ 0.2) nm

²The focus size at the AMO instrument of LCLS is $1 \mu\text{m}^2$.

2. Fundamental Concepts

off by an order of magnitude or so depending on the specific case, it illustrates the order of magnitude improvement scientists were looking for to unravel entirely new aspects of X-ray science. As it is not possible to use conventional optical methods to increase the number of X-ray photons, drastic ideas were needed. In the 1970’s, it was first discussed in Reference [26] to achieve coherent radiation in the ultraviolet to X-ray region. Later, it was proposed to build free electron laser [27, 28] and the Section 2.1.2 discusses the laser-like radiation of these lightsources.

Construction of the first hard XFEL finished in 2009 and it is called the Linac Coherent Light Source. LCLS can be seen from a birds-eye view in Figure 2.1. LCLS is able to create $\sim 10^{12}$ photons per pulse and achieves pulse-lengths of a few femtoseconds. The beam parameters of XFELs increased the peak brightness that is available at user facilities by many orders of magnitude³. This allows the study of, for example, the ultrafast movement of electrons in chemical reactions [29, 30], the imaging of nanoparticles [6, 10] and the discussed nonlinear dynamics of atoms, molecules, and clusters [14, 31–33].

Only a few XFEL exist today. The LCLS at SLAC National Accelerator Laboratory (SLAC) in the United States and the SACLAC at Rikagaku Kenkyūsho (RIKEN) in Japan are the two currently operating XFEL user-facilities. More XFELs are being built around the world, for example, the European XFEL near Deutsches Elektron Synchrotron (DESY) in Germany, the SwissFEL at Paul Scherrer Institut (PSI) in Switzerland, and the PAL-XFEL at Pohang Accelerator Laboratory (PAL) in South Korea.

2.1.1. From bending magnets to undulators

In the beginning of X-ray synchrotron lightsources, the radiation was generated using *bending magnets*. A bunch of electrons was accelerated near the speed of light and traversed a bending magnet. The deflection from the bending magnet resulted in the emission of electro-magnetic radiation. A schematic setup of a bending magnet can be seen in Figure 2.2. The first improvement to creating X-rays over bending magnet sources was through a *wiggler*. Wigglers consist of magnets arranged in an alternating order. An electron bunch traveling through a wiggler is “wiggled” along its path due to magnetic fields, which causes the particles to emit radiation. Although wigglers are

Wigglers can be considered as a series of bending magnets, which is why the total

³See Figure 2.6 for an illustration of the improvement in peak brightness.

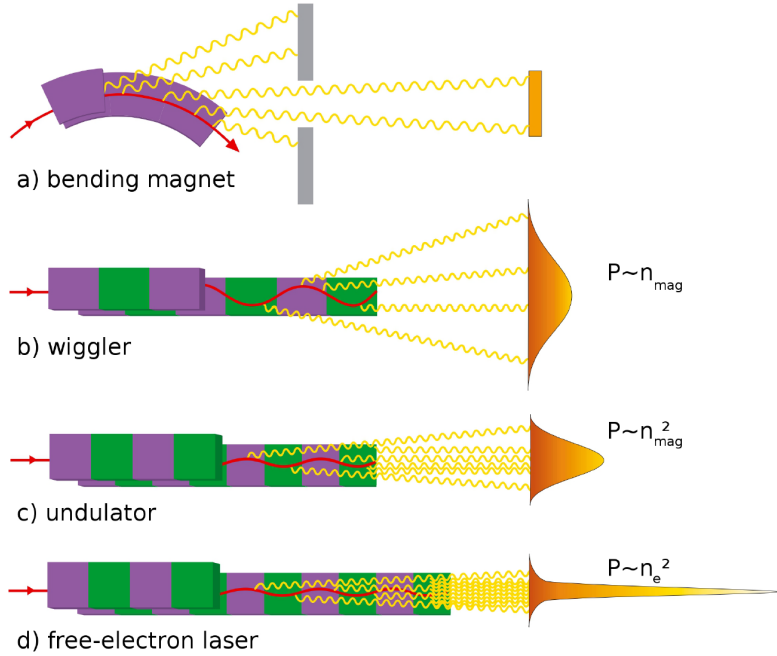


Figure 2.2.: Schematics of several X-ray generating methods. The red lines are pathways of the electron beams and the yellow lines represent emitted X-rays. The emitted spatial power distribution is orange. From [34, CC BY-SA].

emitted power, P , is proportional to the number of magnets, n_{mag} , [35]

$$P \propto n_{\text{mag}}, \quad \text{in a wiggler magnet.} \quad (2.3)$$

The emitted radiation has a broad, continuous spectrum and the center of that spectrum can be controlled by changing the speed, or kinetic energy, of the electron bunch. For X-rays, wigglers were first used by the Hamburger Synchrotronstrahlungslabor (HASYLAB) at DESY and the Stanford Synchrotron Radiation Lightsource (SSRL) at SLAC in the late 1970's to early 80's. Independently from wigglers, undulators were developed [36]. Wigglers and undulators create radiation on the same principle: an electron bunch is accelerated near the speed of light and then forced on a sinusoidal pathway. In undulators, the separation of magnets is specific and named undulator period, λ_U . Although, undulator magnets are large constructs of a few meters and their undulator period is on the order of centimeters, traversing electrons emit radiation on the nanometer wavelength range. This is due to relativistic effects. In the frame of the electrons, the undulator period, λ_U , appears shorter. It is now useful to characterize undulators and wigglers by

2. Fundamental Concepts

the strength parameter, K , which is given by, [37]

$$K = \frac{e B_{\max} \lambda_U}{2\pi m_e c}, \quad (2.4)$$

with e being the elementary charge, B_{\max} being the maximum magnetic field in the undulator or wiggler, m_e being the mass of an electron and c being the speed of light, we can write in convenient units

$$K \approx 0.934 B_{\max} \lambda_U \quad [\text{T cm}]. \quad (2.5)$$

Undulators typically have $K < 1 \text{ T cm}$ and wiggler $K \gg 1 \text{ T cm}$. The X-rays emitted by undulators typically have a narrower spectrum and a higher flux than wigglers. This is due to the fact that in an undulator, the undulator period and magnetic fields are chosen such that their emitted radiation per period constructively interfere with each other. This resonant condition is expressed by the fundamental wavelength of an undulator, λ_r , and can be noted as [37]

$$\lambda_r = \frac{\lambda_U}{2\gamma} \left(1 + \frac{K^2}{2} + \gamma^2 \Psi^2 \right), \quad (2.6)$$

with the Lorentz factor γ of the electron bunch in the undulator and the electron observation angle, Ψ . As a result, the emitted power, P , now scales as [38]

$$P \propto n_{\text{mag}}^2, \quad \text{in an undulator magnet.} \quad (2.7)$$

2.1.2. Self-amplification by spontaneous emission

If an electron bunch travels through just one undulator, the emitted power scales linearly with the number of electrons, n_e , which is due to the finite size and randomly distributed density of an electron bunch. If the electrons emit light from the same point or are separated by $n \cdot \lambda_r$, with $n = (1, 2, 3, \dots)$, the emitted photons would constructively interfere and be coherent. XFELs use the idea to emit light from the same point to generate their light pulses and they achieve that by *microbunching* their electron bunches. Microbunching can be achieved in a straight and long undulator section⁴, where multiple undulators are connected in series. The process is illustrated in Figure 2.3. As the electron bunch travels in vacuum through the long XFEL undulator section, light will always be faster than electrons. This slight velocity difference means that the co-propagating photons and electrons have a phase difference and interact with each other. Depending on the

⁴LCLS has a 112 m long undulator section.

2.1. Why X-ray free electron lasers?

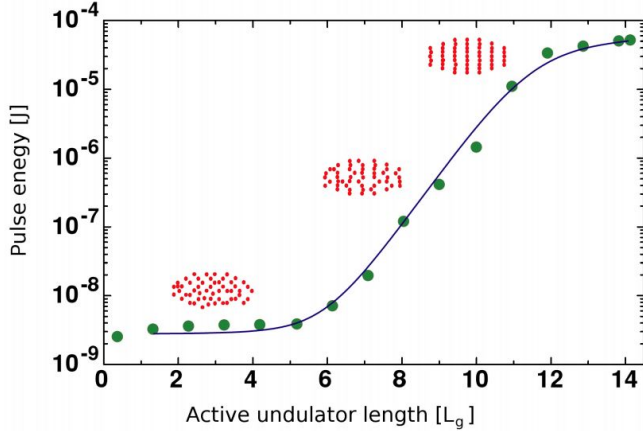


Figure 2.3.: Undulator gain curve correlated to microbunching. The X-ray pulse energy is plotted logarithmically over the undulator length L_g (blue curve, green dots) and shows an exponential growth until saturation. The electron bunch (red dots) starts with a random density distribution. As the bunch travels through the undulator, its density is modulated periodically such that the electrons microbunch. Upon optimal *microbunching*, the X-ray lasing process saturates. From [34, 39]

phase, an electron will either gain or lose velocity. As a result, the initial uniform electron density is periodically modulated by the photon-field as it travels through the undulators of an XFEL. The modulated electron bunch structure is called microbunching.

The structure of the microbunching can be characterized further. Due to the velocity mismatch, the photon-field travels $\lambda_r(\Psi = 0)$ (see Equation 2.6) more than the electron bunch over each undulator period. This is also referred to as *slippage*. As a result, the electron bunch becomes increasingly structured and eventually there is a spacing between dense areas (see Figure 2.3). This spacing is $\lambda_r(\Psi = 0)$. As the electron bunch becomes structured, it amplifies a narrower wavelength bandwidth around $\lambda_r(\Psi = 0)$ through spontaneous emission. The number of electrons that are in phase with the photons increases over the travel length through the undulator and the lasing process saturates when the microbunching is fully developed.

This type of radiation, or XFEL operation mode, is called *Self-Amplification by Spontaneous Emission* (SASE) due to the underlying processes. The emitted power, P , is now not only proportional to the square of the number of undulator magnets, but due to the

2. Fundamental Concepts

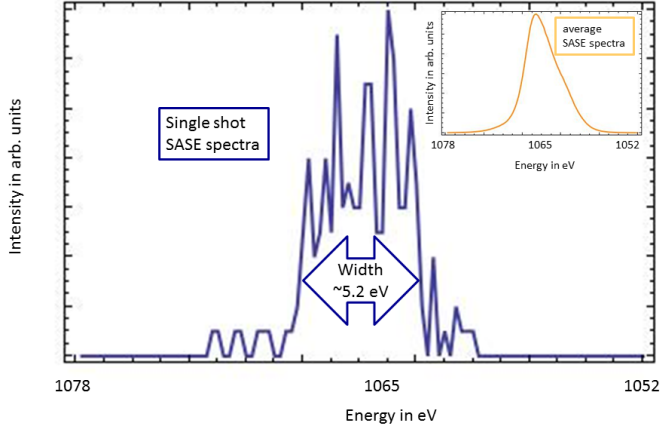


Figure 2.4.: The large blue spectra is a SASE spectra from a single LCLS shot measured with a photoelectron [see 40]. Note the spiky peak structure on a background pedestal. Within the narrow bandwidth of an XFEL pulse some energies are more strongly amplified due to the microbunching. The yellow graph in the inset is an average spectrum of several hundred single-shots and shows a low energy tail, which is due to XFEL-jitter.

photons being in phase, it scales as [22]

$$P \propto n_e^2, \quad \text{in SASE operation.} \quad (2.8)$$

SASE spectra can be seen in Figure 2.4. A SASE spectrum is typically different from shot-to-shot and has distinct peaks on top of a more broad background. This is due to the initially emitted photons that have a pseudo-random wavelength within a narrow bandwidth. The electron-bunch amplifies these specific wavelengths as it travels through the undulators since its microbunching is defined by those specific wavelengths.

The key process in SASE is that an electron bunch interacts with the emitted photon-field. The interaction occurs because the particles have a narrow spatial and kinetic-energy distribution. The average spread of these distributions can be characterized by the so-called *emittance*. Only the linear accelerator components of a free electron laser (FEL) are able to compress an electron bunch in space and energy, i.e., create a low-emittance electron-bunch, such that the electron bunch can interact with the photons and microbunch.

2.1. Why X-ray free electron lasers?

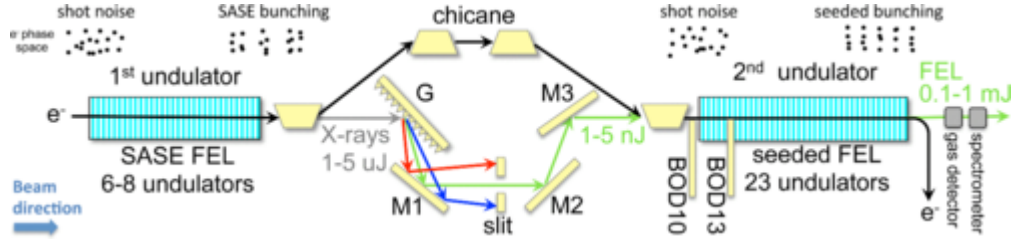


Figure 2.5.: Schematic setup of the soft X-ray self-seeding system at LCLS. From [42]. Reprinted with permission from APS.

At longer wavelength ranges, where efficient optics are readily available, a so-called *multi-pass low-gain* FEL is able to reuse electron-bunches, although the spontaneous emission affects the kinetic energy of the bunch. Without going into much detail, this FEL type leads to comparable high repetition rates and narrow spectra but few photons per pulse [41]. At shorter wavelength ranges, the kinetic energy of an electron bunch is drastically affected due to the spontaneous emission of X-rays. Additionally, there is a lack of efficient optics in the X-ray region. So, XFELs use only one electron-bunch⁵ in a long set of undulators to create one X-ray pulse. This is called a *single-pass high-gain* FEL.

2.1.3. Soft X-ray self-seeding

A special free electron laser (FEL) beam mode is the seeded type. In contrast to the SASE operation, where the initial photons are randomly emitted and further amplified, a seeded FEL starts with a given *seed* of photons. If the set of initial photons is monochromatic, mostly this wavelength is amplified as the bunch travels through the undulator along-side the seed. The initial photon seed can be created through various processes and the wavelength of the photon seed is the critical parameter in determining which method to choose. In the case of the infra-red (IR) to extreme ultra-violet (XUV) wavelength range, conventional lasers can be used to produce the initial photon seed. However, due to the lack of lasers available at X-ray wavelengths, the idea of *self-seeding* is pursued.

Following Figure 2.6, an electron bunch is first sent through a few undulator magnets to generate a few SASE photons, the electrons and photons are then separated using a magnetic chicane, which also neutralizes the microbunching in the electron bunch. The grating monochromator selects a small wavelength slice from the comparably broad SASE spectrum of the initial photons. Photons exiting the monochromator are called the

⁵The European XFEL uses a so-called *bunch train*, where multiple electron bunches are accelerated in series.

2. Fundamental Concepts

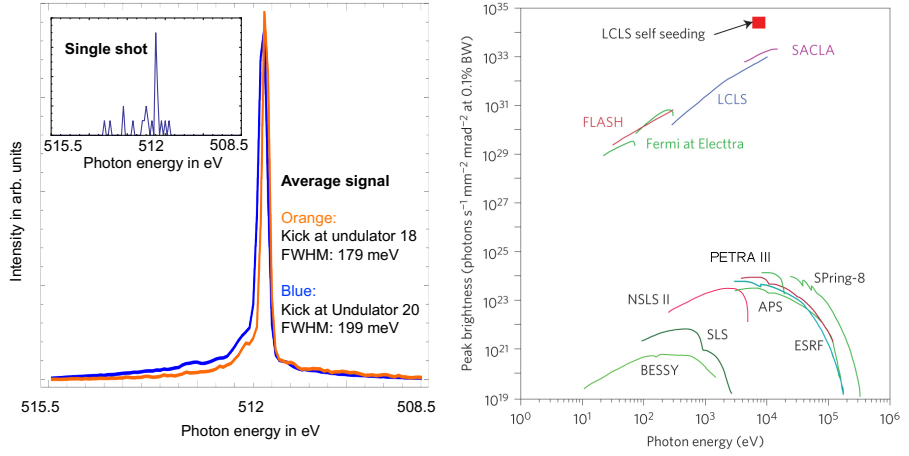


Figure 2.6.: Left, normalized average spectra of soft X-ray self-seeding (SXRSS) operations using the AMO instrument at LCLS [see 40]. The self-seeding spectra is characterized by a sharp spectral peak around a desired energy accompanied by a SASE-radiation-type spectral pedestal. The often undesired SASE pedestal is suppressed, when the electron bunch travel through undulators is shortened. The right image shows the peak spectral brightness of various light sources over a wide photon energy range. SXRSS operations have a spectral brightness that exceeds current SASE FEL sources. Adapted from [43].

2.1. Why X-ray free electron lasers?

seed. The seed and the electron bunch are overlapped again using the magnetic chicane and then sent through more undulators. Here, the seed modulates the electron bunch and thus only a narrow spectral band is amplified. A typical spectrum of a soft X-ray self-seeded beam can be seen in the left panel of Figure 2.6. The characteristics of a self-seeded spectrum are an intense peak at the selected wavelength regime on top of a broad SASE background pedestal. The background is an artifact of the amplification of some spontaneous emission events and can be suppressed by using fewer undulator magnets. Self-seeded beams have a significantly reduced pulse energy – by an order of magnitude, depending on the exact beam parameters – as compared to LCLS SASE operations. However, in their main peak, self-seeded beams have a higher spectral brightness when compared to a SASE beam. Using Equation (2.1), the increase in spectral brightness compared to SASE is understandable and it is illustrated in the right panel of Figure 2.6.

Self-seeded beam operations have recently been demonstrated at LCLS. For hard X-rays, the Hard X-Ray Self-Seeding (HXRSS) instrument uses a diamond crystal to select a wavelength slice [44]. In the case of soft X-rays, the Soft X-ray Self Seeding (SXRSS) instrument uses a grating in a dispersive monochromator [42]. A seeded beam using an external laser to generate photons as an initial seed has been demonstrated at the XUV-FEL FERMI at Ellettra-Sincrotrone (ELETTRA) in Italy [45]. The peak intensity in a narrow spectral band makes seeded beams interesting for a variety of applications, particularly in spectroscopy, where it is instrumental to excite materials with narrow bandwidth photons. There are also applications in atomic and molecular physics, ranging from linear absorption spectroscopy [46], to ultrafast photoemission spectroscopy on molecules [40], to non-linear stimulated Raman spectroscopy [47], to ultra-fast photoemission studies. Particularly interesting for this work is the magnetic chicane from the SXRSS instrument when used as described in the next chapter.

2.1.4. Novel X-ray pump–X-ray probe techniques

Pump–probe experiments are commonly used as they allow a precise study of dynamics. The pump-pulse gives a very controllable starting point, i.e., “time zero” in the dynamic process, and the probe-pulse can perform a measurement at a later time delay, Δt . Sometimes pump- and probe-pulse are switched, which is indicated by a negative time delay to verify time zero, or to probe the system before any dynamics have occurred. It is often desirable to have a pump- and probe-pulse of different wavelength, for example, one can pair an optical laser pulse and an X-ray pulse. However, in order to study X-ray induced phenomena using X-ray imaging and spectroscopy techniques, as it is discussed in this

2. Fundamental Concepts

thesis, two X-ray pulses are needed.

Recently, two methods have been proposed in order to create two X-ray pulses to conduct a X-ray pump–X-ray probe experiment. Method one is a mirror-based beam split-and-delay system (XRSD device) [48–50]. It splits a single pulse into a pump- and probe-pulse and allowing a time delay of the latter. These systems are typically limited to short time delays, as the grazing incidence optics have to fit into existing setups. Method two uses accelerator-based schemes [51, 52] that manipulate electron bunches to create two X-ray pulses. Both methods have been demonstrated at LCLS and have been useful complementing the more widely available optical laser pump–X-ray probe methods, particularly in the chemical sciences [30, 53, 54].

The in this thesis used accelerator-based X-ray pump–X-ray probe method, can also produce two X-ray pulses of different wavelength. These are called “two-color” pump–probe schemes and the generation of two-colored X-ray pulses is currently limited to the parameters of Equation (2.6). The equation indicates possibly two schemes. One, the undulator parameter, K , can be tuned to change the emitted wavelength; and two, the Lorentz factor, γ , can be different if there are two electron bunches. As the accelerator-based X-ray pump–X-ray probe method has been used in the present work, let us describe these schemes in greater detail.

Undulator parameter- K based pump–probe schemes

The first developed accelerator based X-ray pump–X-ray probe technique at LCLS [51] uses a difference in undulator parameters, $K_{1,2}$, to create two pulses of different wavelength. The time delay is introduced through a magnetic chicane.

A schematic setup is shown in Figure 2.7. Following the figure to the top panel (a) Scheme I, one electron bunch is created through a single slotted foil⁶. The use of the slotted foil enables control over the pulse duration. The electron bunch then travels through the undulator section U_1 tuned at strength parameter K_1 and is stimulated deep into the lasing process, but the lasing does not go into saturation such that the electron bunch can be reused in the second undulator section. A magnetic chicane removes the microbunching from the section U_1 such that in undulator section U_2 , tuned to undulator strength

⁶A single slotted foil or emittance-spoiling foil is typically inserted in a magnetic chicane. Here, it spoils the electron bunch by Coulomb scattering them leaving only a certain energy band of the electron bunch that is within the slot unspoiled. This usually narrows the electron beam and thus reduces its pulse duration [55].

2.1. Why X-ray free electron lasers?

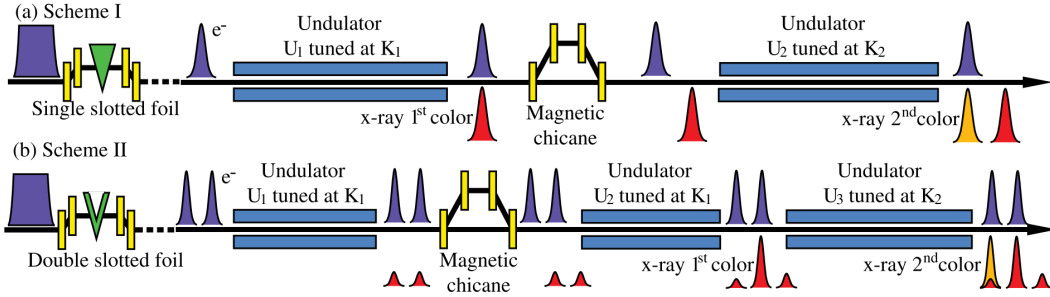


Figure 2.7.: Schematic setup of undulator parameter-K based pump–probe schemes at LCLS. In (a) Scheme I, one creates a single electron bunch using a single slotted foil. (b) Scheme II, one creates a double electron bunch using a double slotted foil. The electron bunches emit radiation with a wavelength depending on $K_{1,2}$. A time delay Δt between pulses is introduced using a magnetic chicane. From [51]. Reprinted with permission from APS.

parameter K_2 , the electron bunch lases again and the process is able to saturate. The maximal color separation between the two pulses is 1.9 % in relative difference between K_1 and K_2 .

The time delay between the two pulses is introduced by a magnetic chicane that extends the pathway of the electrons and leaves photons unaffected. At LCLS, a dedicated chicane, for example, from the soft X-ray self-seeding instrument, can reach delays up to a maximum of 800 fs. In this scheme, several factors prevent a minimal time delay, Δt_{\min} , of zero. The minimal time delay opposed by the magnetic chicane, τ_{\min} , is dictated by the electron drift velocity mismatch to the speed of light. We can express that as,

$$\tau_{\min} = \frac{l}{v_{\text{drift}}} - \frac{l}{c} \approx 50 \text{ as}, \quad (2.9)$$

with $l \approx 4 \text{ m}$ being the length between undulator sections U_1 and U_2 , c being the speed of light, and v_{drift} being the drift velocity of the electron bunch. As the electron bunch drifts undeflected through the chicane close to the speed of light τ_{\min} is typically on the tens of attoseconds timescale. There is also a timing jitter between the two light pulses that is introduced by the magnetic chicane due to the magnetic field jitter and the electron beam energy jitter. The total contribution to the timing jitter is less than 0.4 % of the time delay imposed by the chicane. So, the delay chicane does not significantly contribute to the delay Δt_{\min} . A bigger factor is the velocity mismatch of the light pulse and the electron bunch as they travel through a undulator section. This mismatch can

2. Fundamental Concepts

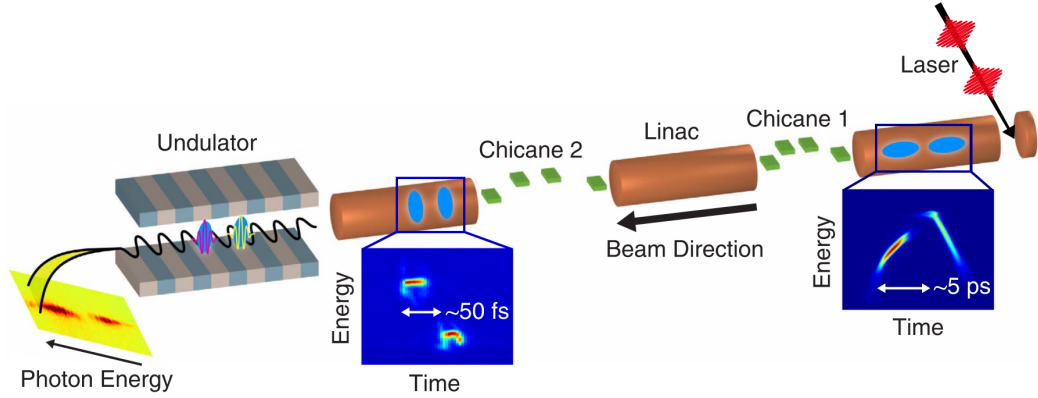


Figure 2.8.: Schematic setup of the two bunch, two color pump–probe setup at LCLS. Two laser pulses shot at a cathode create two electron bunches with a delay Δt on the picosecond timescale. Two magnetic chicanes compress the bunches such that a delay Δt is on the ten femtosecond timescale. Both pulses go through one undulator section and the lasing process is saturated. The relative color separation is on the order of 1 % between the bunches. From [52,].

be estimated by

$$\Delta t_{\min} - \tau_{\min} = \frac{N_u \lambda_r}{c}, \quad (2.10)$$

with N_u being the undulator periods. Given the parameters in study [51], $\Delta t_{\min} = 3$ fs, such that a partial overlap between the electron bunch and light pulse could be achieved after the magnetic chicane. It should be noted that this scheme has been used in the described experiment.

The Twin-bunch or Lorentz factor based pump–probe scheme

The second developed accelerator-based X-ray pump-X-ray probe technique at LCLS [52] uses two electron bunches of different energy. A schematic setup of this beam operation can be found in Figure 2.8. The electron bunches are created through a double laser pulse that impinges on a photo-cathode. Initially, these two bunches are delayed by a few picoseconds, however, two magnetic chicanes compress the peak current of the electron bunches from 20 A to 4 kA such that after the acceleration in the linac a time delay on the ten-femtosecond timescale is achieved. Also after the acceleration stage, the

electron bunch also have a difference in kinetic energy, i.e., Lorentz factor, γ . When the electron bunches then travel through the undulator section, both pulses saturate in their lasing process at different colors. For 8.3 keV photons, both pulses combined can reach pulse energies of 1.2 mJ, the color separation is 100 eV, and the time separation ranges from $\Delta t_{\min} = 0$ fs to $\Delta t_{\max} = 100$ fs. For hard X-rays, this method requires the pump-pulse to have a higher photon energy than the probe-pulse, although their respective intensities may vary. For soft X-rays, the slotted spoiler foil can be used. This enables further control over the electron bunches and allows crossing time zero with both pulses.

2.2. Rare-gas clusters

Clusters have a long history as samples to study the light-matter interaction for a few reasons. In general, their characteristics are well known, they can form interesting states, and they often have practical purposes [56]. Generally speaking, clusters are an aggregation of atoms or molecules and vary in size. Their size ranges from a few atoms to mesoscopic sizes such that one can classify a cluster as a bulk material. Rare-gas clusters are a subclass of clusters and they are bound by van der Waals forces, thus are normally neutral-charged. Single van der Waals clusters typically form in an icosahedral⁷ shape when they are sufficiently small (up to nanometer sized) [57] and have mostly a fcc-crystal⁸ structure but exhibit also hcp-crystal⁹ structures [58, 59]. In the present work, superfluid helium clusters (or droplets), solid xenon clusters and a mixture of both have been used as a sample as they form a finite system that can be produced and tuned in size easily, they have no energy dissipation and can exist in the gas phase. The creation of homogenous and heterogeneous rare-gas clusters is discussed in the next sub-sections.

2.2.1. Generation of homogenous clusters

Rare-gas clusters, for example xenon clusters, can be generated in a variety of ways. Often, as in the described experiment, rare-gas clusters are created via supersonic expansion by releasing gas from a reservoir through a nozzle into a vacuum. The gas in the reservoir is at a certain stagnation pressure, p_0 , and temperature, T_0 . Typical values for p_0 are 10 bar, where the mean free path of the atoms is much smaller than the nozzle diameter¹⁰. This is why many collisions occur in the nozzle during the gas expansion

⁷An icosahedron is a polyhedron with 20 faces, i.e., a dice with 20 faces.

⁸fcc is an acronym for face-centered cubic. A very common crystal structure.

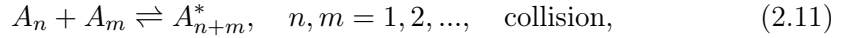
⁹hcp stands for hexagonal close-packed and is also a crystal structure.

¹⁰A schematic drawing of the nozzle used in this work can be found in Figure 3.7. See also Equation (2.20) for non-pinhole nozzle openings.

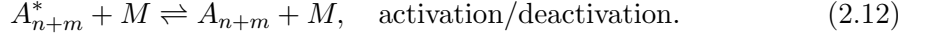
2. Fundamental Concepts

but collisions do not occur in the free supersonic expansion. The collisions in the nozzle intuitively explain the cluster formation [60], which we will discuss first. We follow the phenomenological discussion with a more detailed description of the supersonic gas expansion and end the section with the empirically derived scaling laws that describe average sizes for rare-gas clusters.

In the nozzle, clusters grow through collisions. The initial stages of the cluster growth are driven by monomer addition but as more and more clusters are available, cluster-cluster coagulation starts to dominate the later growth process. The monomer addition can be expressed mathematically through the following reaction formula



with n, m denoting the number of monomer assembling body $A_{n,m}$. A body A_n collides with another body A_m and forms a metastable state A_{n+m}^* that will dissociate if no subsequent collision deactivates it



M is a chaperone that can be any kind of third body that adds or removes energy from the system. M can therefore activate or deactivate the system. The cluster-cluster coagulation in later stages is due to the quantitative increase in small clusters in the generation process that then start to collide, similar to the above reaction formulas. From empirical evidence [61, 62], we know that clusters solely generated through monomer addition follow a size distribution of an exponential decay with a rather large decay constant, whereas larger clusters that grew through coagulation follow a log-normal distribution. Here, the density of smaller clusters including monomers and dimers decreases as larger clusters are formed of these particles through coagulation. During the entire formation process, binding energy is set free that heats the cluster efficiently. In order to lose energy, the cluster typically evaporates monomers. The evaporation process makes the ultimate temperature of the cluster size-independent, after the clusters have reached a certain minimum size [63]. The cluster temperature is heavily dependent on their material, particularly the binding energy. Relevant for this study are the temperature of Xenon cluster, which is $\sim 75\text{ K}$ ¹¹, and the fact that xenon clusters are solid as their

¹¹To put this temperature in perspective, krypton clusters have a temperature of $\sim 50\text{ K}$ and argon clusters $\sim 40\text{ K}$, when they are created through a supersonic jet expansion, with a certain flight distance, and have a minimum size of 800 atoms [63, 64].

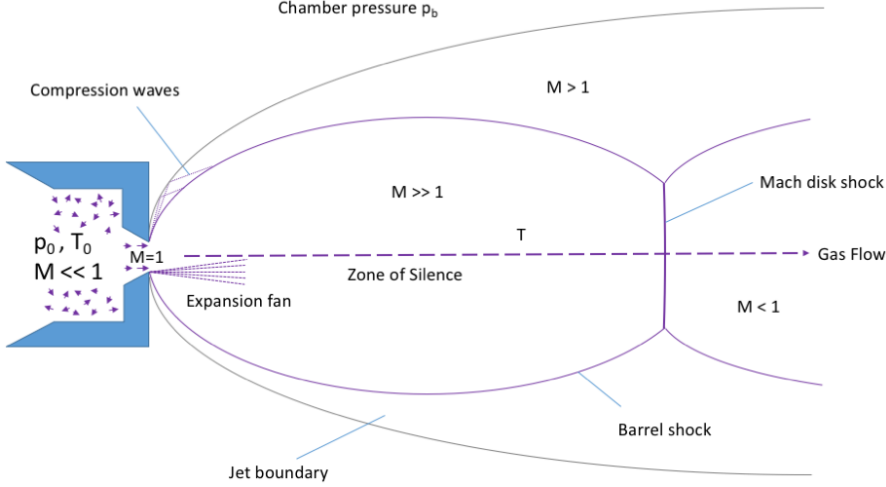


Figure 2.9.: Schematic of a supersonic gas expansion into the vacuum. Gas is stored in a reservoir at pressure p_0 , temperature t_0 and speed of the gas is thermally distributed ($M \ll 1$). As the gas enters the nozzle area, it is accelerated to the speed of sound ($M = 1$) and as the gas expands, the temperature T drops altering the speed of sound such that the gas now travels supersonically ($M \gg 1$). In this expansion, clusters are generated in the nozzle region, where $M = 1$ (see text for details). After [66].

melting temperature is higher [64]. For similar reasons, helium-clusters are liquid, which is why they are often called helium-droplets. If helium-droplets are produced using a cryogenic jet also superfluid helium-droplets can be observed [65].

To discuss the supersonic expansion in detail, we assume an ideal gas and assume that turbulence and the effects of heat conduction are unimportant [56, 67]. Figure 2.9 shows a schematic drawing of this process. In the reservoir, the velocity distribution of the gas is thermally distributed at a set temperature T_0 . The movement direction of each atom is randomly orientated. For an ideal gas, we can define the enthalpy, H_0 , in the stagnation chamber by

$$H_0 = C_P T_0. \quad (2.13)$$

The expansion of the gas through the nozzle is driven by the pressure ratio p_b/p_0 . Only when the ratio exceeds a critical value, G , the expansion will be supersonic. We note, $G \equiv ((\gamma + 1)/2)^{\gamma/(\gamma-1)}$, where γ is the ratio of specific heats, $\gamma = \frac{C_P}{C_V}$, at constant pressure, C_P , and volume C_V . γ can be regarded as independent of temperature for

2. Fundamental Concepts

atomic gases. In the nozzle, the steady gas flow becomes directed and the enthalpy, H_0 , is converted into kinetic energy, $\frac{1}{2}mv^2$, and a remaining enthalpy, H . We can use the conservation of energy and Equation (2.13) to write down

$$H_0 = H + \frac{1}{2}m_{gas}v^2 = C_P T + \frac{1}{2}m_{gas}v^2, \quad (2.14)$$

with T being the local temperature along the gas flow and m_{gas} the atomic mass of the gas. To simplify, let us define the Mach number, $M \equiv v/c_s$, as the ratio of the stream velocity, v , and the local speed of sound, c_s . We can express the local speed of sound as

$$c_s = \sqrt{\frac{\gamma k_B T}{m_{gas}}}, \quad (2.15)$$

where k_B is the Boltzmann constant and we can rearrange Equation (2.14) to

$$T = T_0 \left(1 + \frac{1}{2} (\gamma - 1) M^2 \right)^{-1}. \quad (2.16)$$

Here, the interplay between the Mach number and the local temperature give insight into the directed mass flow versus the remaining thermal energy in the system. As indicated in the Figure 2.9, M increases dramatically along the indicated gas flow direction and that is due to a decrease in c_s , which is proportional to \sqrt{T} as indicated in Equation (2.15). The gas quickly reaches the terminal velocity while the speed of sound is decreasing. We may write the terminal velocity as

$$v_\infty = \sqrt{\frac{2R}{m_{gas}} \left(\frac{\gamma}{\gamma - 1} \right) T_0}, \quad (2.17)$$

with R being the universal gas constant. The expansion speed of the gas gives the name to such types of gas sources, namely supersonic jets. This equation is also useful to calculate gas or cluster flight times – $t_{\text{flight}} = \frac{D}{v_\infty}$ – if the distance D from nozzle to interaction point is known (see Section 3.4.1).

The appearance of the supersonic jet stream (see Figure 2.9) is particularly important for the experimental aspect of delivering the sample to the interaction region. Upon exiting the nozzle, the Mach number increases by a wide margin ($M \gg 1$). This means that the gas travels faster than information in this medium, i.e., the local speed of sound. Here, a *zone of silence* is formed, where the gas flow is not influenced by other particles or boundary conditions. At the borders of the zone of silence, M decreases drastically,

Helium	Neon	Argon	Krypton	Xenon
3.85	185	1646	2980	5554

Table 2.1.: Parameter K_{gas} values for rare-gases [68].

resulting in dense regions that are called *barrel shock* to the sides and *Mach disk shock* downstream the gas flow [66]. For an unhindered transport of the gas and clusters to the interaction region, the interaction region needs to be within the zone of silence. We can express the distance from the nozzle to the Mach disk x_{MD} through

$$\frac{x_{MD}}{d} = 0.67 \sqrt{\frac{p_0}{p_b}}, \quad (2.18)$$

with the nozzle diameter d . So the competing stagnation pressure, p_0 , and the vacuum chamber pressure, p_b , define the distance of the otherwise static parameters. p_b needs to be low enough to drive the Mach disk downstream of the interaction region. By using skimmers and thereby physically separating the jet expansion into separately pumped compartments, the pressure p_b can be reduced, hence x_{MD} increased.

The average cluster size is very much dependent on the gas type, stagnation temperature T_0 , stagnation pressure p_0 , and the nozzle diameter. An empirically found scaling law, named after Hagena [69–71], can be summarized as follows. The Hagena scaling parameter, Γ^* , reads

$$\Gamma^* = K_{\text{gas}} \cdot T_0^{0.25x-1.5} \cdot p_0 \cdot d_{eq}^x \quad [\mu\text{m mbar K}^{-1}], \quad (2.19)$$

with the gas-specific parameter K_{gas} that can be found in Table 2.1 for some rare-gases, the gas specific parameter x that varies between 0.5 and 1 and is 0.85 for all rare-gases, and the equivalent nozzle opening, d_{eq} , that is $d_{eq} = d$ for pinhole sources. For conical nozzles, d_{eq} becomes [68]

$$d_{eq} = d \frac{\tan(\Phi_0)}{\tan(\Phi)} = 0.719 \frac{d}{\tan(\Phi)}, \quad (2.20)$$

where Φ is the half-opening angle of the nozzle and Φ_0 is the half-opening of the free gas expansion. Γ^* allows us to estimate the mean cluster size, i.e., the mean amount of accumulated particles per cluster $\langle N \rangle$, via the following cases

- $\Gamma^* < 350$, no cluster formation is observed;

2. Fundamental Concepts

- $350 < \Gamma^* < 1800$, in this region $\langle N \rangle$ reads [72]

$$\langle N \rangle = 38.4 \left(\frac{\Gamma^*}{1000} \right)^{1.64}; \quad (2.21)$$

- after $1800 < \Gamma^*$, $\langle N \rangle$ is

$$\langle N \rangle = 33.0 \left(\frac{\Gamma^*}{1000} \right)^{2.35}. \quad (2.22)$$

There is a range, where the mean cluster size appears to deviate from Hagena's law [73], and it is

- In the range $10^4 < \Gamma^* < 10^6$, Γ^* becomes

$$\langle N \rangle = 100 \left(\frac{\Gamma^*}{1000} \right)^{1.8}. \quad (2.23)$$

Note, however, that for larger cluster sizes, the Equation (2.22) becomes true again [74, 75].

Experiments using supersonic jets for cluster generation are sometimes performed with pulsed valves to decrease cost and gas load in the overall system. Upon opening and closing of the valve, the gas density can vary. This affects the cluster size and one would expect to see smaller clusters. It has been observed that one finds smaller clusters in the beginning of the pulse, but in the *afterpulse* one finds giant clusters that exceed the above-described scaling laws due to the effects when closing the valve [76].

Supersonic jets generally create clusters of different sizes. This size distribution is centered around $\langle N \rangle$ and for solid rare-gas clusters this distribution is a log-normal distribution. The size distribution can be an experimental challenge, especially when size dependent effects are investigated. Historically, electron diffraction [63, 77] has been used to determine the mean cluster size, mean temperature and mean geometry. Today, free electron lasers allow the determination of the size of a single cluster through a diffraction image [78], and by measuring enough single clusters, one can reproduce size distributions of a supersonic jet as shown in Figure 5.1.

2.2.2. Creation of heterogeneous clusters: The pickup principle

A possibility to create heterogeneous clusters is through the principle of picking-up atoms or molecules [56]. Figure 2.10 illustrates pickup regions that are typically used in an

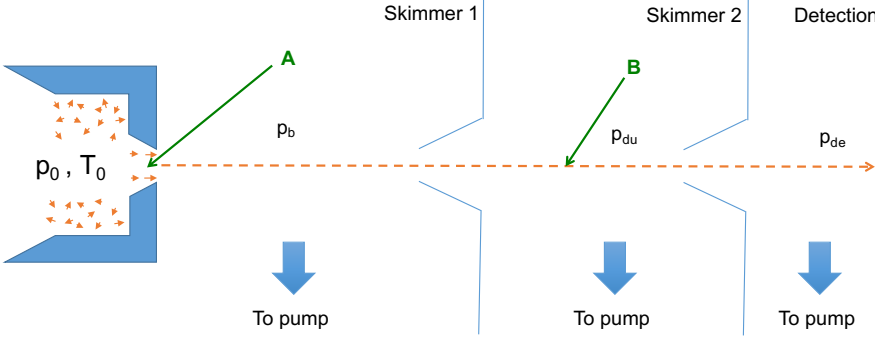


Figure 2.10.: Schematic setup to generate heterogeneous clusters through pickup. Thereby is a cluster generated via supersonic gas expansion, which is doped at regions marked A or B. In region A, the dopant gas is mixed in the nozzle such that it becomes part of the nucleus. In region B, the cluster condenses atoms on its surface from the background gas of the chamber with pressure p_{du} . The cluster can be detected upon evaporation, e.g., due to contact with the chamber, through the pressure p_{de} . After [56, 79].

experiment. Mainly, there are two different places where the cluster encounters a dopant material, one, monomers are added to the cluster in region A of Figure 2.10, which represents the nozzle of a supersonic source and can be achieved by, e.g., co-expanding a gas-mixture; two, they can be picked up by a cluster in region B, for example, through an increased chamber pressure p_{du} with the dopant material. If clusters encounter atoms or molecules in the nozzle region A, they can become part of the cluster formation and can be found inside of solid clusters. If atoms or molecules are picked up in region B, they typically stick to the surface of solid clusters. If a liquid or superfluid cluster picks up a dopant, it may move within the droplet. Since the traversing cluster is much larger and heavier than a colliding monomer, the trajectory is not affected significantly. Ar-cluster with $\langle N \rangle = 5.9 \cdot 10^9$ particles can pick-up 0.05 % as many SF₆ molecules with chamber pressures of $p_{du} = 2 \cdot 10^{-5}$ mbar over a pickup length of a few centimeters [79]. At these low pressures, picking up atoms or molecules in region B requires less gas load on the system but is also less efficient than picking up in region B. To increase the pickup levels in region B, a gas cell can be used as much higher pressures can be achieved within the gas cell without putting too much gas-load on the overall system. In this work, gaseous xenon was picked up by superfluid helium droplets in region B.

To understand the doping process further, the following considerations are useful. When a cluster and a dopant bond, the binding energy that is specific to the materials is added

2. Fundamental Concepts

system. This is similar to the cluster growth process itself. The cluster will lose this energy through evaporation of monomers [65]. The loss of particles through evaporative cooling is dependent on the ratio of binding energies of the two materials and can be expressed as

$$N_{\text{Evaporated from cluster}} \approx \frac{\epsilon_{\text{cluster}}}{\epsilon_{\text{dopant}}}, \quad (2.24)$$

with the binding energy of the cluster $\epsilon_{\text{cluster}}$ and of the dopant ϵ_{dopant} . In the case of this thesis, where a helium droplet is doped with xenon atoms, we may use the binding energies of helium, $\epsilon_{He} \approx 0.6 \cdot 10^{-3}$ eV, and of xenon, $\epsilon_{Xe} \approx 0.15$ eV [11, 65], to estimate that approximately 250 helium atoms evaporate by picking up 1 xenon atom.

Now we can extend this idea to estimate the number of picked-up atoms, if we were to know the number of atoms in the cluster before and after the pickup area. An estimate of the initial mean cluster-size, i.e., $\langle N_{\text{cluster}} \rangle$, can be reached through the scaling laws¹² as discussed in Section 2.2.1. An estimate of the cluster size after the pickup can be established through measuring the partial pressure of the cluster material without the pickup, p_{de} , for example, in the detection chamber when the particle jet hits a wall and evaporates¹³ (see Figure 2.10), and the partial pressure with pickup, Δp_{de} . The relative difference $\frac{\Delta p_{\text{de}}}{p_{\text{de}}}$ then scales with

$$\langle N_{\text{dopant}} \rangle \approx \frac{\epsilon_{\text{cluster}}}{\epsilon_{\text{dopant}}} \cdot \frac{\Delta p_{\text{de}} \langle N_{\text{cluster}} \rangle}{p_{\text{de}}}, \quad (2.25)$$

such that the mean amount of picked up atoms, $\langle N_{\text{dopant}} \rangle$, can be estimated.

2.3. Fundamental processes of soft X-rays and nanoparticles

Nanoparticle respond to intense X-ray radiation by scattering or absorbing the rays. Figure 2.11 shows the most probable processes in the X-ray wavelength range. For soft X-rays, the processes can be reduced to the photoionization process and the coherent and elastic scattering. The Section 2.3.1 discusses photoionization and the resulting core-hole decay processes; section 2.3.2 discusses the coherent and elastic scattering of an electron and extends this concept to the scattering and imaging of a nanoparticle; the section 2.3.3 generalizes the refractive index. The chapter follows the discussion in [22] and avoid effects that have negligible cross-sections such as the Compton effect, the

¹²As already established the actual cluster size produced with a supersonic jet will vary, hence the average cluster size $\langle N_{\text{cluster}} \rangle$.

¹³For example with a residual gas analyzer.

2.3. Fundamental processes of soft X-rays and nanoparticles

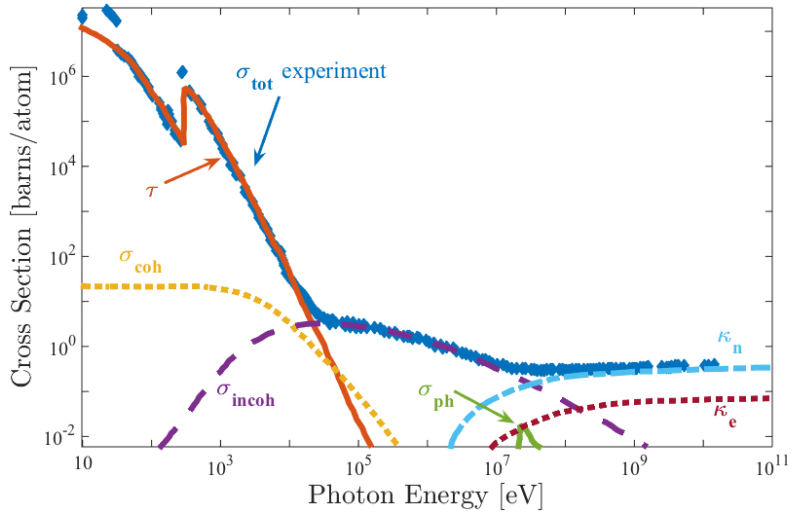


Figure 2.11.: The total cross-section of atomic carbon, σ_{tot} , as a function of energy. Several processes add to, σ_{tot} : τ , is the photoionization; σ_{coh} , is coherent scattering; σ_{incoh} , is the incoherent scattering; σ_{ph} , is photonuclear absorption; κ_n , and κ_e , are pair-production events. At the experimental photon energy of 837 eV, the dominant effects are photoionization and coherent scattering. From [36, 80].

2. Fundamental Concepts

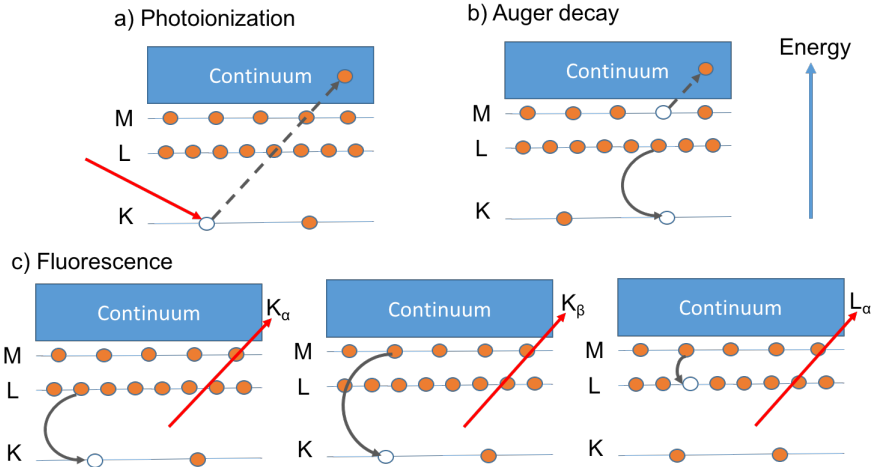


Figure 2.12.: Schematic illustration of common charge transfer processes. a) Photoionization: Describes a direct emission of a K-shell electron after absorbing an X-ray photon. b) Auger decay: A relaxation process, where a K-shell hole is filled with an electron from the L-shell and the remaining energy is released through emission of an electron in an outer shell. c) Fluorescence: An electron hole is filled with an electron from an outer shell and the remaining energy is released through photons. After [22].

pair-production, and the scattering from the nucleus.

2.3.1. Photoionization and core-hole decay

Given the photon energies of soft X-rays, atoms are typically core-ionized when absorbing a soft X-ray photon, which is depicted in Figure 2.12 a) Photoionization. This typically leaves the atom in an excited state. In order to emit energy, the core-hole usually decays according to the schematics in Figure 2.12 b) Auger decay and c) Fluorescence, whereby the Auger decay is the dominant process.

Photoionization is the process, where an atom or molecule is transformed into an ion through absorption of a photon and emission of an electron (see Figure 2.12 a)). Hereby, the photon energy must be higher than the ionization threshold. Figure 2.13 shows the total absorption cross-sections, σ_a , for xenon and helium for various photon energies. σ_a is strongly dependent on the photon energies as resonant behavior occurs near absorption edges. The experimental photon energy of 837 eV has been chosen such that xenon absorbs photons dominantly over helium but is off-resonance. The total absorption cross-section is consisting of the differential absorption cross-sections that are specific for the

2.3. Fundamental processes of soft X-rays and nanoparticles

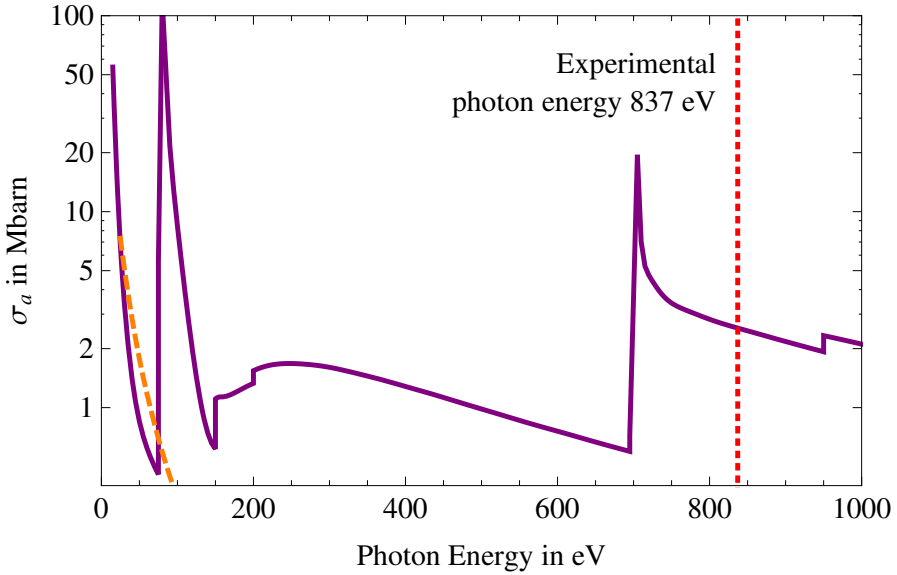


Figure 2.13.: Total absorption cross-sections σ_a in megabarn for xenon (purple line) and helium (orange dashed). The photon energy of the described experiment is ~ 837 eV (red dashed). Data points from [81–83].

Shell	Subshell	Cross-section in Mb	subshell ionization potential in eV
K	1s	-	34630.0
L	2s	-	5466.4
	2p	-	4899.1
M	3s	-	1153.3
	3p	-	965.4
	3d	2.2505	682.7
N	4s	0.0305	223.7
	4p	0.1247	161.8
	4d	0.2587	68.2
O	5s	0.0040	27.3
	5p	0.0120	12.5

Table 2.2.: Differential absorption cross-sections and ionization potentials for certain electronic configurations of xenon at 837eV. Calculations based on [84].

2. Fundamental Concepts

El. Configuration, and ionized subshell	Ionization of subshell	Cross-section σ_a in Mbarn	subshell ionization potential in eV
$\text{He}^{+0}, 1s2$	1s2	0.0007	24.4
$\text{He}^{+1}, 1s1$	1s1	0.0005	54.4
$\text{Xe}^{+0}, 5p6$	3d10	2.2505	682.7
$\text{Xe}^{+1}, 3d9$	3d9	2.1487	733.6
$\text{Xe}^{+1}, 5p5$	3d10	2.2443	693.7
$\text{Xe}^{+2}, 5p4$	3d10	2.2390	705.9

Table 2.3.: Absorption cross-sections σ_a and ionization potentials for certain electronic configurations, including certain ionization profiles. Calculations based on [84].

subshells¹⁴ in an atom. Table 2.2 shows the differential absorption cross-sections and ionization potentials for xenon. If the photon energy is below the ionization threshold of a subshell, the differential cross-section becomes near zero. At the photon energy of 837 eV, xenon mainly absorbs photons in the 3d-subshell. After ionization, the electronic structure of an atom changes, which alters particular ionization energies and absorption cross-sections. Table 2.3 shows total absorption cross-sections for helium and xenon in various electronic configurations. The number of ionization configurations is numerous and the table shall give the reader merely an impression of the change in some for the experiment likely configurations.

The Auger decay is a two-step process (see Figure 2.12 b); one, an outer shell electron is emitted into the continuum, the so-called *Auger-electron*¹⁵; two, another electron in the atom simultaneously fills the electron-hole [89]. An *Auger decay* typically occurs on the few femtoseconds timescale after core-ionization [90]. Emitted Auger-electrons have discrete energies depending on the combination of electrons involved in the process. One can use this attribute to, for example, identify elements or calibrate energies. The right panel of Figure 2.14 shows a partial K-LL¹⁶ Auger spectrum from neon illuminated by 1050 eV photons from the LCLS and measured with a hemispherical analyzer as described in [40]. In this example, neon is ionized in the K-shell and an electron-hole in the 1s shell is created. An electron from the L-shell fills the 1s hole and another electron from the L-shell, the Auger electron, is emitted into the continuum. As there is a variety of electronic configurations that can be involved in this process multiple peaks appear

¹⁴Disregarding the hyperfine structure, which is a shift in atomic energy levels due to interaction of electrons with the nucleus [85].

¹⁵Named after the French physicist Pierre Auger.

¹⁶This nomenclature means a single core-hole in the K-shell decays into two holes in the L-shell.

2.3. Fundamental processes of soft X-rays and nanoparticles

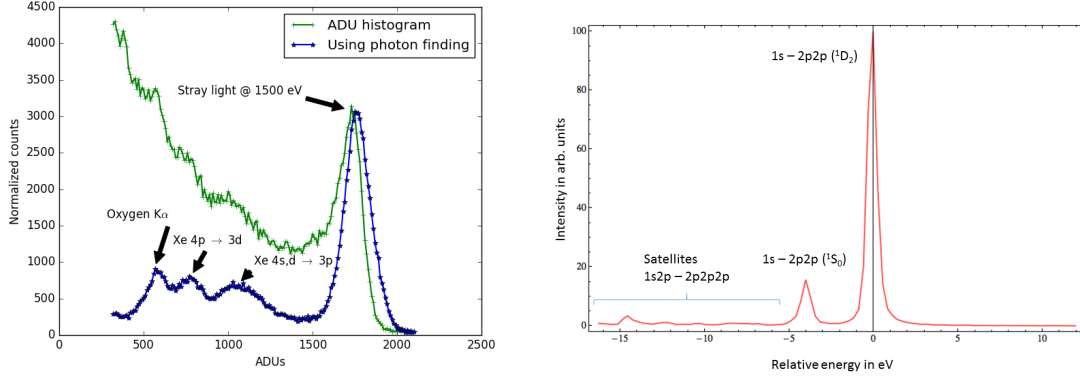


Figure 2.14.: Left spectra shows fluorescence peaks from xenon and oxygen illuminated with 1.5 keV photons from the LCLS; detected with pnCCD detectors [86, 87]. The green curve is an ADU histogram of the pnCCD detector and the blue curve uses a coalescent photon finder. Right, partial K-LL Auger spectrum with rel. energy 0 corresponding to 804.5 eV. Spectrum is measured with a photoelectron spectrometer [40], peaks identified as in [88].

for similar occupation configurations, e.g., 1s - 2p2p. More complex structures, called satellites, appear when the atom is already ionized, for example, when an atom has a hole in the L-shell and then photoionization creates another hole in the K-shell will lead to KL-LLL satellites [89]. Double K-ionized atoms will produce so-called hypersatellites [91], which occurs in the intense soft X-ray pulses of LCLS [32]. The transition can also be of the same shell and is then called a Coster-Kronig transition, for example, the N-NN Coster-Kronig transitions in xenon [92].

Fluorescence is the emission of light by a material that has been photoexcited (see Figure 2.12 c). Is the material illuminated with soft X-rays, the fluorescence leads to the emission of X-rays that have usually very specific energies, e.g., K α^- , K β^- , and L α -lines. These can be used for, e.g., element identification, or chemical analysis. Fluorescence often occurs on the nanosecond timescale [93] and typically for soft X-rays is that the Auger decay-rates beat the Fluorescence decay-rates. The left panel of Figure 2.14 shows fluorescence peaks that contribute to the background signal when diffraction images are taken with the pnCCD detectors (see Section 3.3).

2. Fundamental Concepts

2.3.2. From Thomson scattering to diffractive imaging

When light interacts with a nanoparticle, it dominantly scatterers of electrons. Let us first consider the elastic scattering of a free electron, or *Thomson scattering*, as a result of being accelerated in an electro-magnetic field. Then, we proceed to the scattering of an atom followed by the scattering of an extended object with a continuous electron density. We end the section with some considerations that are relevant for this work.

Let us introduce the electric field of an incident wave $E_{in} = E_0 e^{-i\omega t}$ that irradiates an electron. The electron is accelerated in this electric field and emits radiation similarly to a small dipole antenna. We can write this radiated electric field as [22]

$$E_{rad}(R, t) = - \underbrace{\left(\frac{e^2}{4\pi\epsilon_0 mc^2} \right)}_{r_0} E_{in} \frac{e^{ikR}}{R} \cos(\psi), \quad (2.26)$$

with k being the usual wave-number, R being the distance from the source of radiation, ψ being the observation angle, and r_0 being the *Thomson scattering length*, or the *classical electron radius*. r_0 can be written in practical units as

$$r_0 = \frac{e^2}{4\pi\epsilon_0 mc^2} = 2.82 \cdot 10^{-5} \text{ Å}, \quad (2.27)$$

where $-e$ is the charge of the radiating electron, m is the mass of the electron, c is the speed of light, and ϵ_0 is the permittivity of free space.

Now we would like to understand the cross-section of this scattering process better. We can establish a *differential cross-section*, $(d\sigma/d\Omega)$, which follows the same concept of the already discussed example in Equation (2.2). The only difference is that we now consider a scattered intensity, I_{sc} , of an incident flux, (I_0/A_0) , into a solid angle, $\Delta\Omega$. We may express this as

$$\left(\frac{d\sigma}{d\Omega} \right) = \frac{I_{sc}}{(I_0/A_0) \Delta\Omega} = \frac{|E_{rad}|^2 R^2}{|E_{in}|^2} = r_0^2 \cos^2(\psi), \quad (2.28)$$

which is also called the differential cross-section for *Thomson scattering*. By integrating over the full angular space, the total cross-section for Thomson scattering, σ_T , results in

$$\sigma_T = \left(\frac{8\pi}{3} \right) r_0^2 = 0.665 \text{ b} \quad (2.29)$$

2.3. Fundamental processes of soft X-rays and nanoparticles

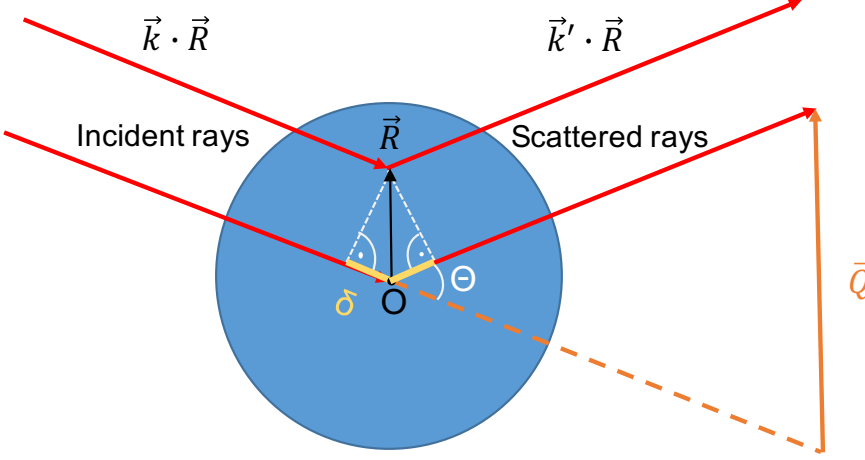


Figure 2.15.: Principle of scattering rays of an atom. After [22, 94].

We can now move on and use this knowledge for atoms, where we have Z electrons. To describe electrons in an atom, let us introduce an electron density $\rho_e(\vec{r})$ that describes the probability density of electrons in an atom. Figure 2.15 illustrates the scattering process by one atom. An incident beam, with wave-vector \vec{k} , is elastically scattered at the origin, O , into a wave with \vec{k}' such that $|\vec{k}| = |\vec{k}'|$. It is useful to define the *wave-vector transfer*, $\vec{Q} = \vec{k} - \vec{k}'$, which we can write in terms of the *scattering angle*, Θ , as

$$|\vec{Q}| = 2|\vec{k}| \sin\left(\frac{\Theta}{2}\right) = \frac{4\pi}{\lambda} \sin\left(\frac{\Theta}{2}\right), \quad (2.30)$$

where λ is the wavelength of the light.

A volume element $d\vec{R}$ of the atom at \vec{R} will now scatter waves proportional to its electron density, which we can express by $-r_0 \rho(\vec{R}) d\vec{R}$. At scattering angle $\Theta = \vec{Q} = 0$, the *atomic scattering factor*, f^0 , can be shown to be

$$f^0(\vec{Q} \rightarrow 0) = Z, \quad (2.31)$$

because all scatterers are in phase. As we increase the scattering angle Θ , a wave that is scattered at the origin, O , and one at \vec{R} have an optical path difference of 2δ . This difference in path length results in a phase difference, $\Delta\Phi$, in the wavefront. $\Delta\Phi$ can be expressed as

$$\Delta\Phi = (\vec{k} - \vec{k}') \cdot \vec{R} = \vec{Q} \cdot \vec{R}. \quad (2.32)$$

2. Fundamental Concepts

We may multiply a *phase factor*, $e^{i\vec{Q}\cdot\vec{R}}$, to the contribution of the scattered field, $-r_0 \rho(\vec{R}) d\vec{R}$, to argue that the volume elements start to scatter out of phase. As a consequence and in the limit of $\vec{Q} \rightarrow \infty$, the atomic form factor is $f^0(\vec{Q} \rightarrow \infty) = 0$. Let us gather these phenomenological arguments, integrate over them to obtain the total scattering volume, and note

$$-r_0 f^0(\vec{Q}) = -r_0 \int \rho_e(\vec{R}) e^{i\vec{Q}\cdot\vec{R}} d\vec{R}. \quad (2.33)$$

This important result is called the atomic form factor in units of $-r_0$. It can be understood as a Fourier transformation of the electron density of an atom.

Let us continue with the scattering of a molecule or cluster that consist of multiple atoms. We can label the atoms in such an object by

$$F^0(\vec{Q}) = \sum_{\vec{R}_j} f_j^0(\vec{Q}) e^{i\vec{Q}\cdot\vec{R}_j}, \quad (2.34)$$

with the atomic form factors $f_j^0(\vec{Q})$ for the j 'th atom and call F^0 the single particle *structure factor*. For coherent and monochromatic radiation the scattered amplitude, $A(\vec{Q})$, of a nanoparticle can be written in the kinematical approximation¹⁷ as [95]

$$A(\vec{Q}) = \int \rho(\vec{R}) e^{i\vec{Q}\cdot\vec{R}} d\vec{R}, \quad (2.35)$$

where $\rho(\vec{R})$ is the electron density of the scattering nanoparticle. This operation can again be interpreted as a Fourier transformation of the single particle's electron density. But only scattered intensities can be measured with, e.g., a CCD detector. So, the scattered intensity in a diffraction pattern can be expressed by

$$I_{sc}(\vec{Q}) = I_0 |A(\vec{Q})|^2, \quad (2.36)$$

where I_0 is the intensity of an incident beam¹⁸. Unfortunately, the operations on the amplitude, $|A(\vec{Q})|^2$, eliminate the phase factor, such that merely an inverse Fourier transformation cannot be used to reconstruct the real-space electron density from measured intensities. This is known as *inverse problem* and can be solved via iterative phase-retrieval algorithms that we will discuss in Section 4.3.

¹⁷Sometimes called the weak-scattering limit, where multiple scattering effects are neglected.

¹⁸Here, we make use of the Born approximation and the intensity of the incident beam becomes constant, which holds true in the kinematical approximation

2.3. Fundamental processes of soft X-rays and nanoparticles

El. Configuration, and ionized subshell	Scattering factor f^0 in barn
He^{+0} , 1s2	2.55
He^{+1} , 1s1	0.65
Xe^{+0} , 5p6	1874.36
Xe^{+1} , 3d9	1813.56
Xe^{+1} , 5p5	1814.68
Xe^{+2} , 5p4	1754.08

Table 2.4.: Atomic scattering factor f^0 for certain electron configurations. From [96].

Let us now make use of above's theory and address the scattering of a rare-gas cluster, as they will reoccur throughout this thesis. We may thus express an electron density of the desired object and Fourier transform it into reciprocal space to understand diffraction patterns better. Due to current resolution limitations¹⁹, we may approximate the shape of a few nanometer-sized cluster with a sphere. The density, ρ , of a hard sphere with radius, r , can be expressed by

$$\rho(\vec{R}) = \begin{cases} \rho & \text{for } r \geq |\vec{R}| \geq 0, \\ 0 & \text{for } r > |\vec{R}|. \end{cases} \quad (2.37)$$

Using this equation, we can solve the integral in Equation (2.35) by making use of spherical coordinates,

$$A_{\text{Sphere}}(\vec{Q}) = \int_0^\pi \int_0^{2\pi} \int_0^r R^2 \sin(\Theta) e^{i\vec{Q} \cdot \vec{R} \cos(\Theta)} dR d\Theta d\Phi, \quad (2.38)$$

$$= \rho \left(\frac{4}{3\pi} r^3 \right) \frac{\sin(\vec{Q} \cdot \vec{r}) - \vec{Q} \cdot \vec{r} \cos(\vec{Q} \cdot \vec{r})}{\vec{Q}^3 r^3}. \quad (2.39)$$

This result can be exploited to determine the size of a spherical particle, i.e., a cluster, using local minima in the diffraction pattern²⁰ or through a numerical fit of the resulting curve.

The total atomic scattering factors, f^0 , for helium and xenon in some electron configurations can be found in Table 2.4. The f^0 calculations are based on Equation (2.33) [96]. Xenon atoms scatter dominantly over helium atoms as xenon's f^0 is over 700 times larger

¹⁹Considering experimental details from Chapter 3

²⁰Equation (2.39) can be solved numerically for the distance between the first two minima, $\vec{Q}_{\min n}$ and $\vec{Q}_{\min n+1}$, such that $r = \frac{3.24}{\vec{Q}_{\min n+1} - \vec{Q}_{\min n}}$.

2. Fundamental Concepts

than helium's. This means for the diffraction images of mixed HeXe-clusters that xenon atoms contribute as much as helium atoms when the doping level is $\sim 0.14\%$. Also upon ionization, xenon atoms scatter dominantly; singly ionized xenon atoms have f^0 reduced by only $\sim 3\%$ and singly ionized helium atoms have f^0 reduced by $\sim 75\%$ compared to their neutral electron configurations. For the same ionization level in xenon, e.g., Xe^{+1} , but different electron configurations, f^0 varies only on the order of $\sim 0.05\%$, which is a small effect compared to the change in f^0 when xenon becomes increasingly ionized.

2.3.3. Generalized index of refraction

Last section established that an electron was accelerated by a light field and radiated as a result. But it is not only the light field that drives the electron, also the electron has an effect on the light field. Ultimately, this effect changes how rays scatter of extended objects and therefore our interpretation of recovered real-space electron densities. The atomic form factor can be corrected for these effects with the so-called *dispersion corrections*. We shall not derive this topic to its full extent as it can be found in [97, p. 55 ff], but we shall qualitatively compare the equation for the complex refractive index, $n(\omega)$, to the resonant description of the atomic form factor, $f(\vec{Q}, \omega)$. For simplicity, we reduce the following considerations to the case of forward scattering, where $\vec{Q} = \Theta = 0$.

As a wave propagates through a medium, for example, from air through water, it changes direction according to *Snell's law* [22]. Here, a medium is attributed a refractive index,

$$n = \frac{c}{v_{\text{phase}}}, \quad (2.40)$$

where v_{phase} is the phase velocity that changes inside the material. n is wavelength dependent and for visible wavelengths, it ranges between 1.2 and 2, which indicates $v_{\text{phase}} < c$. X-rays usually have a refractive index of $n < 1$. As a result, one usually speaks of a *phase advance* when an X-ray field traverses an object. Another aspect, when a light wave is traveling through, e.g, from air through water, is the attenuation of the amplitude. When a light wave travels through a medium along the Z -axis, its amplitude is reduced by $e^{\mu Z/2}$, with μ being the *absorption coefficient*. The amplitude of an electro-magnetic wave that propagates through a medium along the Z -axis with wave number k and the above considerations can be expressed as [97]

$$e^{inkZ} = \underbrace{e^{ikZ}}_{\text{vacuum propagation}} \underbrace{e^{i(\delta)kZ}}_{\text{phase shift}} \underbrace{e^{-\beta kZ}}_{\text{decay}}, \quad (2.41)$$

2.3. Fundamental processes of soft X-rays and nanoparticles

where n is the complex refractive index, δ is its real part resulting in a phase shift of the wave, and $i\beta = i\mu/(2k)$ is the imaginary part resulting in a decline of the amplitude of the wave. The complex refractive index, n , is thus usually written as

$$n = 1 - \delta + i\beta. \quad (2.42)$$

But the refractive index can also be written in terms of the atomic form factor. For this, let us imagine electrons in an atom. The electrons response to being driven by a light field is reduced depending on their binding energies. This can be denoted as f' . The bound electrons can also be photoionized, which can be accounted for by an imaginary factor, if'' , similar to above. These two resonant effects are called dispersion corrections to the non-resonant atomic scattering factor, f^0 . Let us include these corrections to the atomic scattering factor and note

$$f(\vec{Q}, \omega) = f^0(\vec{Q}) + f'(\omega) + if''(\omega). \quad (2.43)$$

Above resonance ω , bound electrons can be largely seen as free electrons such that $f'(\omega) \rightarrow 0$ and $f''(\omega) \rightarrow 0$. Close to resonance, $f'(\omega)$ and $f''(\omega)$ can become large factors.

We can compare Equation (2.42) to Equation (2.43) and note the complex refractive index through the atomic form factor as [22]

$$n = 1 - \frac{2\pi\rho_{atom}r_0}{k^2} \left(f^0(\vec{Q}=0) + f'(\omega) + if''(\omega) \right), \quad (2.44)$$

with the atomic number density, ρ_{atom} . The real and imaginary parts of the refractive index then read

$$\delta = \frac{2\pi\rho_{atom}r_0}{k^2} \left(f^0(\vec{Q}=0) + f'(\omega) \right), \quad \text{and} \quad (2.45)$$

$$\beta = - \left(\frac{2\pi\rho_{atom}r_0}{k^2} \right) f''(\omega), \quad (2.46)$$

with

$$f''(\omega) = - \left(\frac{k}{4\pi r_0} \right) \sigma_a, \quad (2.47)$$

where σ_a is the absorption cross-section.

2. Fundamental Concepts

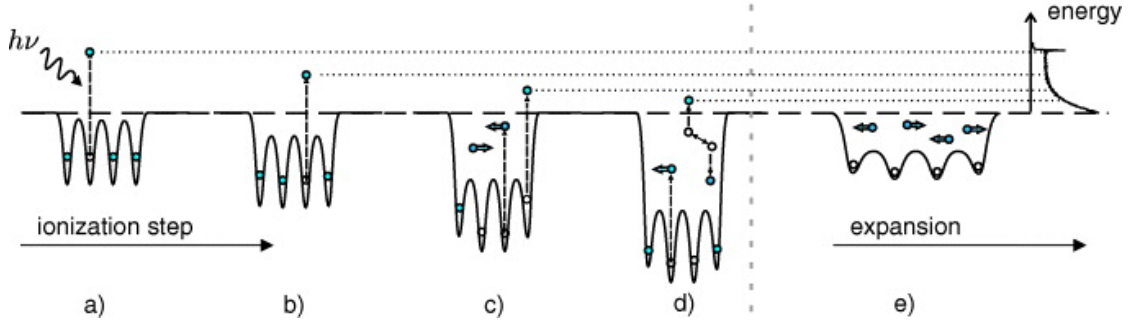


Figure 2.16.: Schematic of the nanoplasma creation and expansion. In step a) X-ray photons ionize the atoms of a cluster. b) Subsequent *multistep ionizations* try to relax the electronically excited system, deepening the Coulomb potential of the cluster. Step c) shows a deepened Coulomb potential of the cluster, due to which the multistep ionization becomes (partially) frustrated and electrons are trapped in the potential. In step d) trapped electrons collide and start to thermalize. Collisions can lead to emission of trapped electrons. e) The superheated nanoplasma starts to expand. From [99, CC-BY].

2.4. Clusters in intense X-ray pulses

The response of a cluster upon irradiation with light often differs from just the atomic response. In the soft X-ray region, the ionization of clusters is initially founded by the ionization of atoms but the sample environment and physical effects are dominated by the overall response. As discussed in Section 2.2, clusters have testbed environment properties that allow studying effects ranging from atomic, to molecular and to bulk material attributes. This is why they are an ideal testbed sample to control light-driven many-particle processes [98]. In Section 2.4.1, we summarize how rare-gas clusters respond to femtosecond long, high-intense X-ray pulses and reflect on recent experiments; Section 2.4.2 discusses how tamper layers shows evidence of how the nanoplasma expansion is slowed down.

2.4.1. Formation and expansion of a nanoplasma

The nanoplasma formation and subsequent expansion summarize the processes that are responsible for sample damage in diffractive imaging due to highly intense X-ray pulses. This section first discusses the nanoplasma formation and expansion of clusters in soft X-rays, then discusses the *electronic damage* and *structural damage* that are imposed in nanoparticles, summarizes recent experiments that study the nanoplasma evolution, and ends with some remarks for this thesis.

2.4. Clusters in intense X-ray pulses

For soft X-rays, the nanoplasma formation and expansion for clusters is schematically shown in Figure 2.16 and the following steps describe it in more detail [99, 100]. Step a) the cluster is strongly ionized. Step b), further ionization through emission of photo electrons and Auger electrons lead to a *multistep ionization* that deepens the Coulomb potential [101–103]. Step c), the multistep ionization is suppressed or, so-called, *frustrated* because the Coulomb potential depth is larger than the excess energies of photo- and Auger electrons. The emitted electrons are now trapped in the cluster potential and are *quasi-free*. As a result, the cluster forms a nanoplasma²¹. Step d), the kinetic energies of the trapped electrons is initially defined by the discrete excess energies of, e.g., the Auger electrons, but collisions with other particles lead to a kinetic energy distribution that is similar to thermal distributions and can be measured via the spectra of emitted electrons [104, 105]. Step e) An *hydrodynamic expansion* and *Coulomb explosion* are the key mechanisms that now drive an expansion of the cluster until the cluster ultimately disintegrates.

Both expansion mechanisms reasonably describe the expansion process, are not mutually exclusive, and mostly depend on sample size and irradiation technique. Regarding the sample size, large clusters tend to efficiently trap electrons in their deep Coulomb potentials that thermalize efficiently, which leads to an expansion that is rather driven by hydrodynamic forces due to comparably high electron temperatures. It has been shown that electrons thermalize on the attosecond timescale and that the energy transfer to the ions can be as fast as 50 fs [106]. Small clusters trap photo- and Auger-electrons less efficiently and electrons are free such that the heating process is suppressed. In this case, the ions see the repelling force due to Coulomb interaction of like charges [107].

We focus here on the soft X-ray wavelength range, but to give an idea of wavelength dependent aspects in the nanoplasma formation, it can be said that for optical to ultraviolet (UV) pulses, strong field ionization can lead to ionization of clusters and a subsequent nanoplasma expansion [108]. In the vacuum-ultraviolet (VUV) range, *inverse Bremsstrahlung heating* leads to efficient energy absorption in clusters and the ionization is driven by collisions inside the strongly coupled plasma [101]. In the extreme-ultraviolet (XUV) to soft X-ray range, direct photoionization and subsequent multistep ionization becomes the main driver of the ionization, as described above. However, depending on the exact wavelength, certain multistep ionization cascades are enabled [99].

²¹Plasma is another state of matter, similar to solid, liquid and gaseous, where molecular bonds dissociate and positive and negative particles are present in increasing numbers.

2. Fundamental Concepts

The nanoplasma formation affects particularly two aspects in any kind of sample: One, electronic damage; the electronic configuration of a sample changes inevitably due to photoionization and subsequent processes, which is expected to break bonds and changing scattering factors and thus limits the achievable information from diffraction images; However, these processes are well understood such that, for smaller samples, computer simulations may account for such changes [16, 20]. Two, structural damage; the nanoplasma expansion leads to structural changes due to the movement of nuclei [109]. It is currently an active field to investigate the nanoplasma expansion and determine particularly the timescales on which the expansion occurs, the effect on the measured signal, and the actual structural changes [110]. Initial experiments aimed to reveal correlations between diffraction images and ion spectroscopic data using a coincident imaging and spectroscopy technique [33, 111].

With the advent of ultrafast pump–probe techniques at XFELs, the nanoplasma expansion could be initiated in a controlled way using the pump-pulse, while the probe-pulse creates a snapshot of the nanoplasma formation and expansion. A first experiment used an infra-red-pump and soft X-ray FEL-probe pulse [112] to study the nanoplasma expansion [15]. Figure 2.17 shows diffraction images of Xe-clusters from this study. The diffraction images have been fitted with Fourier-transformed electron densities. As the time delay, Δt , between pump- and probe-pulse is varied on the hundred femtoseconds timescale, the diffraction images of the (15 to 20) nm radius Xe-cluster show declining intensities at larger spatial frequencies, q . The loss in signal could be explained through a surface softening of the electron density [113, 114]. This means for the nanoplasma expansion that initially the outer atomic layers of a Xe-cluster expand, and only at longer time delays inner atomic layers begin to expand. It remains however a question, whether the nanoplasma responds similarly to an X-ray induced formation.

So, an X-ray pump–X-ray probe study using the technique described in section 2.1.4 followed at a later time [53]. Here, a coincident measurement of Bragg powder patterns and ion spectroscopy data was performed and time delays up to $\Delta t < 100$ fs could be observed. Figure 2.18a shows the measured Bragg peaks of Xe-clusters as a function of Δt . The analyzed signal shows that the unit cell length shrinks over the time delay range $\Delta t = (0 \text{ to } 80)$ fs, which means that the cluster undergoes a *transient lattice compression* before it begins the nanoplasma expansion. This unintuitive and contradictory result is attributed to the changes in electronic configuration upon ionization. Electrons that are trapped in the cluster’s Coulomb potential have an increased mobility and are able to

2.4. Clusters in intense X-ray pulses

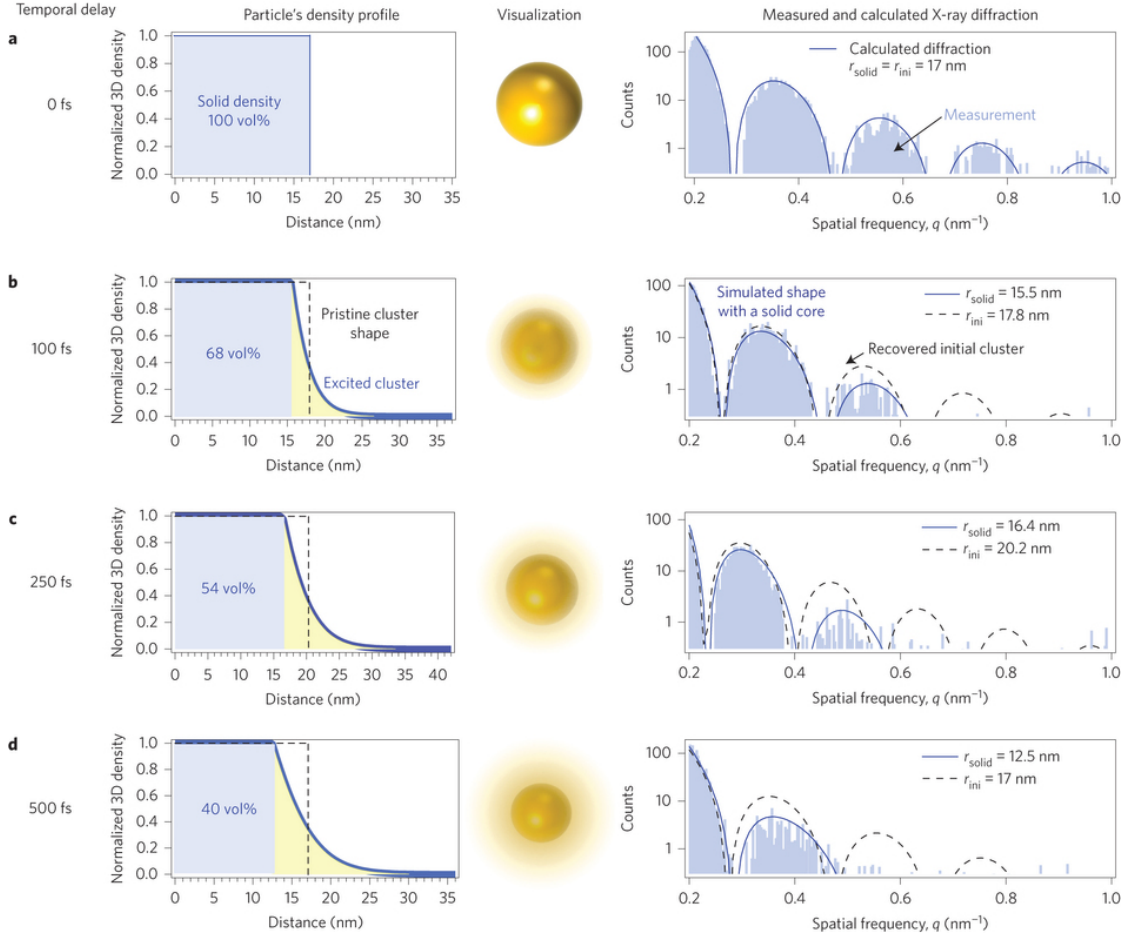


Figure 2.17.: Xe-clusters after being pumped with a NIR laser pulse and probed at a certain time delay (indicated left) with a LCLS pulse. Left series, simulation of electron densities. Right series, measured diffraction patterns. The diffraction patterns show a decrease in intensity at larger q values, when the delay is increased. This can be explained through expanding electron densities, i.e., a nanoplasma expansion. Fourier transformation of electron densities are fitted to the measurement for a solid sphere (dashed line) and an expanding sphere (solid line). From [15]. Reprinted with permission from Nature Publishing Group.

2. Fundamental Concepts

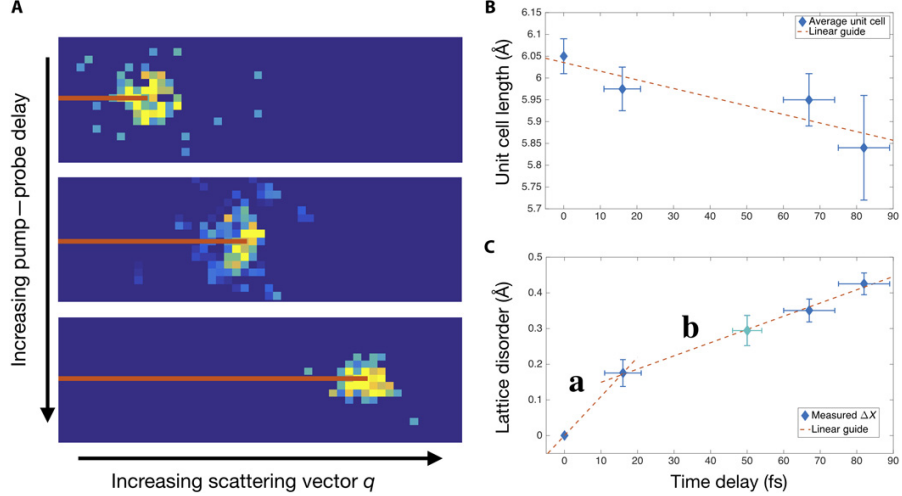


Figure 2.18.: X-ray pump–X-ray probe scattering experiment on an Xe-cluster that shows an early evolution of the nanoplasma transition. A, single-shot Bragg peaks at varying time delays. The scattering vector q increases over time delay. B, unit cell length over time delay. The clusters undergo a *transient lattice compression*. C, Lattice disorder over time delay. The measured fcc lattice is becoming disordered after being pumped with an X-ray pulse. From [53]. Reprinted with permission from AAAS.

contribute comparably to valence electrons and, therefore, change the chemical bonding character of the Van der Waals cluster. Due to the limitations in the time delay, it could not be measured whether the transient lattice compression immediately transforms into a nanoplasma expansion.

Part of this thesis is to complement and build on the results of the above studies (see Section 5.1). The in this thesis used X-ray pump–X-ray probe method (see Section 2.1.4) has similar parameters than current bio-molecule imaging setups such that a nanoplasma formation and expansion can be observed under the conditions of single molecule imaging, where radiation damage remains a major challenge. Furthermore, the pump–probe method allows a time delay range from $\Delta t = (0 \text{ to } 800) \text{ fs}$, thus extending the time delay window of above's X-ray pump–X-ray probe study.

2.4.2. Sacrificial layers slow the nanoplasma expansion

As we have discussed in the last section, radiation damage occurs as the light pulse propagates through the particle on the timescale of Auger decay rates. Thus, the principle of *diffraction before destruction* [109] demands stringent lightsource parameters

2.4. Clusters in intense X-ray pulses

to image a nanoparticle before structural damage, namely X-ray fluences of (10^{13} to 10^{15}) photons μm^{-2} and pulse lengths of a few femtoseconds or shorter [115]. But these parameters are likely not achievable with the currently planned XFEL lightsources [116]. There have been several proposals to reduce the requirements to lightsources [20] by either reducing or accounting for the effects of radiation damage. The following lists three promising candidates: One, Radiation damage effects can - in principle - be computer simulated and accounted for when imaging smaller biological molecules. Two, single particles can be aligned prior to the imaging process [115] and the known orientation of a reproducible nanoparticle in a 2D projection, i.e., the diffraction image, allows, for example, the averaging of multiple diffraction images; molecule alignment has seen some success for small molecules [17], but it is currently unknown, whether this is applicable for larger molecules. The strong light fields that are needed to align the molecules, may change the molecule's structure. Three, nanoparticles or biological molecules can be encapsulated with sacrificial layers or tamper layers [117], which slow the progress of the nanoplasma expansion. The layers supply the imaged nanoparticle with electrons and the ionized tamper layers expand first, thereby delaying structural and electronic damage of the sample. This allows longer lightpulses to perform the diffractive imaging (see Figure 1.1 and the left panel of 2.19). Part of this thesis is to show experimental evidence of sacrificial layers in supersonic gas jet injected nanoparticles (see Section 5.3ff) and is discussed in more detail below.

Initially water has been proposed as tamper layer for biological particles [117] but recent discussions [20] suggest that water tamper layers tend to become uneven in thicker layers and they are usually not uniform around the sample due to a mix of hydrophobic and hydrophilic surfaces on typical biological particles. However, it is important to have a uniform and thin tamper layer to cope with the additions from the layer to the diffraction image. These additions can be reduced by simply averaging multiple diffraction patterns while accounting for the orientation of the nanoparticle and by correcting for the average coherent additions from the layer [117, 118]. Tamper layers have been used recently [19] at FLASH²² using fixed targets that were mounted on a stage as a sample. Here, a silicon tamper layer was placed around an aluminum pillar and compared to an aluminum pillar without a tamper layer (see Figure 1.1). The effects were immediately obvious and the tamper layer ensured the sample integrity over a period of at least 5 ps after the irradiation with a 25 fs-long 13.5 nm FLASH pulse.

²²Short for **F**ree electron **L**ASer in **H**amburg. An XUV free electron laser in Hamburg, Germany.

2. Fundamental Concepts

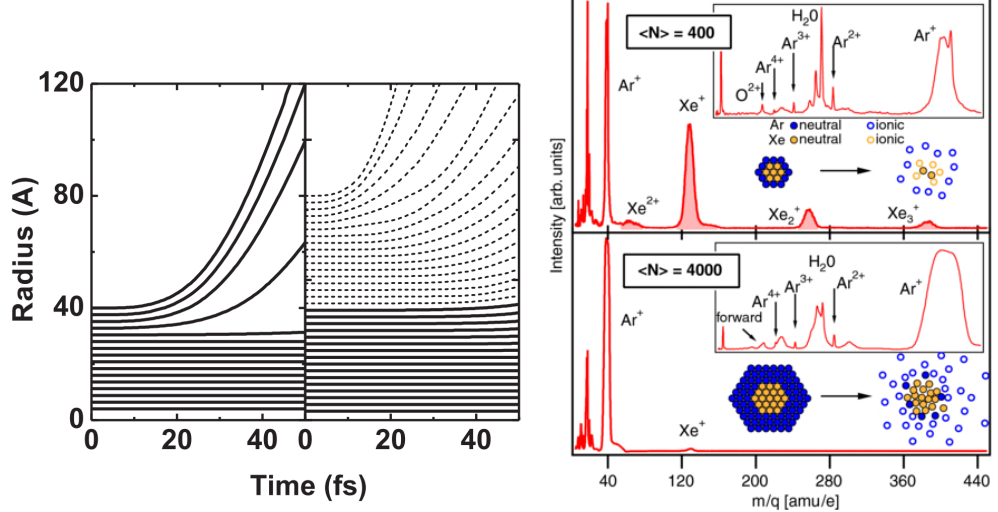


Figure 2.19.: Left panel: Simulations of atomic layers of a nanoparticle that undergoes a nanoplasma formation without tamper layers (left) and with tamper layers (right, tamper dashed line). From [117]. Reprinted with permission from APS. Right panel: TOF traces of ArXe-cluster of different sizes, $\langle N \rangle$. From [119, CC BY].

Another study [119] that is very close to the idea of tamper layers and the work described in this thesis is shown in the right panel of Figure 2.19. Here pristine Ar- and Xe- clusters as well as heterogeneous ArXe-clusters were investigated. The two rare-gases form a *core-shell system*, whereby the cluster's core consists of Xe-atoms and the shell is build of Ar-atoms. The clusters were irradiated with 93 eV photons from FLASH to undergo a nanoplasma formation and expansion. At this photon energy, dominantly xenon atoms are ionized. The experiment reveals that in smaller core-shell systems of ArXe-clusters with 400 particles (Figure 2.19 top-right panel) the time-of-flight (TOF) mass spectroscopy (see Section 3.5) data show Xe- and Ar-ions, while in larger core-shell systems of ArXe-clusters with 4000 particles (Figure 2.19 bottom-right panel) dominantly Ar-ions can be found in the TOF data. As we have discussed in Section 2.4.1, larger nanoparticles trap electrons efficiently in their deep Coulomb potential. These trapped electrons are available for recombination with other ionized atoms in the cluster. For the large ArXe-cluster, the data shows that Xe-ions recombine with the electrons that were attracted to the center of the core-shell system due to the deep Coulomb potential. Neutral xenon atoms are not detected by the TOF detector. The Ar-ions in the outer layers contributed electrons to the center of the cluster but were shed off the mixed ArXe-cluster. It is also evident that the argon atoms in the large cluster case release

2.4. Clusters in intense X-ray pulses

more kinetic energy than in the small cluster case, which is a size-dependent effect that shows an energy transfer process from the initially ionized Xe-core to the Ar-shell. Summarizing, the Ar-shell behaves as a tamper layer that reduces the nanoplasma formation of the Xe-core by transferring charges from the shell to the core, which is called *charge transfer ionization*, and transporting kinetic energy away from the Xe-core.

These are promising results that tamper layers slow and reduce the nanoplasma formation and expansion of nanoparticles that are exposed to highly intense X-ray pulses such as the ones from LCLS. While the underlying processes of a tamper layer are more and more understood and its application for diffractive imaging is widely supported, experiments have not yet produced data that comes close to the conditions of typical diffractive imaging setups at XFELs, where nanoparticles are typically injected using gas or aerosol jets to take diffraction images at high rates. The sample injection then opposes the question, which tamper material should be used and how can it be placed reproducible around a nanoparticle? Helium droplets have a long tradition to study effects of embedded species due to the unique attributes of the quantum fluid [11, 120–123]. Recently, heterogeneous HeXe-clusters were studied theoretically as a core–shell system [124] and it was proposed to use a helium tamper layer to slow and reduce the effects of a nanoplasma formation and expansion upon irradiation with an XFEL. Part of this thesis is to develop the experimental aspects of such an experiment (see Chapter 3) and analyze the effects of the helium tamper layer onto the Xe-cluster during the nanoplasma formation and expansion (see Chapters 4 and 5).

3. Experimental Considerations

The experiment described in the present thesis has been performed using the LAMP end-station of the Atomic, Molecular and Optical (AMO) Physics instrument of the Linac Coherent Light Source, which is located at SLAC National Accelerator Laboratory. SLAC was founded in 1962 as Stanford Linear Accelerator Center. The linear accelerator was early on used for high-energy physics experiments and resulted in three Nobel Prizes in Physics [125–127]. SLAC’s research topics broadened in the 1970’s and with the Stanford Synchrotron Radiation Project, it became an X-ray user facility in 1974. Meanwhile, the synchrotron source was modernized and is now known as the Stanford Synchrotron Radiation Lightsource (SSRL) and the linear accelerator was repurposed to function as the world’s first hard X-ray free electron laser - the LCLS. The LCLS began operations in April 2009 [7] and the AMO instrument started user operations in October 2009 [128]. AMO began operations with the High-Field Physics (HFP) and the CFEL¹-ASG² Multi Purpose (CAMP) end-station, which was supplied by the Max-Planck Society from Germany. The so-called “LAMP” end-station is a successor of the CAMP end-station and was commissioned in September 2013 [129]. LAMP has been in use at the AMO instrument since commissioning and the experiment described in this thesis was performed in January 2014³ in the LAMP end-station of the AMO instrument. My involvement in design discussions, the building, the commissioning, and the operation of the LAMP end-station was a significant effort during my doctoral studies and resulted - at the time of writing - in the publications [30, 47, 130–135].

This chapter is organized as follows; Section 3.1 discusses the details of the AMO instrument; Section 3.2 focuses on the specifics of the LAMP end-station; Section 3.3 goes over the pnCCD detector and its geometry; and Section 3.4 centers around relevant aspects of the sample delivery. The chapter ends with Section 3.5 that describes the time-of-flight (TOF) detector for the LAMP end-station.

¹Acronym for the Center for Free Electron Laser Science on the DESY campus in Hamburg, Germany.

²Short for the Advanced Study Group of the Max Planck Society in Hamburg, Germany.

³Experimental identifier at SLAC: AMOA1214

3.1. The X-ray beam transport to the LAMP end-station

The AMO instrument is located closest to the undulators of the LCLS at hutch 1. It is designed for soft X-ray photons in the energy range from (280 to 2000) eV [129, 136], where the beam divergence is a limiting factor for lower energies and the boron-carbide (B_4C)-coating on the mirrors leads to absorption above 2000 eV. After the X-ray pulse generation in the undulators of the LCLS, the X-rays are separated from the electron bunch using magnets, and optionally, the X-band transverse deflecting structure (XTCAV) [137] can be used to give insight into the kinetic energy and pulse duration of the electron bunch. Prior to entering the Front End Enclosure (FEE) [138], the electron beam is discarded in the electron dump such that only X-rays continue. In the FEE, the X-rays can be attenuated with either gas or solid attenuators. An X-ray pulse energy monitor, often referred to as a gas detector, measures the pulse energy of a single shot before and after attenuation [139]. Eventually, the X-ray beam is deflected through a mirror system into the desired hutch. To direct the beam to the AMO hutch, the soft X-ray offset mirrors (SOMS) are used. The SOMS are a set of four mirrors,

where the first two deflect the X-rays to the LCLS instruments that use soft X-rays, namely the AMO and the Soft X-ray (SXR) instrument [140–142]. The third SOMS mirror is a double mirror that either deflects the beam into the AMO or SXR instrument. The AMO instrument is versatile in its configuration and three different end-stations have been used so far. In historic order; one, the HFP end-station [128, 136]; two, the diagnostics (DIA) end-station [128]; three, CAMP end-station [143]; and four, the LAMP end-station [86, 129]. Today, the HFP and LAMP end-station can be combined with additional instrumentation, for example, the modernized DIA end-station or the XRSD device (see Section 2.1.4). As the experiment described in the present work has been performed with the LAMP end-station, we shall focus on that AMO-configuration from here on.

A schematic overview of the AMO beamline instrumentation in the LAMP configuration can be found in Figure 3.1. As the X-ray beam travels from the FEE to the AMO beamline, it can be viewed with a YAG crystal diagnostic viewer (D). Here the shape and position of the beam can be determined as it is several meters downstream of the SOMS such that a difference of the SOMS angle and position can be determined with sub-millimeter precision. This also reveals the alignment of the beam with respect to several differential pumping apertures that are located in the FEE. Experience shows that the X-rays should be centered to those apertures [144]. It is noteworthy already here

3. Experimental Considerations

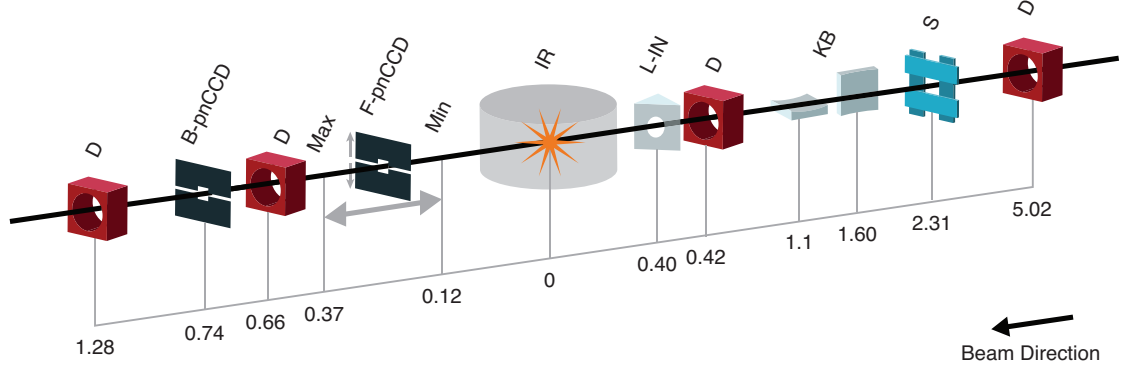


Figure 3.1.: Schematic overview of the AMO beamline instrumentation in the LAMP configuration. The indicated distances below the schematic items are in meters from the interaction region. As the X-ray beam enters the instrument, it can be visualized on a YAG crystal diagnostics (D). A set of 2 slits (S) cuts the beam in the vertical and horizontal to reduce straylight from the Kirkpatrick-Baez (KB) optics. The differential pumping section of the LAMP end-station houses another YAG crystal diagnostics (D) and an option couple in an optical laser (L-IN) on-axis with the X-rays. The front and back pnCCD (F/B-pnCCD) are located downstream of the IR with further beam viewing options (D). From [129].

that the X-ray beam became unstable and the beam's pointing became erratic. The most upstream diagnostic viewer (D) of the AMO instrument was able to detect this jitter such that the linear accelerator could be tuned to correct the erratic pointing. A beamline alignment laser, which is a typical HeNe-laser with low beam divergence, can be coupled into the beamline slightly downstream of the YAG screen⁴ such that it co-propagates with the X-rays. The X-ray beam then travels through a set of four blades (S), which are often referred to as 4 Jaw slits that can be moved independently to cut into the beam to reduce parasitic scattering⁵ originating from the Kirkpatrick-Baez (KB-)mirrors [145]. Experience shows that the blades should not cut into the main intensity profile of the beam, but rather conservatively cut into the halo of the beam. This sufficiently reduces parasitic scattering but does not reduce the peak intensity of the X-ray pulse (compare green and blue curve in Figure 3.12).

The KB-mirrors are a set of two concave mirrors that focus the X-ray beam into the interaction region. The mirrors consist of two 400 mm long silicon (Si) substrates that

⁴Not shown in Figure 3.1

⁵Parasitic scattering is often referred to as stray light.

3.2. The LAMP end-station at the AMO instrument

	pump beam	probe beam
wavelength		1.5 nm
mean pulse energy	(80 to 100) μJ	(0.8 to 1) mJ
X-ray beam FWHM		$\sim 1.5 \mu\text{m}$
pulse duration		$\sim 25 \text{ fs}$
delay Δt precision		$\sim 25 \text{ fs}$

Table 3.1.: Summary of LCLS beam parameters during experiment.

are coated with boron carbide (B4C). They reflect the X-rays in grazing incidence at 13.85 mrad and are sometimes referred to as KB-optics. The first mirror focuses the beam in the horizontal and the second mirror focuses the beam in the vertical. As the mirrors are located at different positions in the horizontal and vertical, they are designed to have a focal length of 1600 mm in the horizontal and 1100 mm in the vertical. Additionally, the mirrors can be bent to change their focusing position along the Z -axis⁶ and the optimal focus can be found and characterized through, for example, the study of time-of-flight (TOF) mass-spectroscopy [86] and imprint analysis [146, 147], which we will discuss in Section 3.6. A study of the X-ray focus is necessary to achieve the smallest focus, thereby increasing the intensities at the sample interaction region. For the experiment in this thesis, the X-ray beam focal size was determined to be $\text{FWHM} \approx 1.5 \mu\text{m}$, with an effective area of $5 \mu\text{m}^2$ [86]. The LCLS beam parameters are summarized in Table 3.1. The pulse duration was determined through analysis of the electron beam and the delay, Δt , precision is estimated from geometric considerations of the delay chicane (see also Section 2.1.4).

3.2. The LAMP end-station at the AMO instrument

Following the Figure 3.1, the X-ray beam enters the LAMP end-station after the KB mirrors (see also the overview in Figure 3.2). LAMP begins with a differential pumping (DP) section that separates the interaction (C1) and detector chambers (C2-1, C2-2) from the KB optics and other upstream beamline instrumentation. The differential pumping section consists of two small tubes, which are pumped with turbo-molecular pumps at neighboring chambers. The tubes are 5 mm, 8 mm, or 10 mm diameter differential pumping apertures (indicated in Figure 3.3). The DP stage is able to maintain over 4 orders of magnitude pressure difference, for example, the pressure in the C1 vacuum chamber,

⁶The LCLS uses a right-handed coordinate system, where the index finger (Y -axis) points up and the middle finger (Z -axis) points parallel to the X-ray beam.

3. Experimental Considerations

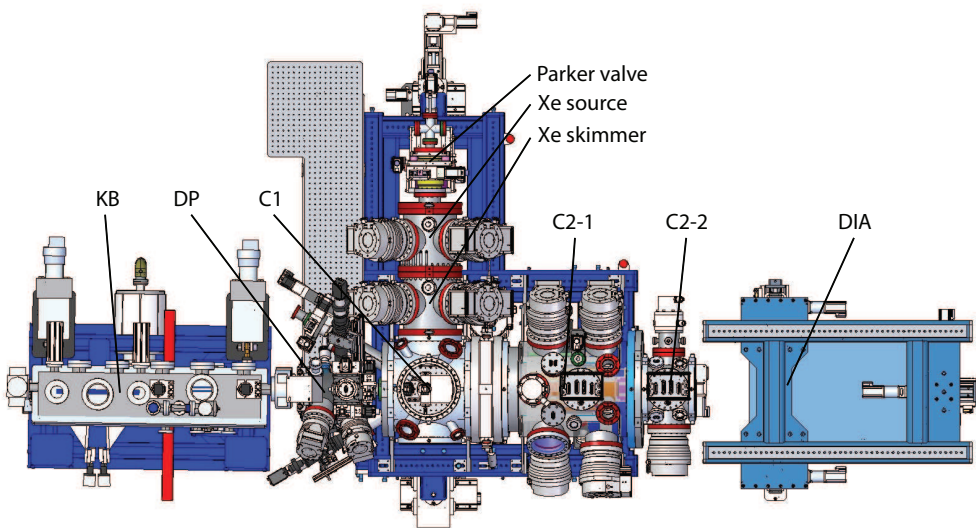


Figure 3.2.: Overview of the AMO instrument in the LAMP end-station standard configuration. From left to right, the beam propagates through the Kirkpatrick-Baez (KB) optics, the differential pumping (DP) section, the interaction chamber (C1), the front pnCCD chamber (C2-1), the rear pnCCD chamber (C2-2) and finally the diagnostics (DIA) stand. The Xe jet is also shown, including the Parker valve, Xe-source and -skimmer chamber, which are mounted on C1.

3.2. The LAMP end-station at the AMO instrument

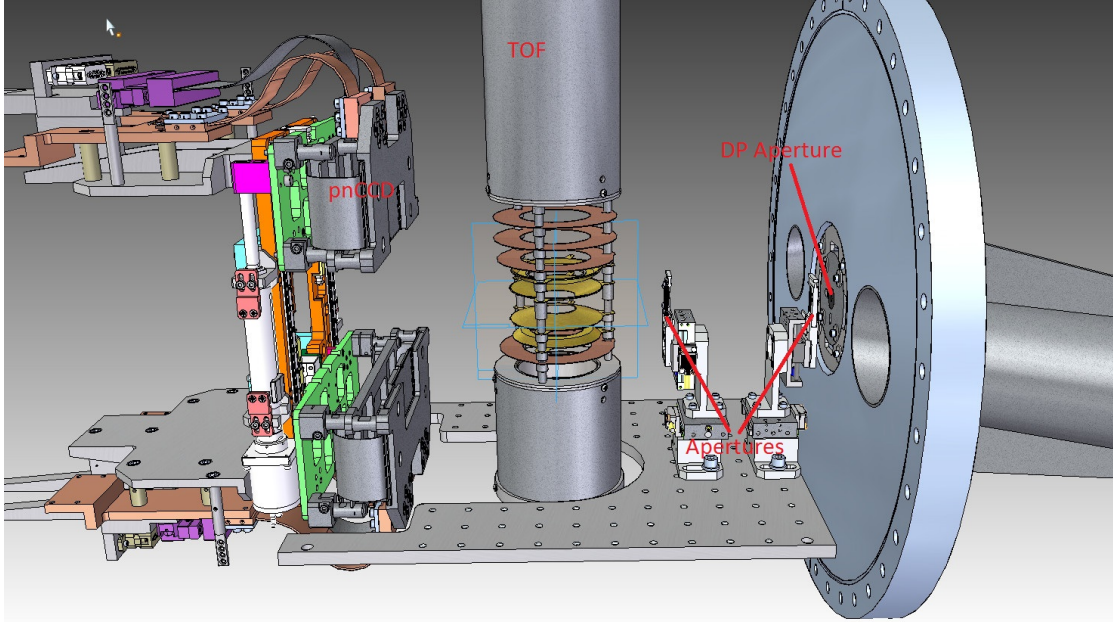


Figure 3.3.: Inside view of the C1 chamber showcasing the interaction region.

p_{C1} , may rise to $p_{C1} = 10^{-6}$ kPa as the sample injection starts and the pressure in the KB-optics vacuum tank, p_{KB} , is maintained at $p_{KB} = 10^{-10}$ kPa due to the differential pumping section. The second DP-stage chamber holds a YAG crystal to examine the X-ray beam after the KB optics and a removable laser in-coupling mirror to overlap X-rays with an optical laser or an aperture to reduce parasitic scattering from the differential pumping apertures and upstream elements.

The beam then travels into the C1 chamber that encloses the interaction region. Before reaching the sample interaction region, the beam is cut by apertures (see Figure 3.3). The apertures are mounted on encoded stages that are driven by piezoelectric actuators with sub-micron movement precision. The aperture material is silicon nitride (Si_3N_4) and has windows with tapered-edges that cut into the X-ray beam. The window-size can be fit to the size of the X-ray beam diameter, which can be estimated using geometric optics. Alternatively, oversized aperture windows can be used to drive one corner of the window on the first aperture stage and the opposite corner on the second stage into the beam, which is sometimes referred to as cornering apertures. As part of this thesis work, an improved aperture system was designed using four aperture blades with tapered edges. These allow full control over the aperture from four directions, thus allowing short aperture alignment times and a more controlled reduction of unwanted effects. For soft

3. Experimental Considerations

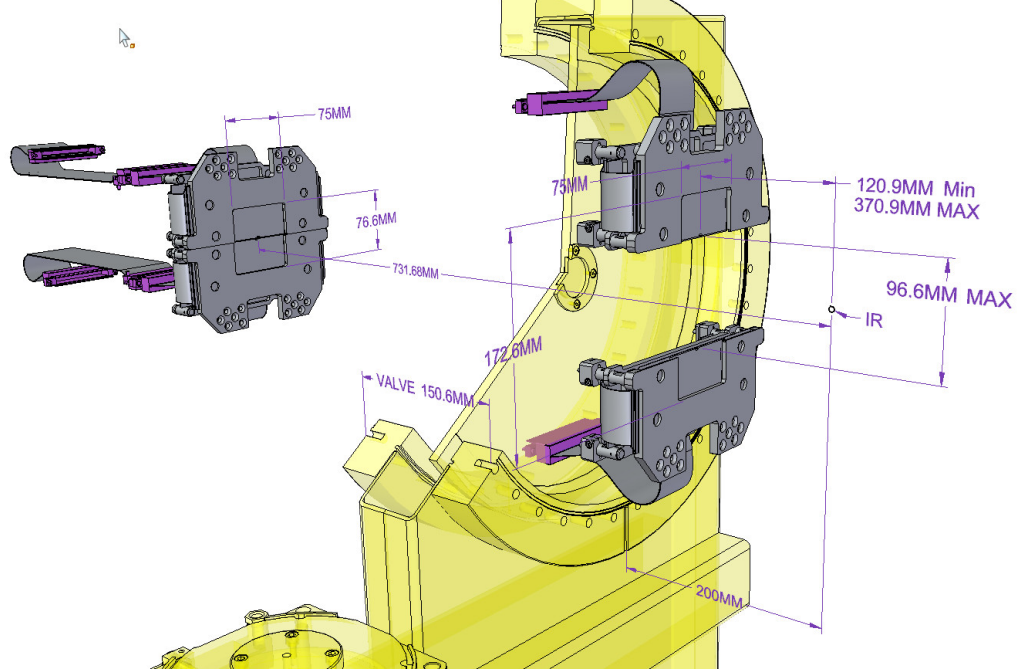


Figure 3.4.: Side view of the rear and front pnCCD detector inside LAMP. The interaction region (IR) is in the center of C1. The beam propagates along the Z-axis where the rear (top) pnCCD is placed 728.53 mm away from the IR (original engineering distances). The half detector height is 38.3 mm and results in a scattering angle of $\Theta = 4.26^\circ$. With the gate-valve installed, the front pnCCDs are able to travel along the Z-axis from 370.9 mm to 120.9 mm downstream of the IR. The front pnCCDs position along the Y-axis is adjustable and they can detect photons up to 48.3 mm from the beam axis. At maximum extension, the pnCCDs are able to detect photons up to a scattering angle of $\Theta = 38.11^\circ$.

X-rays, it is important to note that the flat side of the tapered aperture is facing the beam such that the tapered-edges are facing downstream.

In the center of C1, where sample and X-rays interact, a time-of-flight spectrometer can be installed (see Figure 3.3), which is described in detail in Section 3.5. The beam then enters the C2-1 chamber through a large gate valve. Here, a variety of distances become relevant for the digital combination of diffraction images from the front and rear pnCCD detectors that are in different planes. This algorithm is discussed in detail in Section 4.2.1. Figure 3.4 shows for this thesis relevant engineering design distances of the pnCCD detectors inside the LAMP instrument including the gate valve. The manufac-

3.3. The large area pnCCD detectors

turing size of the gate-valve along the Z -axis is 150.6 mm. The front pnCCD is mounted on a motorized stage and can be moved along the Z - and Y -axis inside the vacuum. The front-bottom pnCCD module can be set between (117.75 to 367.75) mm downstream of the center of C1. The front-top pnCCD module is 3.15 mm closer to C1. The maximum extent along the Y -axis is 48.3 mm from the beam to the onset of the detector. In this experiment, the front pnCCD modules were in the most rear position and their extent along the Y -axis was asymmetric, whereby the front-top pnCCD was 17.3 mm from the beam and the front-bottom pnCCD was 18.9 mm. The distance from the center of C1 to the bottom-rear pnCCD detector module is 731.68 mm and the top-rear pnCCD module is again 3.15 mm closer to C1⁷. A set of motorized, in-vacuum stages allow the use of another YAG crystal (D), an optical filter and a B_4C beam stop just before the rear pnCCD.

3.3. The large area pnCCD detectors

The pnCCDs are attractive photon area detectors because of the following four reasons; one, their high quantum efficiency (QE) and good signal to noise ratio; two, their read-out rate is very high – up to 200 Hz; three, their large active areas cover wide scattering angles; and four, the detectors are almost defect free after applying widely-used pixel detector image corrections. pnCCDs are originally designed to be sent into space and have found usage in astronomy and material science. The pnCCD detectors have been used first as X-ray diffractive imaging detectors at FLASH and at LCLS, namely in the CAMP instrument. At LCLS, these detectors are mostly used for X-ray diffractive imaging, but have also spectroscopic capabilities, which are demonstrated in the left panel of Figure 2.14. For this thesis, the pnCCD detectors were used to record diffraction images and are described in detail below.

Let us begin by describing the chip geometry [86]. Each front or rear pnCCD detector is made out of two modules. Figure 3.5 shows the layout of a single pnCCD module. The chip consists of 512 pixels \times 1024 pixels. Each pixel has a size of 75 $\mu m \times$ 75 μm , so the area that the detector covers is 38.4 mm \times 76.8 mm. To allow the FEL beam to travel through the instrument, each module has a rectangular region cut out in the middle of the center edge. On a single module this area is 4.5 mm \times 1.65 mm and for the whole detector this “hole” has the dimensions 4.5 mm \times ~4.5 mm. The rear pnCCD position

⁷These design distances must be extended by ~5 mm along the Z -axis due to customization during the initial setup of LAMP.

3. Experimental Considerations

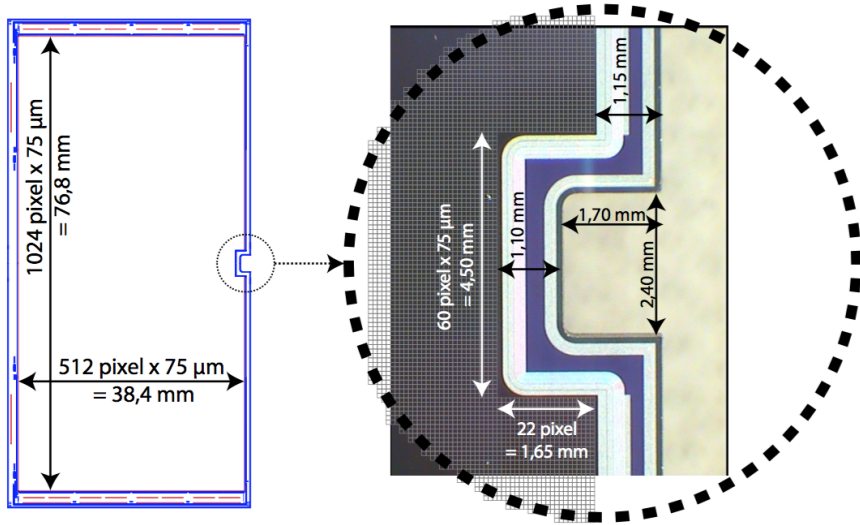


Figure 3.5.: Geometry of a single pnCCD module with a detailed view of the beam conveying hole. A single module consists of 1024 pixels \times 512 pixels. Each pixel is $75 \mu\text{m} \times 75 \mu\text{m}$, which results in an active area of $76.8 \text{ mm} \times 38.4 \text{ mm}$. The chip is surrounded by non-active edges, which are 1.15 mm wide on beam facing edges. The hole reduces the active area on one module by 60 pixels \times 22 pixels, or $4.5 \text{ mm} \times 1.65 \text{ mm}$ and allows the beam to propagate through a $2.4 \text{ mm} \times 1.7 \text{ mm}$ hole.

3.3. The large area pnCCD detectors

Key	relative gain	approx. ADU/keV	max. photons per pixel
1	1/256	5	1100
2	1/128	10	640
3	1/64	20	320
4	1/16	79	80
5	1/4	316	20
6	1	1250	5

Table 3.2.: Typical generated ADU values and dynamic range using 1k eV photons at all pnCCD gain settings. It is a valid approximation to linearly extrapolate to other photon energies.

has been chosen such that the pnCCD hole slightly oversizes the diverging FEL beam, when the focus is in the middle of the C1 chamber. The borders of each module are insensitive to photons over a width of 1.15 mm and 1.10 mm at the borders of the hole. To minimize the overall detector area that is insensitive to photons, the two pnCCD modules are mounted such that the non sensitive areas overlap. As a result of that, each top module is 3.15 mm closer to the interaction region than each bottom module. The effective gap that is seen in the laboratory frame images between each top and bottom module measures 16 pixels or ~ 1.2 mm.

The pnCCD chip is read out with a custom CMOS multichannel Analog MultiplEXer (CAMEX). Eight CAMEX are installed on each pnCCD module (indicated on top and bottom of Figure 3.5). The CAMEX performs two interesting functions; one, instead of reading out every pixel sequentially, it can read-out 128 pixel rows in parallel enabling pnCCD image read-out rates of up to 200 Hz; two, it pre-amplifies the photon signal through a set of gain amplifiers. Different gain modes can be used to be more sensitive to photons in high gains or to store more photon signal in lower gains. The following considerations are useful when combining detectors of different gain settings or arbitrary detector unit (ADU) generation. Table 3.2 shows information about the pnCCD gain settings and ADU generation. Gain $\frac{1}{1}$ is the highest gain and $\frac{1}{256}$ is the lowest gain. As one steps from highest to lower gains, e.g., from 1 to $\frac{1}{64}$, the ADU value creation per photon goes with that fraction in good approximation.

TBD The thin and unstructured radiation entrance windows have a high quantum-efficiency from the infra-red (IR) to soft X-ray wavelength range. In order to avoid unwanted scattering, the photon entrance windows are located at the back of the detec-

3. Experimental Considerations

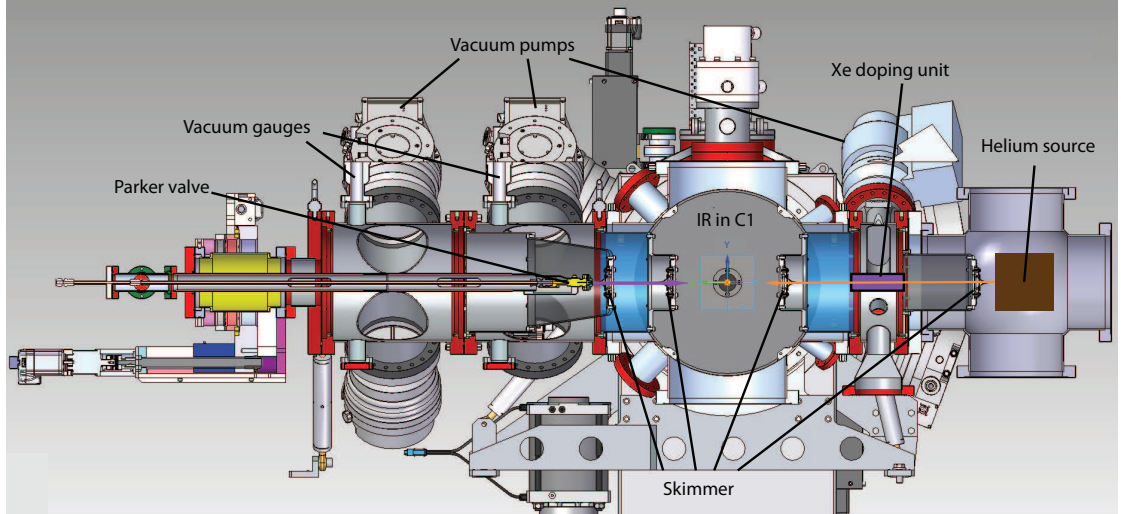


Figure 3.6.: Downward view of a slice through the interaction region in C1 of the experimental setup. The purple arrow indicates the xenon gas flow, the orange arrow indicates the helium gas flow.

tor, thus facing upstream of LCLS, and are coated with 50 nm aluminum to reduce their sensitivity from infra-red and optical light. This aluminum coating does attenuate the soft X-rays at AMO slightly but the detectors maintain a quantum efficiency of $\sim 90\%$. At AMO, it is thus possible to linearly extrapolate the generated ADU values to other photon energies, for example, a 1.5 keV photon will generate approximately 1750 ADU in highest gain (compare Figure 2.14). The in this thesis used 837 eV photons will approximately generate ~ 1087 eV. There is also an optical aluminum filter mounted from the front of the chip, thus facing downstream of LCLS, to drastically reduce wrongly directed scattering.

3.4. Sample delivery

Two gas sources are used in order to create single rare-gas clusters. Single xenon and helium clusters are produced using the principle of the supersonic gas expansion into a vacuum that is described in Section 2.2.1. Helium clusters that are doped with xenon are produced through the pickup principle as described in Section 2.2.2. Given the time constraint of performing experiments at the LCLS, both sources are installed in one setup and operate independently, allowing quick sample changes. A schematic setup of the sample environment can be found in Figure 3.6 and a list of used vacuum pumps can be found in Table 3.3.

3.4. Sample delivery

Chamber	Turbomolecular pump mod.	Roughing pump mod.
Xenon source	4x Leybold Turbovac TMP 361	
Xenon skimmer	2x Leybold Turbovac Mag W 300 P	
Helium source	2x Leybold PK-S 1300	adixen ACG600
Helium skimmer	2x Pfeiffer HiPace 300	
LAMP C1	1x Pfeiffer HiPace 700	
LAMP C2-1	4x Pfeiffer TC 400	adixen ACP 120G

Table 3.3.: Installed vacuum pumps per chamber in the experiment.

The AMO cluster source, which produces a single xenon cluster, consists of a Parker-Hannifin Series 99⁸ - pulsed valve using a solenoid with a custom manufactured conical copper nozzle, two vacuum chambers to mount two skimmers, a third adjustable piezo-slit skimmer and several vacuum pumps. It is a well-characterized source that was used extensively in the past [15, 33, 53, 76, 129]. The pulsed solenoid valve (see Figure 3.7) is controlled and operated by a Parker-Hannifin Iota One pulsed-valve driver. The valve driver applies a current to the solenoid, a magnetic cylinder actuates and the attached poppet opens and closes again after a set TTL signal from the driver. The valve's opening time is set to 1 ms and repetition rates of up to 30 Hz can be set at a xenon reservoir pressure range of (1 to 20) bar. The pulsed valve heats up substantially during operations and due to material deterioration and the vespel poppet is replaced every \sim 60 h of operating time, or as needed to prevent a leakage from the gas source. The nozzle has a 200 μm opening diameter and an opening half angle of 4°. It is clamped to the Parker valve using an indium gasket to seal. Two skimmers with an opening of 1 mm diameter and an adjustable piezo-skimmer have been installed to define the gas jet. The piezo skimmer allows fine control over the slit opening formed by two razor blades. The blades can be closed by applying a voltage, U , from (0 to 8) V. At $U = 8$ V, the cluster source operates in the single cluster regime. The background pressures in the respective source and skimmer chambers is handled through turbo-molecular pumps that are connected to roughing pumps (see Table 3.3). Ultimately, these chambers lower the gas pressure in the interaction region, p_{IR} , or C1 chamber to $p_{\text{IR}} \leq 10^{-5}$ bar.

Helium droplets are produced in a continuous free gas expansion using an electron microscope diaphragm as nozzle (Plano A0200P) that has a 5 μm orifice and an orifice channel length of \sim 2 μm [65]. The nozzle is cooled to cryogenic temperatures $T = 5.8$ K using a Sumitomo cold-head. The particle beam is defined by a first 0.5 mm and a second 1

⁸Series 99 is at the time of writing not produced/advertised as a straight, in-line pulsed valve anymore.

3. Experimental Considerations

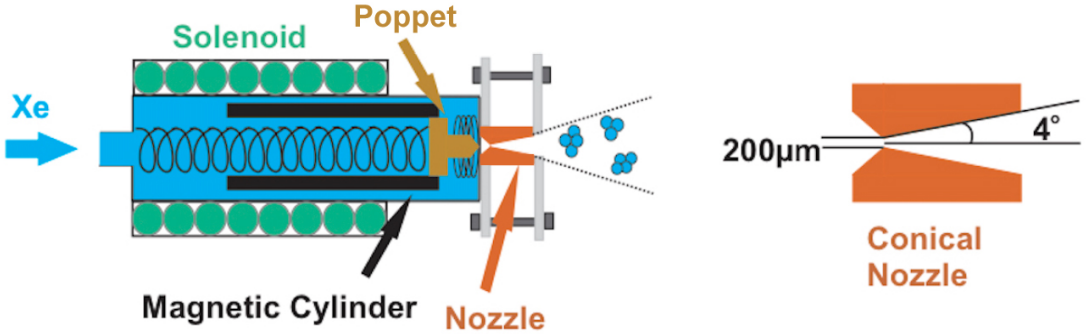


Figure 3.7.: Schematic of the Parker-Hannifin Series 99 pulsed in-line valve and custom copper nozzle. The nozzle is clamped to the pulsed valve using an indium gasket to seal. The vespel poppet is attached to the magnetic cylinder and closes the valve. If a current is run through the solenoid, the valve actuates and opens. Adapted from [80,].

mm diameter skimmer. As explained above, a third piezo-skimmer allows the definition of the gas jet to single helium droplets. A doping unit is installed in the skimmer chamber of the helium source. The doping unit is a separate, smaller chamber in the skimmer chamber, where He-clusters can traverse through. The gas cell allows locally increasing the pressure of the cell with gaseous xenon to $\leq 3 \cdot 10^{-6}$ bar. The pressure is manually controlled using a leak valve. Since the gas load is confined in the doping unit, the vacuum system is not overloaded. As shown in Figure 2.10, the partial helium pressure is determined with a residual gas analyzer (RGA) in the source chamber of the AMO cluster source, which can then be used to determine the depletion of the helium cluster through the pickup of xenon atoms. A thorough alignment of the sources is necessary to overlap the particle beams such they traverse through all skimmers.

3.4.1. Sample jet timing at LCLS

Pulsed gas jets such as the one using the Parker solenoid valve require an electric trigger to open the valve. At LCLS, an event generator sends a fiducial, i.e., a clock signal with 360 Hz, and several event codes, e.g., at 120 Hz, to an event receiver (EVR) over a fiber network with a 10 ps precision [148]. The EVR processes these signals and systems in need of an electric trigger can be connected to the EVR to receive a specific one. The triggers coming from the EVR are based on specific event codes (ECs), for example, EC 40 operates at 120 Hz and may be delayed with respect to the EC. Figure 3.8 schematically illustrates the timing system. Following the figure, the process starts with a fiducial, an

3.4. Sample delivery

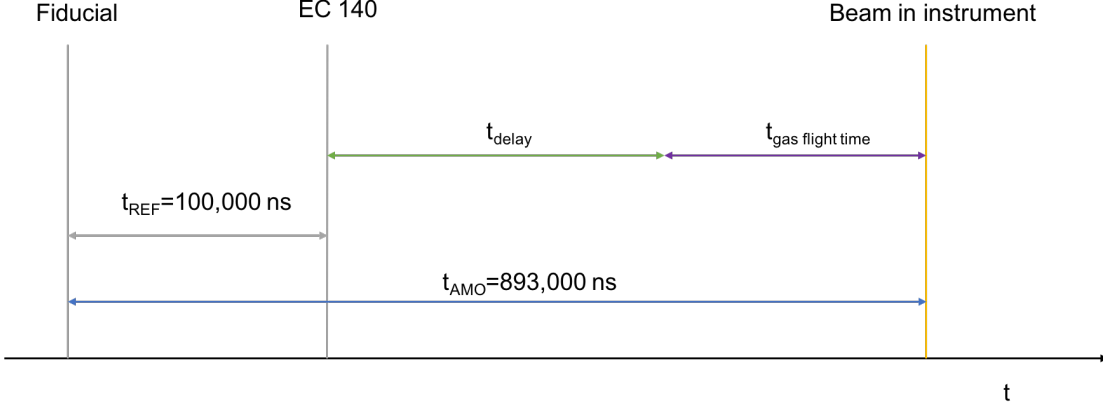


Figure 3.8.: Schematic of LCLS EVR timing system.

EC is delayed by time of event code x (TECx) and after a certain time of the fiducial a LCLS pulse arrives. At the AMO instrument, this time is $t_{\text{AMO}} \approx 893000 \text{ ns}$ ⁹. The LCLS control system automatically corrects for different TECx by internally correcting the delay to a reference time t_{REF} that corresponds to EC 140, which occurs on 120 Hz, when the beam is present. The reference time is set to $t_{\text{REF}} = 100000 \text{ ns}$ and thus we can write down the following equation for the delay time of the trigger for a sample jet at LCLS to coincide with the beam.

$$t_{\text{delay}} = t_{\text{AMO}} - t_{\text{REF}} - t_{\text{gas flight time}}, \quad (3.1)$$

with t_{delay} being the delay value for the LCLS EVR control system and $t_{\text{gas flight time}}$ the flight time of the sample from the gas source to the interaction region (IR). As described in [66], the terminal velocity v_∞ of a sample from a supersonic jet is

$$v_\infty \approx \sqrt{\frac{2RT_0}{m} \left(\frac{\gamma}{\gamma - 1} \right)}, \quad (3.2)$$

with the universal gas constant R, the temperature in the stagnation chamber T_0 and the ratio of specific heats $\gamma = \frac{c_P}{c_V}$, which is $\gamma = \frac{5}{3}$ for monoatomic gases such as rare-gases. The flight time of a certain gas can then be calculated by measuring the distance, D , between the source and the interaction region, thus $t_{\text{gas flight time}} = \frac{D}{v_\infty}$. The approach may be extended to approximate flight times of molecules, e.g., using the mass of CO, $m_{\text{CO}} = 28 \text{ amu}$, and also to gas mixtures, for example, the mass of a 2% xenon-131 and

⁹Times are in nanoseconds (ns) and in a format to comply with the LCLS interface.

3. Experimental Considerations

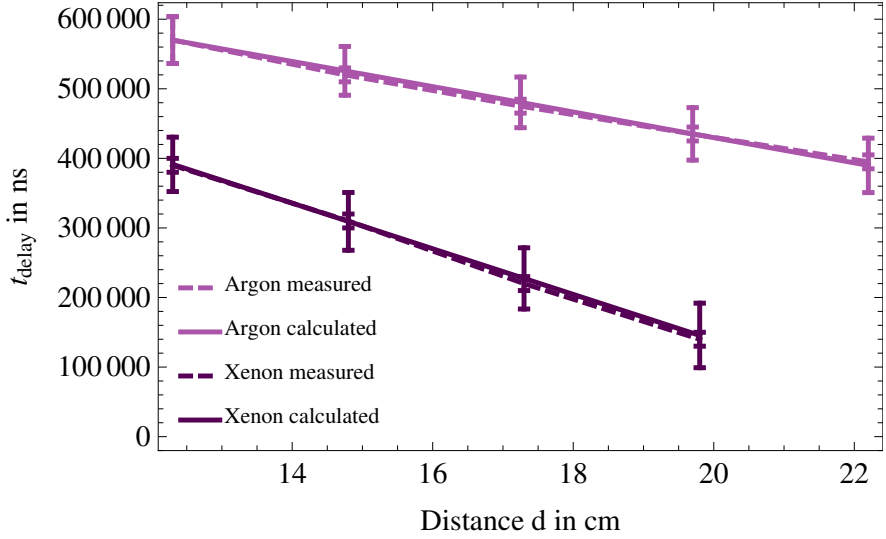


Figure 3.9.: t_{delay} as a function of the gas source distance to the interaction region. Xenon and argon has been used as sample gas in an Even-Lavie pulsed valve. The calculated delay values (solid lines) agree well with the measured delay times (dashed lines) to overlap the onset of the pulsed jet with the laser.

98 % helium-4 gas mixture can be estimated using a weighted average according to their relative contributions, thus $m_{\text{HeXe}} = 6.54 \text{ amu}$.

Figure 3.9 shows measured and calculated flight times using an Even-Lavie (EL) supersonic gas source¹⁰ instead of the earlier described Parker valve. The Evan-Lavie source has a very well-defined opening time of 22 μs and thus a well-defined gas jet, which can be time consuming to trigger properly without knowing t_{delay} . The data show very good overlap of the calculated delay times t_{delay} and ion yield maximum of the particle beam. The calculated flight times include an error margin, which can also be read as a recommended scan range. While the electric triggering and actual valve opening times may add errors on the microsecond time-scale, uncertainties in temperature and distance from nozzle to IR change delay times drastically. For completeness, the terminal velocity of argon is $v_{\infty, \text{argon}} = 512 \frac{\text{m}}{\text{s}}$ and of xenon is $v_{\infty, \text{xenon}} = 305 \frac{\text{m}}{\text{s}}$ at room temperature.

Very long flight times can occur when heavy gases, such as xenon, are used or long distances, D , are necessary. If the flight times $t_{\text{gas flight time}} > t_{\text{AMO}} - t_{\text{TREF}}$ the system has to be delayed onto the next event as negative delays are not possible in the LCLS timing

¹⁰The EL-valve has the serial no.: EL 5 HRR NO 114.

3.5. Time-of-flight mass-spectrometer

scheme and Equation (3.1) can be rewritten to

$$t_{\text{delay}} = \frac{1}{f_{\text{rr}}} + t_{\text{AMO}} - t_{\text{REF}} - t_{\text{gas flight time}}, \quad (3.3)$$

with f_{rr} being the repetition rate of the event code.

3.5. Time-of-flight mass-spectrometer

An ion time-of-flight spectrometer was used in the interaction region to detect xenon and helium ions. A time-of-flight spectrometer uses electric fields to accelerate ions from the interaction region towards a detector. The detector unit often consists of a micro-channel plate (MCP) that allows a position sensitive detection of the particle signal. In the first stage, the ions are accelerated from the IR towards the detector. Here, the electric potential energy is converted into kinetic energy

$$qU = \frac{1}{2}m \left(\frac{d_1}{t_1} \right)^2, \quad (3.4)$$

$$t_1 = \sqrt{\frac{m}{2qU}} \cdot d_1, \quad (3.5)$$

with q being the elementary charge of the ion, U the voltage difference, d_1 the distance between the IR and spectrometer, m is the mass of the ion, and t_1 is the time-of-flight in the acceleration stage. The ions then travel through a drift tube of length d_2 that is field free. As the velocity remains constant, we can write down

$$t_2 = \sqrt{\frac{m}{2qU}} \cdot d_2, \quad (3.6)$$

with t_2 being the time-of-flight in the drift tube. The total flight time can then be written as

$$t_{\text{time-of-flight}} = t_1 + t_2 = \sqrt{\frac{m}{2qU}} (d_1 + d_2), \quad \text{and explicitly} \quad (3.7)$$

$$t_{\text{time-of-flight}} \propto \sqrt{\frac{m}{q}}. \quad (3.8)$$

Typical for an experiment, all values aside from m and q can be considered constant. As the spectrometer is a cylindrical system, the time-of-flight denotes the final position on the detector and vice versa. Therefore, the position sensitive MCP yields insight into the $t_{\text{time-of-flight}} \propto \sqrt{\frac{m}{q}}$ of the ensemble of ions in the IR upon interaction with an X-ray

3. Experimental Considerations

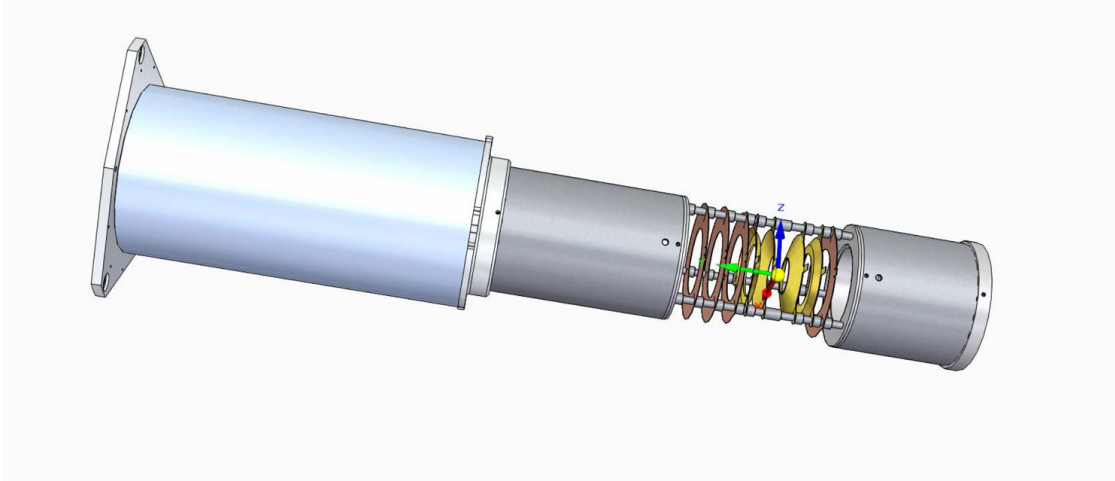


Figure 3.10.: Drawing of the time-of-flight spectrometer.

pulse. Usually, ions start with a kinetic energy $E_{kin} \neq 0$, such that the flight times are altered. This results in a distribution of the ion signal instead of a strict peak structure. Atomic ion time-of-flight data typically exhibits a distinct peak structure while the signal from clusters is strongly broadened due to kinetic energy release from collective effects. Using this information, element specific data including insight in the ionization cascades can be gained [149].

The configuration of the here used time-of-flight spectrometer is depicted in Figure 3.10. It consists of an electron and a, longer, ion side. With ± 5 keV power supplies, ions can be detected up to kinetic energies of 50 eV with a time-of-flight resolution of 100 ps [129]. If only the ion side is used, ions with kinetic energies of up to 100 eV can be detected. The use of ± 10 keV power supplies allows a detection of kinetic energies up to 150 eV. Electrons can be measured up to kinetic energies of 150 eV using ± 5 keV power supplies, 300 eV if only the electron side is used and 400 eV when using ± 10 keV power supplies. Ions and electrons can be detected whether they are emitted in any direction, in other words the spectrometer has a 4π solid angle collection [150]. A side view of the spectrometer can be found in Figure 3.11. Ion, electron and photon trajectories upon interaction with a LCLS pulse have been simulated using SIMION. A conical lens stack avoids casting a shadow on the pnCCD detectors (top of image). The applied voltages in the experiment can be found in Table 3.4. Here, the electron side is powered to have unperturbed electric fields across the interaction region.

3.5. Time-of-flight mass-spectrometer

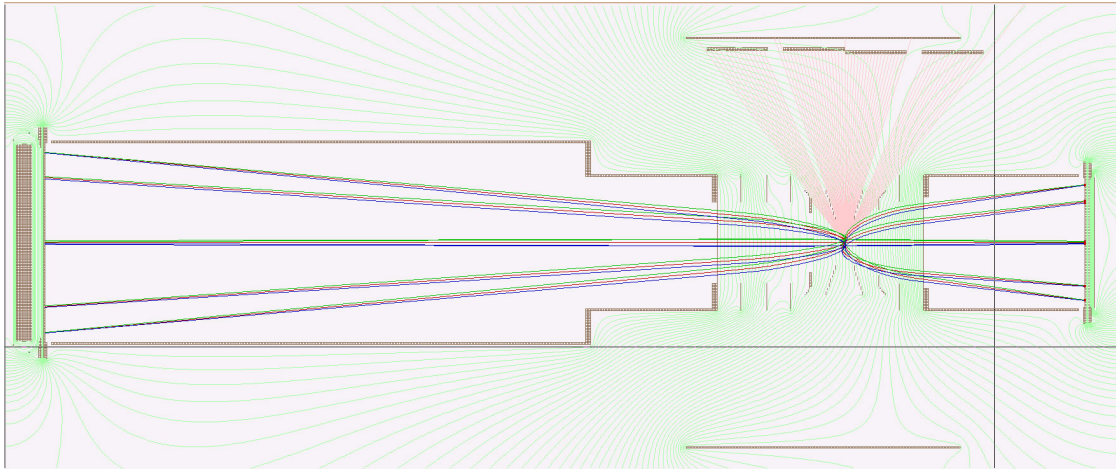


Figure 3.11.: Sideview of the spectrometer showing ion, electron and photon trajectories upon interaction with LCLS. The image was created with SIMION. From [150].

Ion-side Connection	Voltage in V	El. Side Connection	Voltage in V
MCP Front	-2600	MCP Front	200
MCP Back	5	MCP Back	2200
Holder	200	Phosphor	3000
Conical lens 70deg	-923	Holder	6000
Conical lens 53deg	-1393	Conical lens 70 deg	500
Flat lens #1	-1490	Conical lens 53 deg	1370
Flat lens #2	-1564	Flat lens	1940
Flat lens #3	-1639	Flight tube	2736
Flight tube	-1714	-	-

Table 3.4.: Applied voltages to the time-of-flight spectrometer (ion side use only).

3. Experimental Considerations

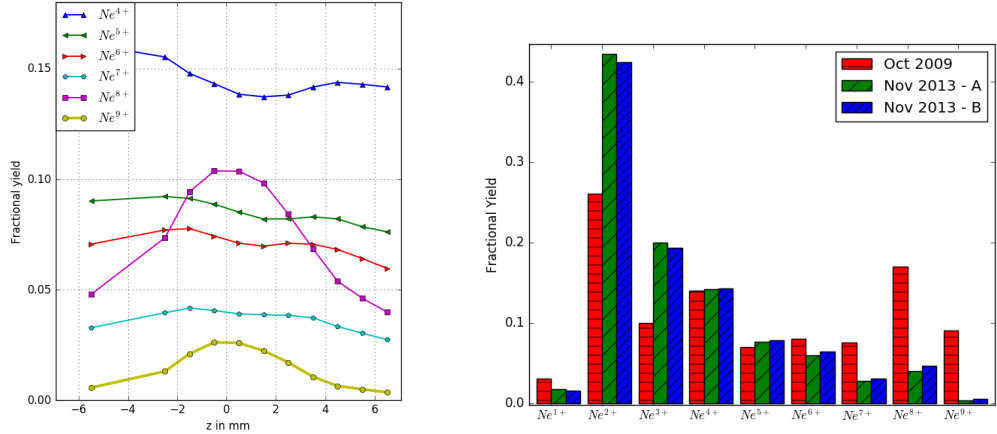


Figure 3.12.: Left graph: Atomic neon charge state yield from TOF as a function of Z-position, relative to optimal focus position $Z = 0$. $Z = 0 \pm 1$ mm is a favorable length for sample injection. Right diagram: Comparison of atomic neon charge state yield from TOF for different cases. Red: Experimental data from October 2009 with 4 blades (S) opened. Green: Experimental data from November 2013 with (S) closed. Blue: Experimental data from November 2013 with (S) opened.

3.6. Focus characterization

3.6.1. Focus characterization using a TOF spectrometer

The left panel in Figure 3.12 shows a focus characterization along the Z-axis using a TOF spectrometer. The fractional neon ion yield per charge state is summed and plotted as a function of Z-position. A 2 mm region centering around the focal plane at $Z = 0$ mm was located, where the beam was suitable for the experiment. The right panel of Figure 3.12 compares the fractional neon ion yield at the optimal focus position from November 2013 [86] to October 2009 [151]. The comparison reveals that high-charge states of neon, for example, Ne^{8+} and Ne^{9+} , are less frequent. We attribute this to deteriorated beamline optics.

3.6.2. Focus characterization via imprint study

The panels a) to d) in Figure 3.13 show images from an optical microscope of the result of a LCLS X-ray pulse at 1600 eV interacting with a lead tungstate ($PbWO_4$) sample at

3.6. Focus characterization

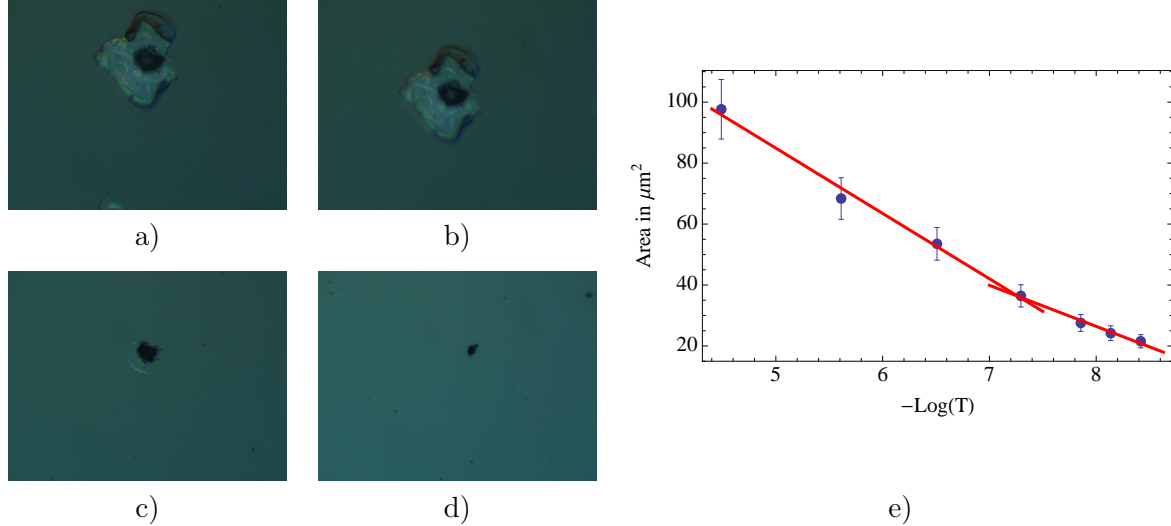


Figure 3.13.: a)-d) Ex-situ microscope imprint study of a lead tungstate (PbWO_4) sample that was irradiated with single, 1600 eV LCLS pulses at different gas attenuation. e) Non-linearity in Liu plot due to LCLS's super-gaussian beam profile. The approximate $\text{FWHM} \approx 3.4 \mu\text{m}$ is determined from the slope of the linear fits, see more in text.

different transmission values, T . We can describe the energy fluence, $E(R)$, as

$$E(R) = E_0 e^{\frac{-R^2}{2\sigma^2}}, \quad (3.9)$$

with the radial coordinate R , a characteristic radius σ , and the peak fluence E_0 . Typically, σ stays a constant beam parameter, but different peak fluences change the crater-area in the sample, e.g., more peak fluence usually increases the crater-area as more of the PbWO_4 surface is irradiated with power densities above the damage threshold. We can measure the peak fluence, E_0 , through to the pulse energy, E_p , which is measured with the gas detector. Let us explicitly note the proportional dependency, $E_p \propto E_0$. Now, we can express the peak fluence more conveniently in terms of the pressure, p , in the gas attenuator

$$\log(E_0) = \log(E_{\text{in}}) + \log(T) = -p \cdot c + \text{const.}, \quad (3.10)$$

with the peak fluence into the gas attenuator E_{in} and the transmission T . In the gas attenuator, the transmission is $T = e^{-p \cdot c}$ and a constant c . The constant c can be derived from [152]. For the LCLS attenuator filled with nitrogen gas (N2) over its 410 cm length at 1600 eV photon energy, $c \approx 0.5611415 \text{ Torr}^{-1}$. We can further approximate the crater surface area using a circle. The area then is πr_0^2 , with the crater radius r_0 . As shown

3. Experimental Considerations

in [153], $r_0^2 = 2\sigma^2 \log(\frac{E_0^2}{E_0^1})$, with $E_0^{1/2}$ being the peak fluence at two different attenuation levels. Thus, the slope of a linear fit between the two points $E_0^{1/2}$ is $2\pi\sigma^2$. The full-width at half-maximum (FWHM) is $\text{FWHM} = 2\sqrt{2\ln(2)}\sigma$. Figure 3.13 right shows the crater-area as a function of $-\log(T) = p \cdot c$ (Liu's plot) and is fitted with two linear fits. The data indicates non-linearities that come from a super-Gaussian beam-profile [154, 155]. In this data set, using the slope of the linear fit at smaller transmissions, a $\text{FWHM} \approx 3.4 \mu\text{m}$ is determined.

4. Methods

Let us conservatively estimate how much data is produced when using the LAMP end-station with both pnCCD detectors at a 120 Hz. Each pnCCD produces 120 images per second, each image is in a 32 bit-per-pixel format such that an image is approximately 4 megabyte in size. So, every minute the front & rear pnCCD produce approximately 60 gigabytes of data or 700 gigabytes per 12h shift. To analyze these vasts amount of data, an extensive set of methods and optimized algorithms is required. This chapter is devoted to illuminate the analysis methods used in the present thesis and it is organized as follows. Section 4.1 describes the general LCLS computing environment to establish an overview of the hard- and software capabilities. Section 4.2 discusses corrections that are applied to the raw pnCCD images. Section 4.3 goes over used phase-retrieval algorithms and Section 4.4 discusses simulations of 2D projections of spheres and corresponding diffraction patterns. The Section 4.5, discusses the Acqiris data acquisition and sampling, while Section 4.6 evaluates several hitfinding methods.

4.1. The computing environment at LCLS

As estimated above, the vast amounts of data generated by many detectors are unwieldy to handle by a single group of scientists that perform experiments at LCLS. For this reason the LCLS data acquisition (DAQ) group has incorporated many detectors, for example, the pnCCD and Acqiris digitizer into their framework. All data taken at LCLS is stored in the LCLS computing environment, where the data can also be analyzed. As indicated in Figure 4.1, DAQ readout nodes send the data traffic via Ethernet to a short-term cache and fast feedback (FFB) layer. While the data is being transferred, online monitoring nodes are able to 'see' a fraction of the live (online) data and run analysis. With a delay of a few tens of seconds, the FFB nodes can be used to run analysis on the full data stream using parallelization, thereby having 'online' and 'offline' data access. Eventually, the data is moved to the 'offline' layer, where the data is managed by an integrated Rule-Oriented Data System (iRODS). The data is stored in .XTC file containers and it can also be accessed from outside SLAC (Router & ESNET).

4. Methods

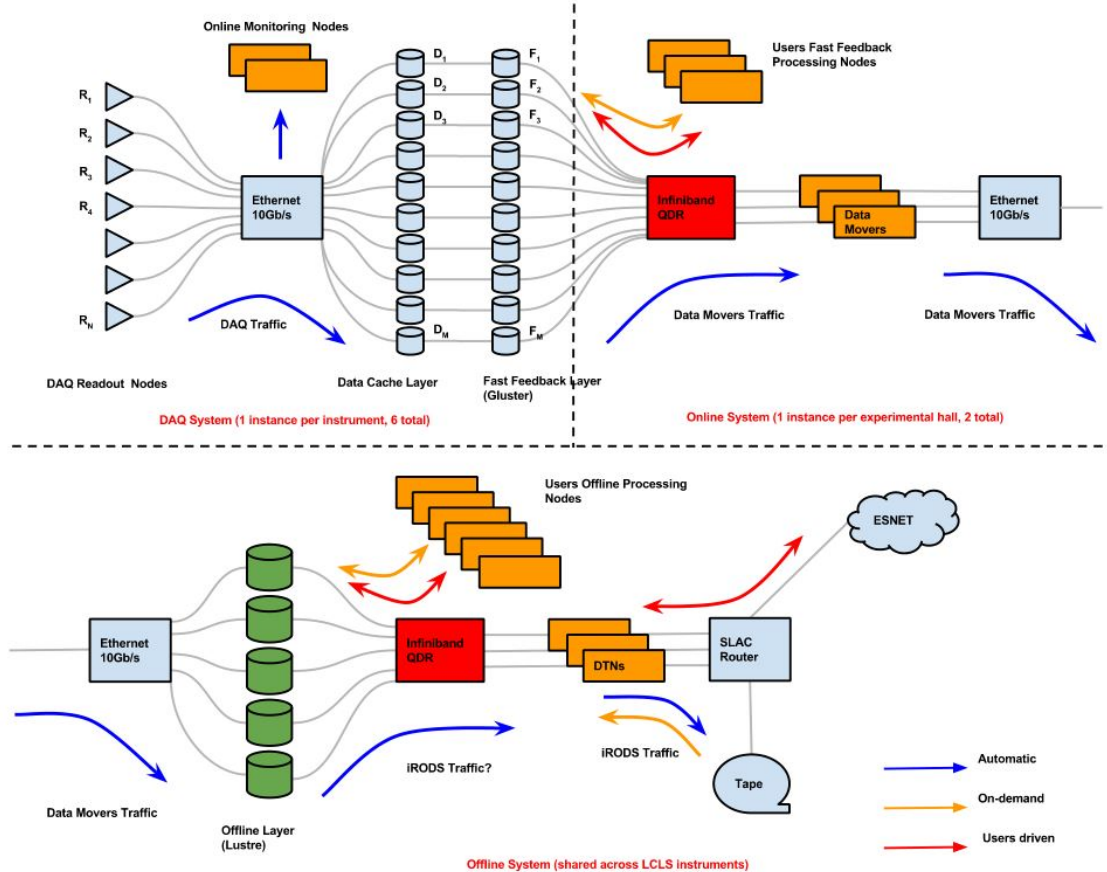


Figure 4.1.: Diagram of the computing environment at LCLS and DAQ traffic. The recorded data is exchanged through Ethernet and after digitization, is stored on a cache and FFB cluster, where psana computer have access to the online environment during the experiment. Eventually, the data is moved to the more permanent offline environment, where data can be analyzed on psana computers or through a load sharing facility. See more in text. From [156].

4.2. *pnCCD* photon detectors

The stored data has certain storage quotas and times. In brief, there is a six month short-term storage without quota limitations and a two-year medium-term storage with a storage quota of ten thousand gigabytes. After that, the data is automatically stored for at least ten years on magnetic tape (long-term storage) and can be restored upon request. A web interface is provided by the DAQ group to simplify and automate the data-handling and logging process. The short- and medium-term storage solutions can also be used to analyze the data using the Psana¹ software package [157] to access data and to perform computations on the psana computer cluster with over one thousand CPU cores. A load sharing facility (LSF) allows the scheduling of (parallelized) batch jobs. The psana-framework can be interacted with via python 2.7. The interacting python script calls functions within the psana-framework that are programmed in C(++) , for example, detector calibrations. Psana allows parallelization via MPI and it is therefore possible to analyze many events (LCLS pulses) simultaneously. Also complex analysis is able to be processed at the rate of the incoming data using MPI, when the fast feedback buffer (FFB) is used. Python scripts can be written for 'online' or 'offline' analysis and are of similar syntax.

For LCLS-II [156], the analysis and data-access scheme is designed to be similar to Figure 4.1 with the exception of the online monitoring nodes. It is therefore recommended to build analysis schemes that are based on psana and use the FFB for online analysis, which can then be adapted easily for offline analysis as well. A quick introduction on how to use psana can be found at <https://confluence.slac.stanford.edu/display/PSDM/LCLS+Data+Analysis> (from Dezember 2016).

4.2. **pnCCD** photon detectors

Before the pnCCD detectors can be used to take data, it is good practice to apply corrections to the raw detector image in order to cope with electronic noise. Since these corrections are used often, the LCLS detector and DAQ group has implemented a calibration manager tool² that provides the necessary algorithms and helps with the procedure of applying image corrections and more. We discuss the two most-often used corrections next. The first, corrects for the electronic noise pedestals (levels) of each pixel, and, the second, accounts for common modes, e.g., artifacts from the read-out electronics that

¹Psana is an acronym for Photon Science Analysis.

²The calibration manager tool 'calibman' can be found in the 'psana' software package. More information under <https://confluence.slac.stanford.edu/display/PSDM/Calibration+Management+Tool> (Oct 2016)

4. Methods

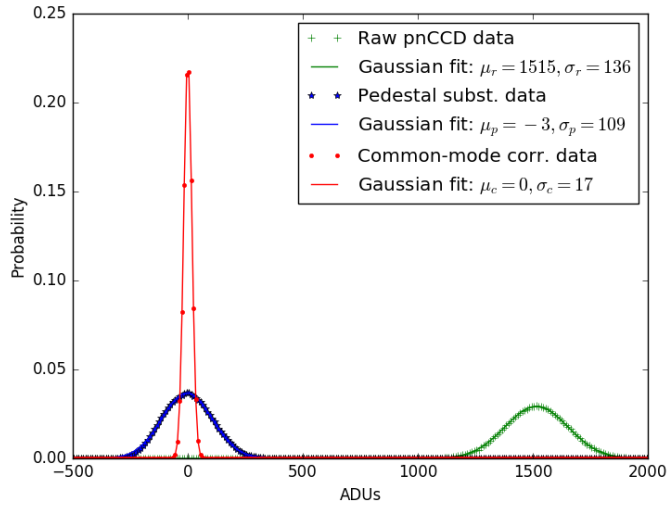


Figure 4.2.: ADU histograms from electronic noise of not illuminated pnCCDs in highest gain mode. The green plus symbols reflect a histogram of ADU values from raw electronic noise of pnCCD pixel. The noise is set off zero at $\mu_r = 1515$ ADU and has a standard deviation $\sigma_r = 136$. The same data shifts to the blue stars after applying a pedestal subtraction. The noise is centered around $\mu_p = -3$ and its standard deviation is reduced to $\sigma_p = 109$. For the red data points, the common-mode corrections have been applied. Now, the noise is well-centered at $\mu_c = 0$ ADU and σ_c is significantly reduced to 17.

appear, for the pnCCD, in columns.

The effects of applying these corrections are illustrated in Figure 4.2 through a set of histograms. The histogram bins are showing ADU values from dark pnCCD images in highest gain. The green curve shows the ADU values of a raw detector image where no corrections have been applied and the electronic noise response from the chip has a standard deviation of $\sigma_r = 136$. Note, that there is also a significant offset of the distribution from 0 to $\mu_r = 1515$ ADU. The blue curve shows the same data but is using the pedestal corrections found in 'calibman'. The pedestal corrections reduce the noise slightly to $\sigma_p = 109$ ADU, and as expected, the pedestal corrections drastically move the normal distribution to be centered around $\mu_p = -3$. Finally, the red curve is also the same data than the green curve but includes pedestal and common-mode corrections. The corrected read-out modes drastically improve the standard deviation to $\sigma_c = 17$ and slightly move the mean to $\mu_c = 0$.

As a guideline, the pedestal corrections should be always used to account for the mean offset. The common-mode calibration, however, should be tested before applying. The algorithm that determines common-modes needs to find a baseline and therefore needs a pixel with no signal in each row and column [158]. In single-particle imaging, the detector is illuminated in (almost) every pixel. In this case, the common-mode correction algorithm may treat real signal as noise and fail to find a common baseline.

In the present thesis, pedestal and common-mode correction has always been applied on the front detectors, as these pixel hold, mostly, signal from single photons. The rear pnCCD uses the pedestal correction but corrects common-modes only above a certain, conservative threshold. See Figure 4.3 for the visible effect on front detector (large, top/bottom arrays) and rear detector (small, centered array).

4.2.1. Combining multiple pnCCD detectors

In order to maximize resolution, it is most useful to combine multiple pnCCD detector image from a single-shot into one larger image. While this is a simple task in itself, it becomes more complex when the combined images need to undergo a phase-retrieval process that use fast Fourier transformations (FFTs). In fact, it has not yet been shown in single-particle imaging that it is possible to retrieve a real space image from multiple detectors in different planes. The reason for this is that, so far, there was little incen-

4. Methods

tive for merging multiple detectors. Until recently, typical samples were on the order of several hundred nanometers in diameter such that little signal could be detected at large scattering angles. With the intensities provided by LCLS and the single-particle imaging capabilities of the LAMP end-station, objects that are smaller than a hundred nanometer in diameter can be studied. Besides the ability to cover larger scattering angles, multiple detectors can be operated in different gains and still be combined efficiently. For the pnCCD, this allows not only an increase in dynamic range but improves the signal-to-noise.

Let us now describe the process of combining multiple detector images from a single-shot, while simultaneously preparing them for the inverse problem of phase-retrieval. The discussion now follows the code shown in appendix 7.2. The input for the following procedure are two pnCCD images. The images should be pedestal corrected and, if applicable, common-mode corrected. Analysis of the electronic noise determines a cutoff or offset between signal-to-noise for each image (see the left panel of Figure 2.14 and 4.2). At this step it is also convenient to account for different detector gain settings, $\text{gain}_{\text{front},\text{rear}}$, using Table 3.2 and detector distances from the interaction region, $\text{distance}_{\text{front},\text{rear}}$, to equalize the measured intensities. The following equation corrects the signal from the rear pnCCD to the front pnCCD plane

$$I(\text{pixel}_X, \text{pixel}_Y)_{\text{normalized}} = I(\text{pixel}_X, \text{pixel}_Y) \cdot \frac{\text{gain}_{\text{front}}}{\text{gain}_{\text{rear}}} \cdot \frac{\text{distance}_{\text{rear}}^2}{\text{distance}_{\text{front}}^2}, \quad (4.1)$$

pixel_X and pixel_Y being the length of the pixel array from the beam along the X- and Y-axis, respectively. The pnCCD front top and bottom module are placed in an enlarged array to reflect the real geometry in the plane of the front pnCCD. We can now transform the rear pnCCD data to this pixel-constructed geometry. Let us use the earlier introduced scattering angle, Θ , in X- and Y-axis separately

$$\Theta_{X,Y} = \arctan \left(\frac{\text{pixel}_{X,Y} \cdot a}{\text{distance}_{\text{rear}}} \right), \quad (4.2)$$

where a is the pixel size along one dimension. We can further generalize the matter and attribute a scattering vector \vec{Q} to each pixel, with the entries in X- and Y-axis separately again

$$Q_{X,Y} = 4\pi \frac{\sin \left(\frac{\Theta_{X,Y}}{2} \right)}{\lambda}, \quad (4.3)$$

4.2. pnCCD photon detectors

with λ being the wavelength of the scattered photons. We can now add the signal from the rear pnCCD to the enlarged array, while using the generalized coordinates \vec{Q} . In this generalized downsampling process, the arithmetic mean of the downsampled pixel is used, which is why a normalization factor needs to be carried. The downsampling into the enlarged array also preserves the pixel size of the front pnCCD (enlarged) array and allows Fast Fourier Transformation (FFT) algorithms to use the array. The usage of FFT algorithms is of great interest to reduce computing times in iterative phase-retrieval algorithms.

Figure 4.3a shows a diffraction pattern from a spherical xenon cluster of ~ 50 nm in radius. The front pnCCD detector was set to slightly overlap with the rear pnCCD detector along the Y-axis but the front detector was set ~ 365 mm closer to the interaction region along the Z-axis. All four of LAMP's pnCCD modules have been combined in one image, and since the rear pnCCD is farther away from the interaction region it appears smaller on the combined image. The red circles are a help for the eye to align the modules and show how the diffraction pattern overlaps. In this case, the front pnCCD was operated in highest gain $\frac{1}{1}$ and the rear pnCCD was operated in lowest gain $\frac{1}{256}$.

The radial intensity profile yields valuable information about the geometric alignment and intensity normalization. Figure 4.4 shows the radial intensity profile of the spherically symmetric diffraction image over 5 orders of magnitude above the noise level. The red curve illustrates the expected scattering intensity of a spherical object using Equation (2.36) and (2.39). An automated fitting routine determined the radius r of the cluster, here, $r = 49$ nm, and the incident beam intensity I_0 , which was determined based on zero-order scattering. The curve showcases the validity of the detected signal up to the edges of the front pnCCD, where little signal is present. There are also some discrepancies from the red curve on the transition from the rear to front pnCCD, which are due to the shadow projected from the front onto the rear pnCCD and the resulting lack of signal.

4.2.2. Impact of the X-ray pump–X-ray probe on diffraction pattern

In a coherent diffractive imaging X-ray pump–X-ray probe experiment, both pulses contribute to the scattering image. The pump-pulse will project an image of the solid and intact cluster, while the probe-pulse will propagate an image of the expanding, damaged cluster. In the present experiment, the pump-pulse was set at $\sim 10\%$ of the overall pulse energy, while the probe-pulse was set to $\sim 90\%$ of the overall pulse energy. In order to simulate the effects of the pump-pulse to the diffraction image, a 1D simulation is con-

4. Methods

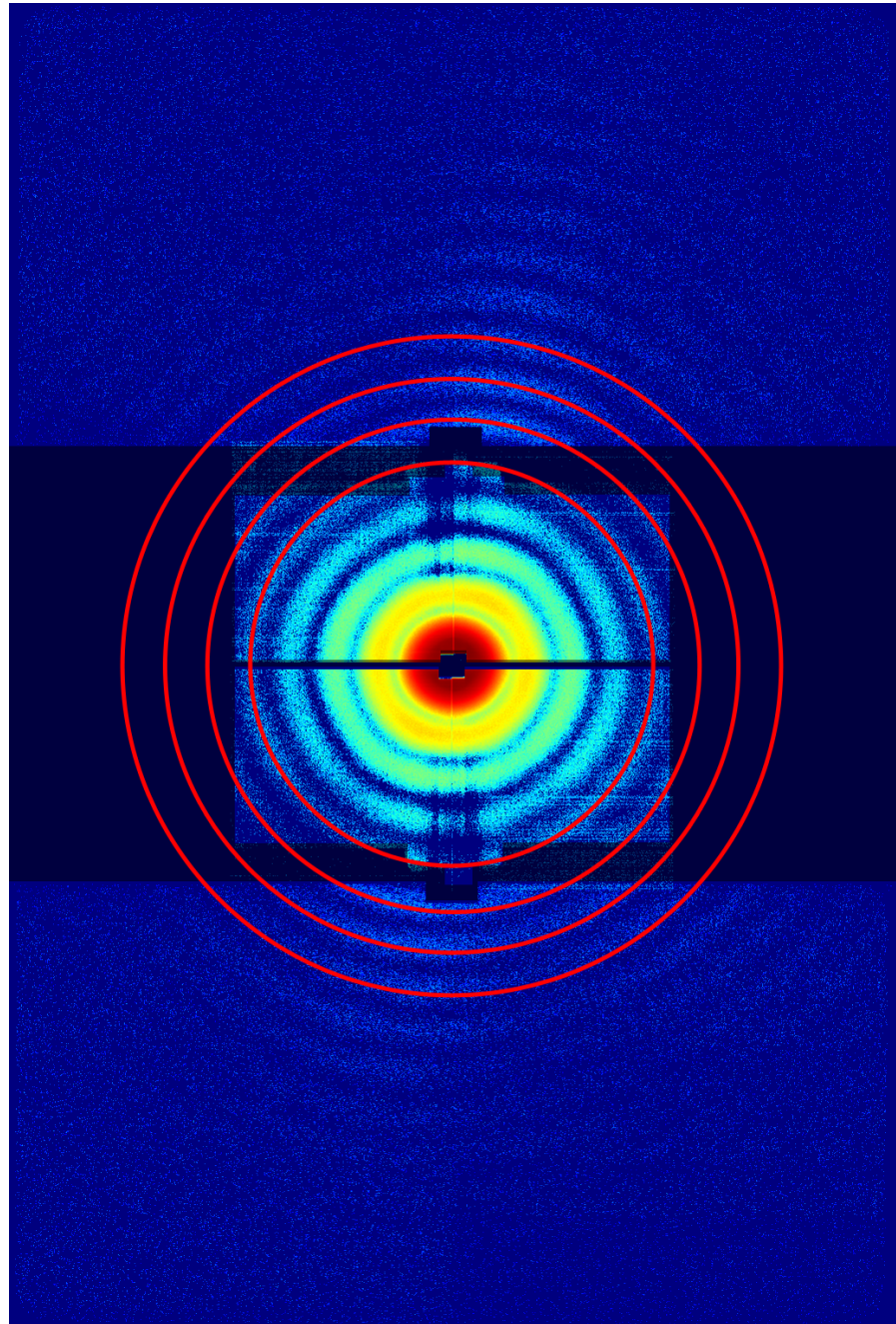


Figure 4.3.: A combined pnCCD image using the full image of the front pnCCD and a down-sampled image of the rear pnCCD. The red circles in the image are drawn to visualize the alignment of the detectors. As described in the text, the intensities in the image are normalized and corrected for different electronic gains and distance to specific detectors. The shaded areas are not covered by the pnCCDs and are therefore masked out.

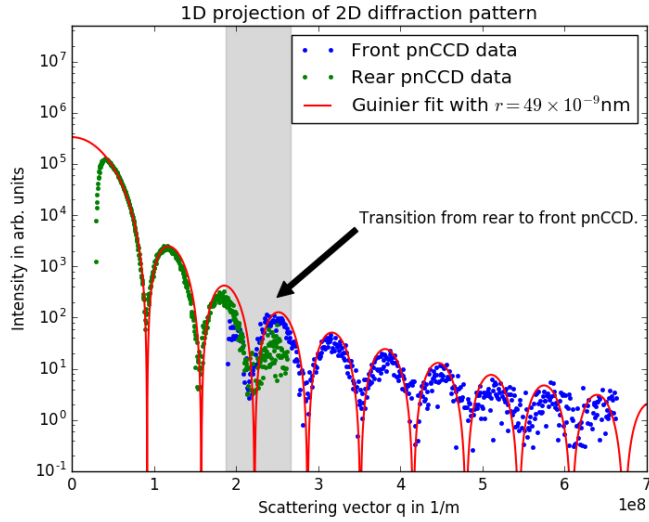


Figure 4.4.: Spherical projection of 2D diffraction image onto 1D. The data points are from the rear pnCCD (green points) and the front pnCCD (blue points) have been combined. The gray shaded area shows the transition area from rear to front detector. The red curve is a simulated scattering curve from an ideal sphere (see Equation (2.39)). The amplitude of the red curve has been fitted to the data points and it agrees well with the data.

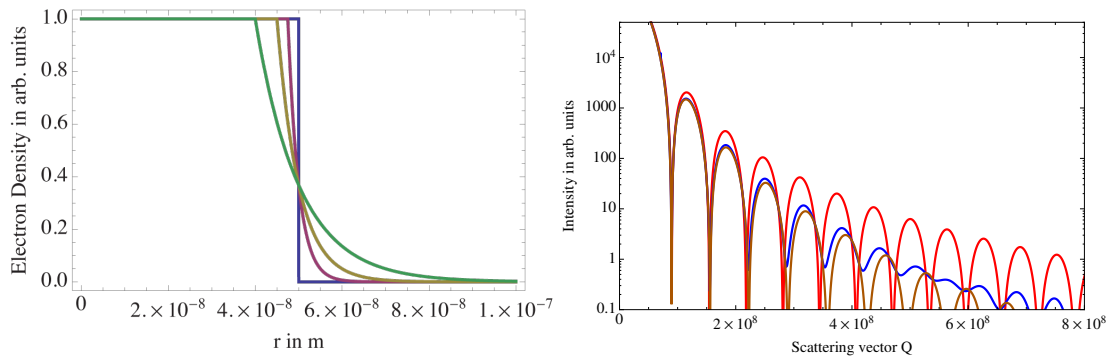


Figure 4.5.: Left: electron density of an expanding spherically symmetric nanoplasma. Right: red line, scattering of an intact sphere. Brown, scattering of an expanding sphere with $k = 5 \text{ nm}$. Blue, combined scattering of an intact and expanding sphere that has been pumped with 10 % and probed with 90 % of the overall pulse energy. See more information in text.

4. Methods

ducted using electron densities of spheres, $\rho(R)$. Although rare-gas clusters exhibit an icosahedral structure, at our present resolution the cluster can be well-simulated using spheres. The spheres are allowed to expand according to the model

$$\rho(R, k) = \begin{cases} 1 & \text{for } r - k \geq R \geq 0, \\ e^{\frac{(r-k)-R}{k}} & \text{for } r > R - k, \end{cases} \quad (4.4)$$

where r is the cluster radius, R is the distance from the center of the cluster, and k an expansion coefficient such that

$$\int_0^\infty \rho(R, k) dR = r, \quad \text{if } 0 < k < r \quad (4.5)$$

The electron density can then be Fourier transformed into reciprocal space using the transformation in 1D due to the symmetry. With the spatial frequencies, Q , we may note [94]

$$I(Q) = I_0 F^2(Q) = I_0 \left(\int_0^\infty \rho(R, k) \frac{\sin(QR)}{QR} 4\pi R^2 dR \right)^2, \quad (4.6)$$

where an incident beam has the intensity I_0 . The electron densities for $r = 50$ nm and $k = (0, 2.5, 5, \text{ and } 10)$ nm are shown in the left panel of Figure 4.5. The right panel of Figure 4.5 showcases several cases of expanding spheres in reciprocal space. The red line is the scattering of a solid sphere, F_{intact}^2 . The brown curve is the scattering of an expanding sphere, $F_{\text{expanding}}^2$, with $r = 50$ nm and $k = 5$ nm. Lastly, the blue curve corresponds to the case, where $I_0 F^2 \rightarrow 10\% \cdot I_0 F_{\text{intact}}^2 + 90\% \cdot I_0 F_{\text{expanding}}^2$. Here the pump-pulse affects the diffraction pattern at high Q -values and decreases the fringe contrast. However, the added signal from the pump-pulse remains within the noise level of $I(Q) < 1$ ADU. For this assessment, the simulated incident beam intensities, I_0 , and cluster radius, r , have been fitted to match the experimental data of Figure 4.4.

4.3. Phase retrieval from a single diffraction pattern

As alluded to in Section 2.3.2, coherent diffractive imaging measures the continuous intensity distribution of an object in reciprocal space and the phase information, i.e., complex fields are lost. Iterative algorithms can retrieve this lost information because there are only limited sets of phases that uniquely reproduce the diffraction image [159, 160]. To fully recover the original function, i.e., real and complex values of the imaged object, the diffraction image must be oversampled [161]. Here, the *Nyquist-Shannon*

4.3. Phase retrieval from a single diffraction pattern

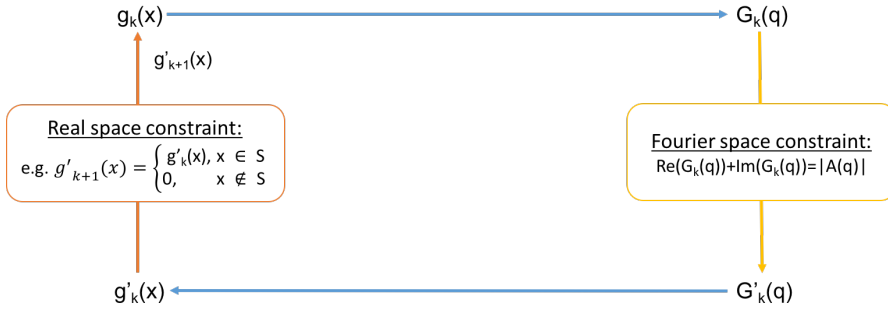


Figure 4.6.: Principle of a phase retrieval algorithm. The real space object $g_k(x)$ is Fourier transformed to $G_k(q)$. The function $G_k(q)$ is altered to fit the constraints set in Fourier space and becomes $G'_k(q)$. $G'_k(q)$ is inverse Fourier transformed to $g'_k(x)$. After fulfilling the real space constraints the iterative starts again using $g'_{k+1}(x)$. After [163].

sampling theorem says that a Fourier transformed object, $A(\vec{Q})$, of size X can be fully recovered if its sampling rate is at the Nyquist rate of $\frac{1}{2X}$. However, we measure the intensity distribution, $I(\vec{Q})$, which already has a period of $\frac{1}{2X}$. In this case, the Nyquist rate – with an *oversampling* of two – can be translated into a minimum pixel-size in real-space that samples $I(\vec{Q})$ using the following relation between a discrete Fourier transformation and pixel length along one dimension, Δ_r . We note [162]

$$\Delta_r \leq \frac{\lambda L}{4X}, \quad (4.7)$$

with the wavelength λ , the length from the interaction region to the detector L , and the object length along one dimension X . This means that larger objects require a more frequent sampling of the scattered intensity distribution. If a large, micrometer-sized object is imaged under typical experimental parameters, where $\lambda = 1.5 \text{ nm}$, $L = 0.371 \text{ m}$, and $X = 100 \text{ nm}$, the detector pixel-size must be $\Delta_r \leq 1.39 \text{ mm}$ along each pixel dimension to fully recover the particle's projected electron density. In the present experiment, the pnCCD pixel-area of $75 \mu\text{m} \times 75 \mu\text{m}$ samples also the largest measured objects sufficiently.

4.3.1. Principle of phase retrieval

To recover the phase from an oversampled diffraction pattern and thus reconstruct an image of the object, iterative algorithms have been developed [163]. Figure 4.6 illustrates such an iterative algorithm, where the image of an object $g_k(x)$ is Fourier transformed to

4. Methods

reciprocal space $G_k(q)$ and then back again resulting in $g_{k+1}(x)$, while sufficing certain constraints.

The constraints are rather strictly defined in the reciprocal space as they have to reproduce the actual measurement $I = A \cdot A^*$, which is sometimes called the modulo constraint. The criteria that need to be met in real space can be chosen more freely. Generally, the recovered object should be physical, i.e., should be of a certain (known) size. One can introduce a support structure S that meets the physical constraints and can therefore be used to, for example, zero outlying values. Throughout the iterations, the functions $g_k(x)$ evolve and eventually converge into a solution. If one uses the above criterion, one can show that the error between the reconstructions and the actual measurement continuously reduces, which is why it is commonly referred to as error-reduction algorithm [164].

4.3.2. 2D reconstructions and image resolution

Hawk program for 2D image phase retrieval

For all image reconstructions in 2D, the Hawk software package [165] has been used. Hawk is available under the GNU General Public License³ and can be downloaded with installation instructions from <https://github.com/FXIhub/hawk>. In previous efforts to retrieve a real-space image from FEL based coherent diffractive imaging, Hawk has been used successfully in several reconstructions ranging from viruses [10, 12] to other few-hundred-nanometer-sized objects [166], but has not yet been used to recover the real space image from rare-gas cluster. The usage of the program is straight-forward in three steps. First, the diffraction images are transformed into the “.cxi” format, which uses HDF5 as base and adopts a variety of other rules to have a uniform format for SPI data-files [167]. Second, diffraction images are prepared in *Hawk’s editor*, where particular effort has to be made to create a pixel mask. The mask prevents shadowed or otherwise faulty pixels from introducing unphysical signals into the reconstruction algorithm. The software suite automatically interpolates between masked pixel regimes, which is acceptable over the length of a few pixels in one direction. Third, *Hawk’s phaser* can be used to iteratively retrieve the phase from the “.cxi” intensity file. Typical parameters for the program can be found in Table 4.1, which can be tedious to find. Therefore, it is worth emphasizing that particularly the *RAAR algorithm* [168] in combination with initially strong *blurs*, the extension of the *phasing beta range*, and a proper determination of the *object area*

³Hawk copyright: <https://github.com/FXIhub/hawk/blob/master/Copyright>

4.3. Phase retrieval from a single diffraction pattern

Parameter	Setting
Starting Guess	random phases
Autocorrelation Selection	threshold
Autocorrelaton Threshold	0.04
Phasing method beta	0.9
Beta range	0 - ∞
Enforce positivity	false
Enforce real	false
Perturb weak reflections	false
Phasing algorithm	raar
Blur	12 - 0.7
Blur range	0 - 12000
Center image	false
Object area	0.0022 - 0.0019
Object area range	0-8000
Support update algorithm	area

Table 4.1.: Typical parameters used in the Hawk software package. The object area depends strongly on the actual particle size and thus varies.

resulted in useful reconstructions using Hawk. Note, that the object area size differs from particle to particle and is a sensitive parameter. After 10^5 to $1.5 \cdot 10^5$ iterations, the real space object typically converges.

Resolution enhancement through combination of rear and front pnCCD

While there is no consensus on how to define resolution in a coherent diffractive imaging pattern and the resulting reconstruction, there are various good estimates. A simple and conservative method to define resolution in a diffraction pattern is Abbe's criterion, which comes from microscopy and calculates the minimal resolvable feature size in a diffraction pattern. The fundamental limit that the minimal resolvable feature size is dependent on the wavelength has also given us the inspiration to build short-wavelength machines such as the free electron laser and new synchrotron light sources.

First, we must verify that we are in the far field by fulfilling the following requirement [162]

$$\frac{X^2}{\lambda L} \ll 1 \quad (4.8)$$

with the wavelength of the X-rays λ , the distance to the detector L and the object size X . In this work, the criterion is met.

4. Methods

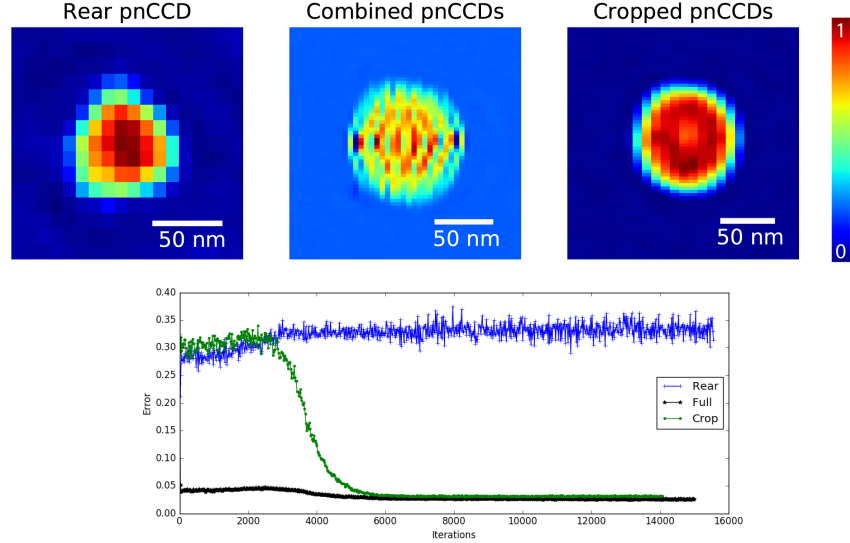


Figure 4.7.: Illustration of resolution enhancement due to detector combination. The diffraction pattern in Figure 4.3 of a Xe-cluster has been reconstructed to illustrate several cases. Top left: Rear pnCCD data only reconstruction yields a non-spherical object; error criterion shows no convergence (see graph). Top middle: Front & rear pnCCD data results in a spherical object but missing areas next to the rear pnCCD disturb the reconstruction process, such that the electron density becomes unphysical. Top right: A cropped diffraction image without the missing areas next to rear pnCCD enables a physical reconstruction.

4.3. Phase retrieval from a single diffraction pattern

In the far field, Abbe's criterion can be written down as

$$d_r = \frac{\lambda}{2n \sin(\frac{\Theta}{2})}, \quad (4.9)$$

with the minimal resolvable feature size d_r , the refractive index n and the half scattering angle $\frac{\Theta}{2}$. The scattering angle is restricted by either the active detector area, which goes back to the typical understanding of a numerical aperture, or the signal intensity up to certain angles. The latter is in interplay with the photon wavelength and object scattering cross-sections.

In the far field, we can use the following relation to determine the actual size of a pixel, Δ_s , in a recovered real space image of an object. We note [162]

$$\Delta_s = \frac{\lambda L}{N \Delta_d}, \quad (4.10)$$

with L being the length from the interaction region to the detector, Δ_d being the linear detector pixel size, and N being the side length of the discrete detector array.

Figure 4.7 top shows several reconstructions of a xenon cluster at $\lambda = 1$ nm using different portions of the diffraction pattern in Figure 4.3. If just the rear pnCCD is used for reconstructions, a maximum scattering angle of $\Theta \approx 4.2^\circ$ is recorded, which results in a minimal resolvable feature size of $d_r \approx 14$ nm. However, in the present data a shadow is cast on the CCD reducing the maximum scattering angle in the image **Rear pnCCD** in the top left panel of Figure 4.7 to $\Theta \approx 3.8^\circ$ and thus the resolution to $d_r \approx 15$ nm. The pixel size is ~ 10 nm \times ~ 12 nm. The image **Combined pnCCDs** of Figure 4.7 uses the whole data including the empty areas next to the rear pnCCD. The image shows an unphysical electron density distribution, which originates from the empty areas next to the rear pnCCD data. In these areas, which have been masked out, the interpolation along the Y-axis and the extrapolation along the X-axis fails. The next image labeled **Cropped pnCCDs** in Figure 4.7 uses data in its full extent along the Y-axis, but is cropped along the X-axis such that the blank areas are excluded. The reconstruction converges into an object that appears physical. The maximum scattering angle here is $\Theta \approx 9.2^\circ$ and the resolution thus $d_r \approx 6$ nm. The pixel-size here is ~ 10 nm \times ~ 3 nm.

This is a factor ~ 5 improvement over common cited studies in single particle imaging [10] and still a factor ~ 3 better than [169], where measured diffraction patterns have

4. Methods

been “computationally purified”. The resolution enhancement due to the combination of detectors can be exploited further using EMC algorithms [170]. EMC algorithms arrange multiple diffraction patterns according to their orientation and are thus able to compute averaged 3D diffraction patterns of a few hundred diffraction images of the same object. When conducting such an experiment, the missing areas next to the rear pnCCDs would fill with data due to random orientations, thus allowing 3D reconstructions of nanoparticles with nanometer resolution⁴.

4.3.3. 1D projections and phase reconstructions

The main goal of reconstructions in this thesis is to recover an image of the object while it undergoes the nanoplasma transition. The effects of the nanoplasma transition on the spherically symmetric cluster can be considered isotropic [15]. It is thus useful to display diffraction patterns and projected electron densities in one dimension to simplify the comparison of the transient states. A 1D representation of the data allows furthermore simplifies the comparison to analytical models. To reduce the 2D diffraction data to 1D the program shown in appendix 7.1 has been employed. It is based on Matlab to efficiently iterate through pixel arrays. The input for this program are pedestal-calibrated diffraction images that have a true image center defined. Key elements of the algorithm are to iterate through every pixel, filtering signal from noise, disregarding missing areas, determining the scattering angle of every pixel, and sum signal over $|\vec{Q}|$, while normalizing the data over the pixel number. To recover the object in real space, an algorithm has been designed to perform phase retrieval on the 1D data. The algorithm follows the fundamental scheme described in sub-Section 4.3.1. Thereby, the real space data of the object is forced to be real and positive, which is also the error criterion in real space. The difference to the measured data yields the error criterion in Fourier space. The algorithm allows monitoring of the Fourier and real space error, the phase and the actual Fourier and real space images. The iterative algorithm is aborted when the error criterion meets a predetermined threshold.

4.4. 2D electron density and diffraction image simulations

The interpretation of the helium cluster doped with xenon data requires a more thorough investigation than is possible with 1D fits. Therefore, two dimensional studies were performed to simulate electron densities of pristine and doped clusters. The electron

⁴Depending on the position of the front pnCCD.

4.4. 2D electron density and diffraction image simulations

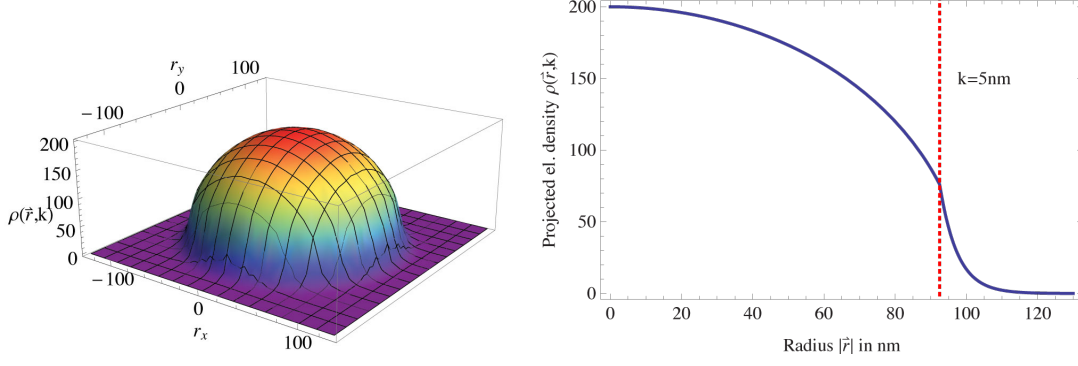


Figure 4.8.: Left: Electron density of a $R \approx 100\text{nm}$ expanding sphere with $k = 5 \text{ nm}$, projected onto a 2D plane. Right: Blue curve, spherical projection of the 2D simulation to 1D. Red dashed line, point of expanding density at $k = 5 \text{ nm}$.

density is then Fourier transformed and squared to yield 2D diffraction images, which can be compared to the experimental data. The 2D simulations can then optionally be reduced to 1D using a spherical integration (see Section 4.3.3) to be easily compared to the experimental data and other analytical models. The clusters are approximated using spheres, which is, at the current resolution, an acceptable estimation of the icosahedral cluster structure. In the simulated, doped cluster, or more general the core-shell system, the shell consists of one large cluster with low electron density, which simulates a helium droplet, and the core comprises smaller dense spheres, which simulate the xenon doping. The spheres can be arranged at different locations within the shell. Furthermore, the simulated spheres can expand to simulate the effect of a nanoplasma expansion. We can express the electron density of a single sphere that has been projected onto a 2D plane using the formalism

$$\rho(\vec{R}, k) = \begin{cases} 2\sqrt{r^2 - |\vec{R}|^2} \cdot \rho_0 & , \text{ for } r - \frac{3k}{2} \geq |\vec{R}| \geq 0, \\ 2\sqrt{r^2 - |\vec{R}|^2} \cdot \rho_0 e^{\frac{(r - \frac{3k}{2}) - |\vec{R}|}{k}} & , \text{ for } r > |\vec{R}| - \frac{3k}{2}, \end{cases} \quad (4.11)$$

with ρ_0 being the density, r being the cluster radius, and k an expansion coefficient such that

$$\int_0^\infty \rho(|\vec{R}|, k) d|\vec{R}| = r, \quad \text{if } 0 < k < r. \quad (4.12)$$

This sphere can be positioned arbitrarily in a 2D array, which simulates the real space image, using $\vec{R} \rightarrow \vec{R} - \vec{R}_0$, with \vec{R}_0 being the center of mass of the sphere. From here,

4. Methods

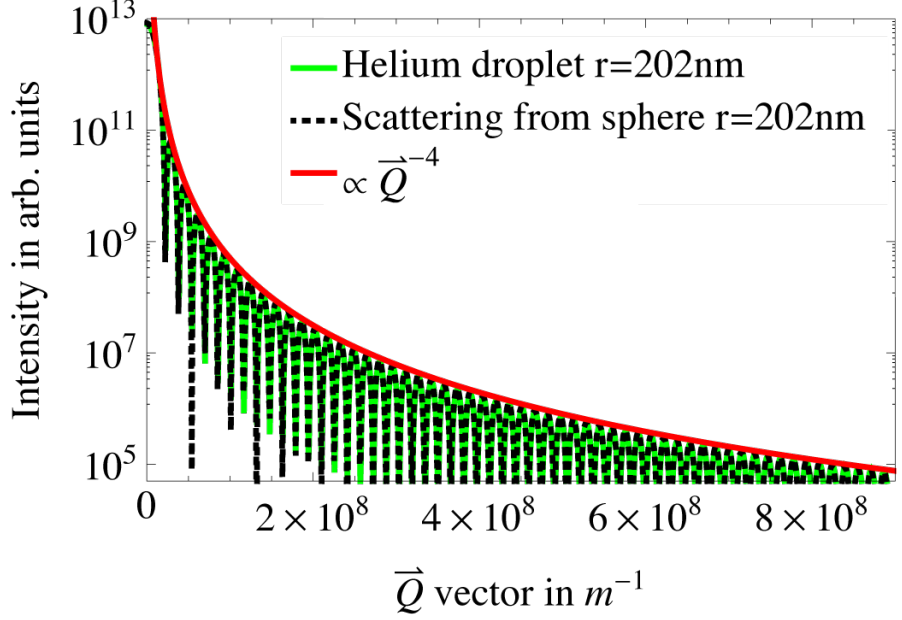


Figure 4.9.: Comparison of analytical scattering from a sphere of radius $R = 202$ nm (black curve), Equation (2.39), and scattering of a sphere of radius $R = 202$ nm from 2D simulations projected onto 1D (green, dashed curve). The envelope of scattering intensity of a sphere (Porod's law) is $\propto q^{-4}$ (red curve). The analytical scattering and developed simulations agree well with each other.

it is simple to construct the desired real space core-shell system. The electron densities of multiple spheres consisting of arbitrary radii and densities can be added together onto the 2D array. In these simulations, the density ρ_0 was set to $\rho_{0,\text{helium}} = 1$ for liquid helium and $\rho_{0,\text{xenon}} = \frac{3.640}{0.1412} \approx 25.8$ for xenon. The numerator of the fraction for $\rho_{0,\text{xenon}}$ is the density of bulk xenon in g/cm³ and the denominator is the density for liquid helium in g/cm³. Using Equation (4.11), a large array of $\sim 1500 \times \sim 1500$ is generated, which is comparable to the combined pnCCD image array size. The array is then Fourier transformed using Matlab's *fft2* and the output is subsequently rearranged using *ifftshift* and squared.

Figure 4.9 shows a comparison of the analytical derived scattering of a sphere (see Equation (2.39)) with a radius of $r = 202\text{nm}$ (black, dashed line) and the scattering of the 2D simulations reduced to 1D (green, solid line). The red curve is the envelope of the functions, called Porod's law that scales with $\propto |\vec{Q}|^{-4}$. The developed simulation agrees well with the analytical scattering, when $k = 0$.

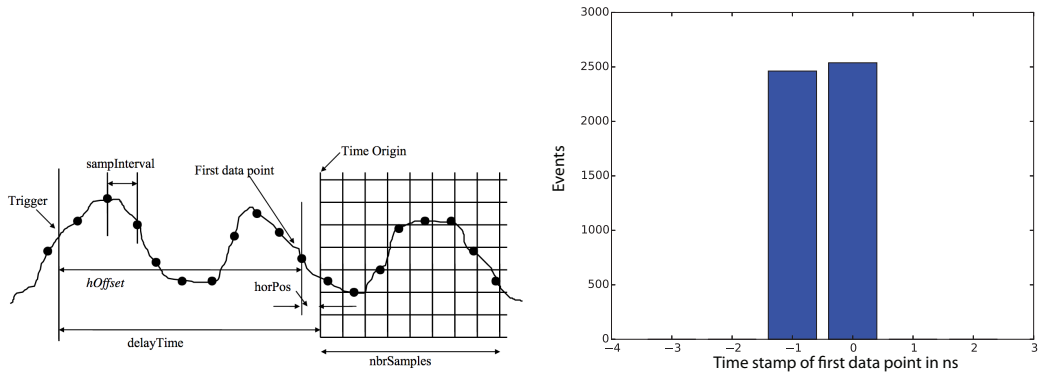


Figure 4.10.: Left image from [171], it shows the schematics of the “rolling” buffer in the Acqiris. An electronic trigger start a read-out process may occur anytime within the buffer. Due to the sampling in finite time-intervals, the First data point can be before the Time Origin. The right image is a histogram of the the time-stamp from the First data point.

4.5. Acqiris data sampling considerations

An Acqiris digitizer (now called: Agilent U1065A) has been used to read out the waveform signal from the time-of-flight spectrometer discussed in Section 3.5. For technical reasons, the Acqiris sampling rate and the Acqiris “clock” are generally not chronologically synchronized with the electronic trigger from LCLS-EVR that starts the readout process. The electronic trigger can occur between the sampling point (1, 2, ..., or 10), as it is illustrated in the left panel of Figure 4.10. These initial 10 channels function as some sort of a “rolling” buffer for the Acqiris. When the Acqiris receives the trigger, it reads out 40 000 samples including the 10 initial sampling points, so, some sampling points may be before the trigger and are thus “unused”. The unused sampling points are removed from the trace by the Acqiris. But to avoid different trace lengths in the data analysis that vary from shot-to-shot, the LCLS DAQ group fills each array with zero entries until the trace is 40 000 points long. This simplifies the data analysis and data handling of the waveform signal. Additionally we should consider the case when the trigger comes in between two sampling points, where the time difference between the *First data point* and the *Time Origin* is within the sampling interval (see Figure 4.10). In this case, the Acqiris uses the first data point as first entry in the read out trace to avoid data loss. This first data point may have a negative time stamp attributed to it as the time origin occurs closer to the second data point. The right panel of Figure 4.10 shows is a histogram of the time stamp from 5000 first data points. The time-stamp

4. Methods

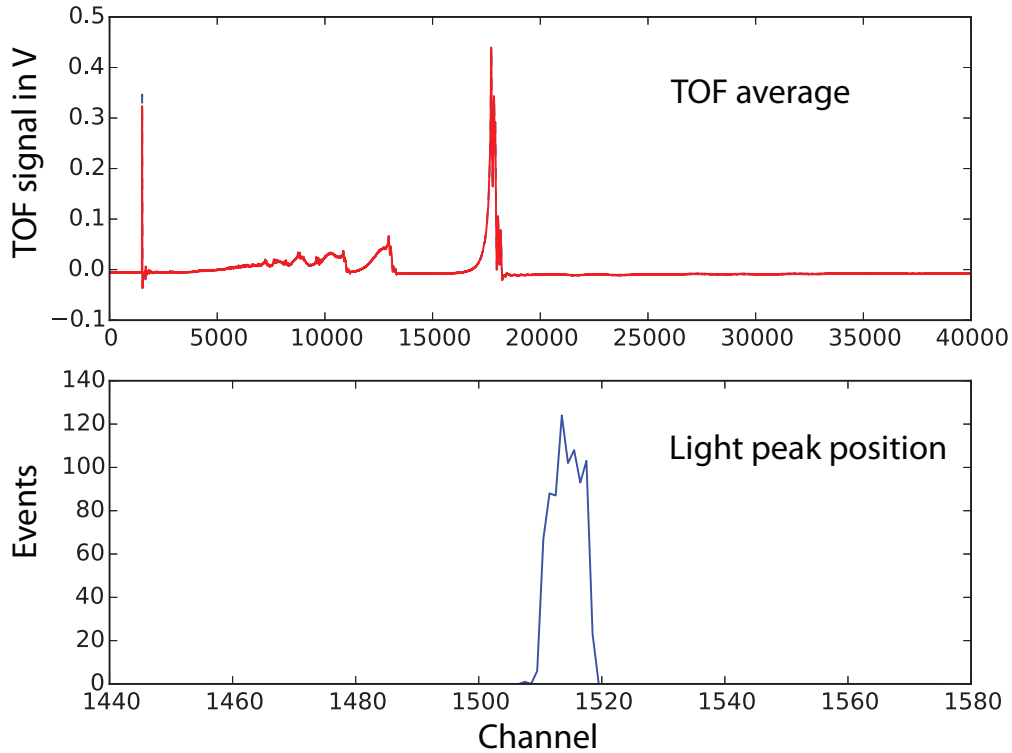


Figure 4.11.: Top plot, average TOF trace of xenon cluster upon irradiation with LCLS. Red curve, corrected run average to account for shifted light peak due to Acqiris sampling. Blue curve, uncorrected average. Bottom image, histogram of light peak channel position ranging between ± 5 of channel 1514.

is evenly distributed, which is what one would expect when the electronic trigger “randomly” occurs in between sampling points.

Due to these considerations, the origin of time in a LCLS experiment is best defined by the light peak in a TOF trace. The time-of-flight spectrometer will detect photons scattered of the sample as the pulse is traversing through the system. This light peak is typically in the beginning of the TOF trace and for well scattering samples, such as xenon clusters, the light peak is a well-defined peak (see top panel of Figure 4.11). When 40 000 channels are being read out, each channel corresponds to one sampling point at a sampling rate of 1 ns. The bottom panel of Figure 4.11 shows an analysis of the light peak position in the TOF trace. The light peak occurs within a ~ 10 ns window and is evenly distributed around channel 1514. We attribute this to the earlier mentioned

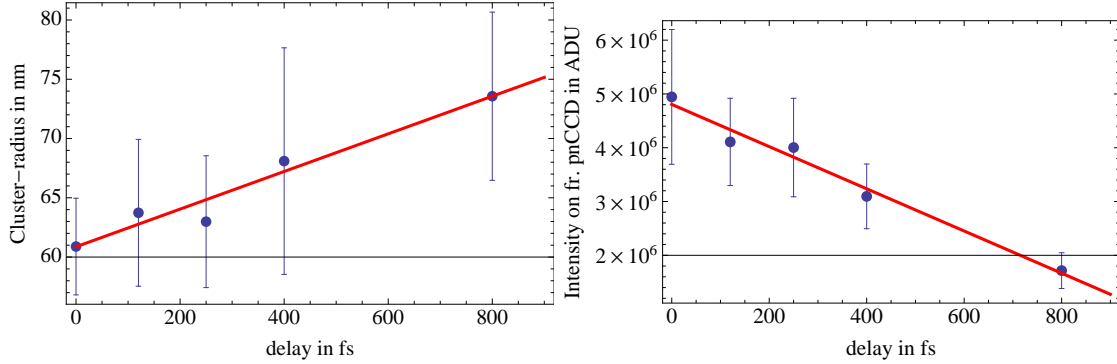


Figure 4.12.: Left: Average Xenon cluster size of intense hits as a function of pump–probe delay Δt . Right: Average intensity on the front pnCCD of intense single-shot hits from single Xe-cluster as a function of the pump–probe delay Δt .

“rolling” buffer. The top panel of Figure 4.11 shows an average of 1000 TOF trace (blue curve) and a TOF trace that has been corrected for the light peak occurring at different position (red curve). The data shows a very good agreement of both curves and indicates that at low time-resolution of a 1 ns sampling, the above considerations may be disregarded. However, for high-resolution TOF spectroscopy the above considerations will become important. The time-of-flight analysis in this thesis accounts for the above considerations and additionally corrects for a common baseline.

4.6. Data filtering

As described in the above sections, LCLS produces large amounts of data. This data has to be filtered to a point, where it can be used for phase retrieval and plotting. The coincident detection of diffraction image and time of flight trace allow great freedom to filter on useful events. For the present work, a useful event is the interaction of X-ray pump–X-ray probe pulse sequence with a single cluster system. On the one hand, clusters produce the most intense signal on pnCCD and TOF detectors when they are in the center of the intensity profile of the LCLS beam [33]. On the other hand, as the time delay, Δt , of the X-ray pump–X-ray probe is increased, the nanoplasma expansion leads to a decrease in signal on the pnCCD (see Figure 4.12). This can be extrapolated to an extreme, where a cluster would produce barely any signal on the front pnCCD. In order to filter on the full spectrum of interesting hits, a series of filters have been applied. Filtering on ion time of flight high-charge states has been successful in the large scale analysis of events that resolve pump–probe dynamics. In the left panel of Figure 4.12,

4. Methods

the xenon pump–probe data has been automatically pre-filtered on xenon ion high-charge states, leaving several thousand events that were then semi-automatically reduced to over 350 single-hit diffraction images. This semi-automatic process determines, whether it was a single hit and the size of a cluster. The size determinations have been performed using the first maxima as described (see Section 2.3.2). The plotted events in Figure 4.12 indicate a linear average-Xe-cluster-radius increase of $\sim 20\%$ over the course of the first 800 fs (see more in Section 5.1). However, to perform phase retrieval and to solve the inverse problem, bright hits containing many photons are required. Therefore, another set of hitfinding has been implemented. This hitfinder determines the scattering intensity of single events automatically and the brightest hits that show signs of X-ray induced dynamics have been selected semi-automatically. These hits undergo a phase retrieval to reveal their electron density. To clarify, single He- and Xe-cluster hits show X-ray induced dynamics, when the 1d reduction of the intensity profile differs from the scattering of an intact sphere, i.e., $\frac{I}{F_{\text{intact}}^2} \ll 1$. The case of X-ray induced dynamics in HeXe-clusters is discussed in more detail in Section 5.5.

5. Results and discussion

This chapter discusses the experimental data and is organized as follows. First, the nanoplasma transition in pristine Xe-clusters is discussed in Section 5.1. Section 5.2 discusses the time dependent response of Xe-atoms to X-ray pump–X-ray probe beams in ion TOF. Ion TOF spectroscopy is continued on superfluid He- and mixed HeXe-clusters in Section 5.3. The arrangement of Xe-atoms in HeXe-clusters is discussed in Section 5.4 using 2D-simulations. Sample damage scenarios of HeXe-clusters are compared to simulations in Section 5.5. Section 5.6 compares structural damage from the nanoplasma expansion for the different samples, He-, Xe-, and HeXe-clusters, to each other.

5.1. Structural damage in Xe-clusters induced by intense X-rays

A large scale analysis of size, scattered intensity and shape is performed on single-shot diffraction patterns of xenon cluster to investigate the nanoplasma transition. The analysis starts by selecting useful hits from an experimental run using the methods described in Section 4.6. A typical run length is 20 min and results in a total of $\sim 36\,000$ images. These events are automatically reduced to ~ 1000 events by filtering on high-charge states of Xe-ions. Then, a semi-automatic routine reduces the data to a subset of 30 to 60 single-shot diffraction patterns per run. This breakdown allows the estimation that (0.08 to 0.16) % of all imaged xenon clusters had good parameters for analysis per run. Multiple runs of data were taken as the pump–probe delay Δt was varied.

In the above mentioned high-throughput size evaluation, Equation (2.39) is used to automatically determine the cluster radii of several hundred Xe-clusters. Figure 5.1 shows a distribution of cluster radii at X-ray pump–X-ray probe delays, $\Delta t = (0 \text{ and } 800) \text{ fs}$. The size distribution of Xe-clusters follows a log-normal distribution [172] and at $\Delta t = 0 \text{ fs}$ the mean cluster radius is 61 nm. When the delay is increased to $\Delta t = 800 \text{ fs}$, the mean cluster radius increases to 74 nm and the distribution becomes more broad. The mean cluster radius increase by $\sim 20\%$ over the time delay of 800 fs is attributed to the

5. Results and discussion

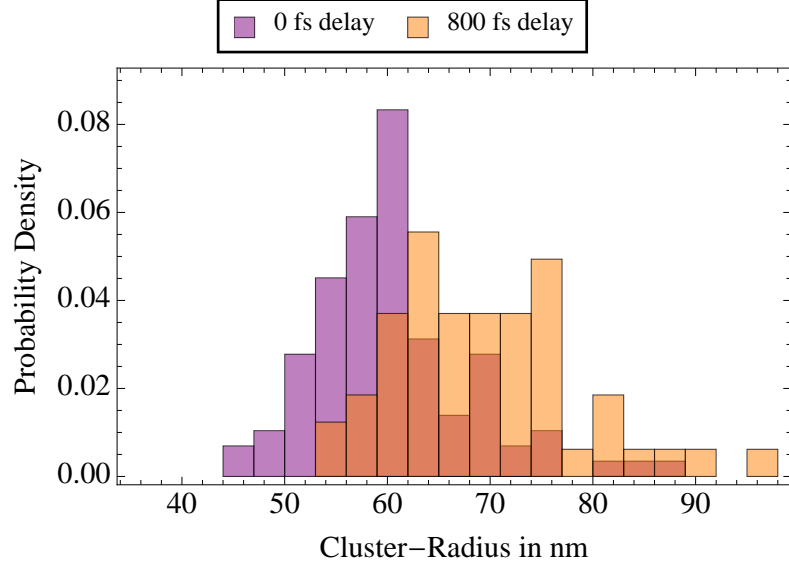


Figure 5.1.: Size evaluation of ~ 30 single Xe-cluster hits per time delay Δt step. At $\Delta t = 0$ fs, the size distribution follows an expected log-normal distribution, while at $\Delta t = 800$ fs the distribution broadens and shifts towards larger radii due to the nanoplasma transition.

nanoplasma expansion, as the cluster source should have a stable size distribution. The Xe-cluster size distribution may become more broad due to a distribution of the pump-pulse power density that varies the expansion speed from shot-to-shot.

Figure 4.12 summarizes the mean cluster radii data over several pump–probe delay steps, $\Delta t = (0, 120, 250, 400, \text{ and } 800)$ fs. This data suggests that the nanoplasma expansion speed, v_{exp} , is constant. With the mean cluster radii at $\Delta t = (0 \text{ and } 800)$ fs, we note $v_{\text{exp}} \approx 15250 \text{ m s}^{-1}$. We may use this expansion speed to estimate the electron temperature of the nanoplasma. Here, it is assumed that electrons thermalize with the nucleus within a few femtoseconds such that the velocity distribution of the hot electron gas in the nanoplasma follows a Maxwell-Boltzmann distribution. If we use v_{exp} as mean velocity of a Maxwell-Boltzmann distribution the electron temperature is $\sim 125 \text{ eV}$, which compares to temperatures that can be found inside the sun. We can also compare the electron temperature to a similar IR pump–X-ray probe nanoplasma study on Xe-clusters [15], where electron temperatures of $\sim 200 \text{ eV}$ have been found. The difference in expansion speed and electron temperature is attributed to the different pump-pulse parameters. Although the IR-pump pulse had power densities of only $\sim 10^{15} \text{ W cm}^{-2}$ compared to the $\sim 10^{17} \text{ W cm}^{-2}$ of the X-ray pump-pulse in this study, the X-ray absorption cross-section

5.1. Structural damage in Xe-clusters induced by intense X-rays

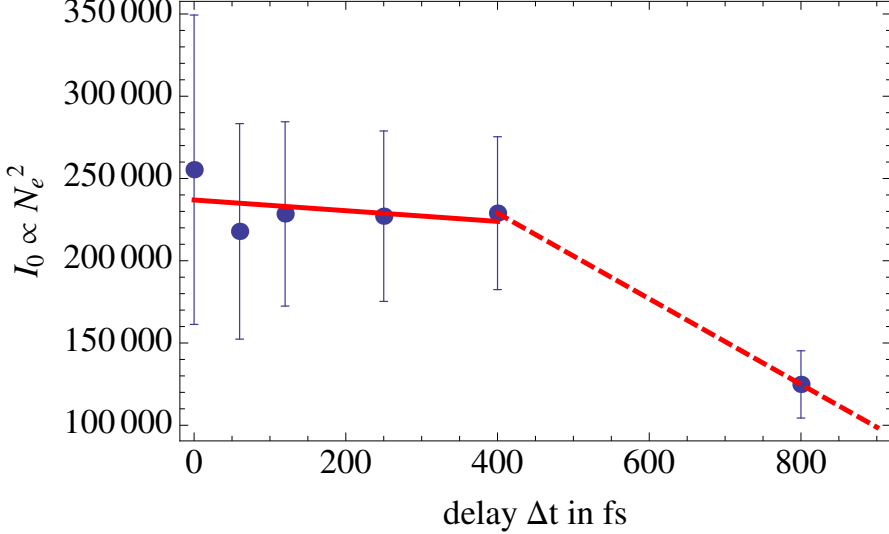


Figure 5.2.: Intensity I_0 in arb. units at $\vec{Q} \rightarrow 0$, which is proportional to the total number of scatterers squared N_e^2 , here electrons. The data show that the expanding cluster Coulomb traps electrons steadily in the initial stages of the nanoplasma expansion but as the trapping potential decreases due to the multi-step ionization a sudden decrease of $\sim 65\%$ electrons is observed.

is much smaller than the IR cross-section. Ultimately, the Xe-clusters absorb more energy from IR pump-pulses than X-ray pump-pulses of similar power density.

The total number of scatterers, i.e., electrons that interact with the LCLS pump-pulse, is deduced from the diffraction patterns via an intensity analysis. As described in the theory Section 2.3.2, when

$$I(\vec{Q} \rightarrow 0) \propto N_e^2, \quad (5.1)$$

where I is the distribution of the scattered intensity as a function of the scattering vector \vec{Q} , we can determine the number of electrons, N_e , that contribute to the scattering process. Figure 5.2 shows the parameter ρ_0^2 , from Equation (2.39), as a function of the time delay Δt (blue dots). As the incident beam intensity, I_0 , remains constant in the X-ray pump–X-ray probe setup $\rho_0^2 \propto N_e^2$. Two linear fits (red lines) have been added to the figure to visualize the effect. The data show that up to a delay of $\Delta t = 400$ fs the amount of electrons N_e in the interaction region rather constant (solid red line). However, at a time delay of $\Delta t = 800$ fs, the number of scattering electrons decreases on average by $\sim 26\%$ (dashed red line). This supports the idea that the Coulomb barrier efficiently traps electrons from the ionization process in the initial stages of the nanoplasma expansion.

5. Results and discussion

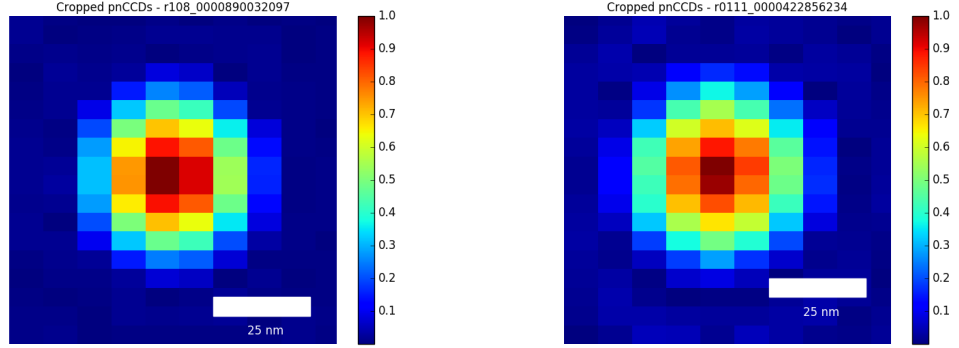


Figure 5.3.: Single-shot 2D reconstructions of diffraction patterns from single Xe-clusters. The left image shows a ~ 25 nm radius Xe-cluster at a pump–probe delay $\Delta t = 0$ fs. The cluster has a spherical or arguably icosahedral electron density distribution that is distinct compared to the background. The right image shows a ~ 25 nm radius Xe-cluster at a time delay $\Delta t = 800$ fs that shows a similar symmetry but due to the loss of scatterers (see fig 5.2), the signal-to-noise ratio decreases and a ringing appears that is likely generated by the support structure in the iterative process.

sion, here, up to 400 fs after the pump-pulse. But, eventually, the electrons overcome the trapping potential and dissipate the interaction region, such that they do not contribute to the diffraction image anymore. The key driver that lowers the trapping potential, thus releasing the electrons, is the expansion of the cluster. The effect of trapped electrons has been simulated in, e.g., [18]. Trapped electrons contribute drastically to the radiation damage process due to secondary collisional ionization.

In a thought-experiment, where SPI is performed using long X-ray pulses of ~ 100 fs, the sample would get ionized and efficiently traps electrons. The trapped electrons can be treated as non-relativistic, thus they do contribute coherently to the scattering pattern. However, their contributions reduce the contrast as their positions are not related to the structure. A similar damage effect is described in [16] and it is shown that computational methods may compensate for such damage.

Figure 5.3 shows 2D reconstructions of single Xe-clusters at $\Delta t = 0$ fs in the left panel and $\Delta t = 800$ fs in the right panel. The clusters appear generally spherical, however, an icosahedral shape is imaginable. Both clusters have a radius of $r \approx 25$ nm. The reconstructions constitute some of the smallest objects recovered with diffraction imaging at the time of

5.1. Structural damage in Xe-clusters induced by intense X-rays

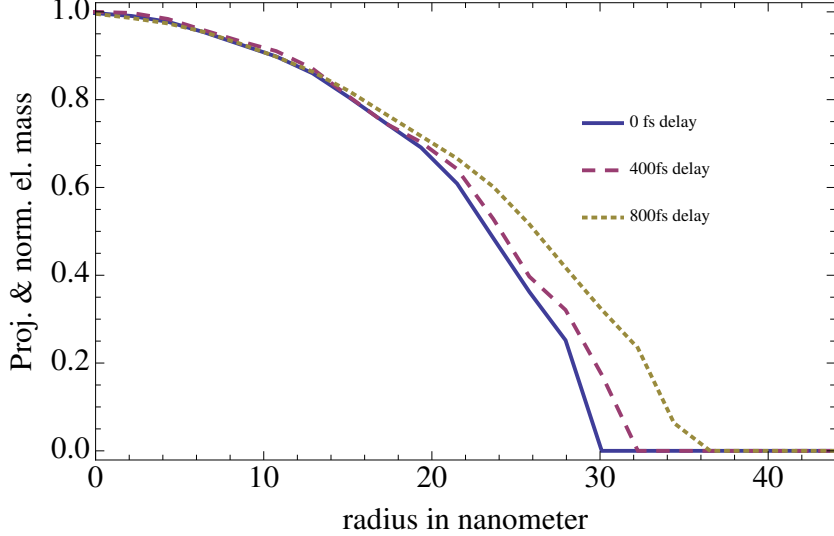


Figure 5.4.: Single shot 1D reconstruction of Xe-cluster at various time delays Δt . The figure shows the projected and normalized el. mass as a function of the radius, i.e., the electron density. These real-space images of a nanoplasma transition show that, at first, outer atomic layers are shed off, here imaged at $\Delta t = 400$ fs. And over time, more inner atomic layers follow, here imaged at $\Delta t = 800$ fs.

writing. The minimal resolvable feature size in these images is ~ 14 nm \times ~ 6 nm along the $X \times Y$ -axis (see Section 4.3.2). The reconstruction at $\Delta t = 800$ fs shows a ringing around the actual cluster, which is likely an artifact of the spherical support structure. This ringing becomes visible due to a lower signal-to-noise ratio, which is due to the described loss of electrons in the interaction region. Due to the resolution limitation, a nanoplasma expansion, i.e., the earlier discussed 20 % increase in Xe-cluster radius, may be difficult to see. Also, 2D reconstructions of nanoparticles of that size are challenging and the number of successful 2D reconstructions is low. We thus analyze the xenon imaging data in 1D in the following paragraphs.

Real-space images of single Xe-clusters have been recovered in 1D in Figure 5.4 (see methods Section 4.3.3). The 1D reconstructions show normalized and projected electron density from single xenon cluster at time delays $\Delta t = (0, 400, \text{ and } 800)$ fs. At $\Delta t = 0$ fs, the electron density follows the density projection of a sphere (compare Figure 4.8). With a delay of $\Delta t = 400$ fs, an expansion of the outer atomic layers of the cluster is observed. At $\Delta t = 800$ fs, outer layers continue to expand and inner atomic layers start

5. Results and discussion

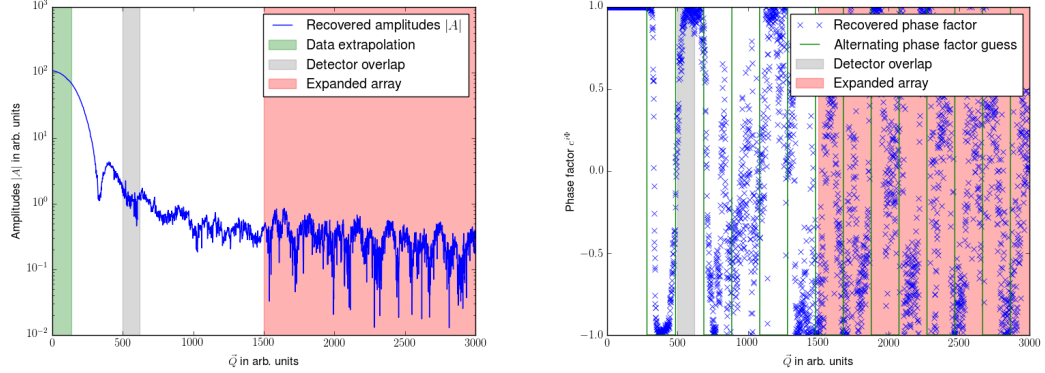


Figure 5.5.: The left panel shows the recovered amplitudes $|A|$ and the right panel shows the phase factor of the 1D phase retrieval. The green and red background indicates the space where initial data points were extrapolated. The gray area discloses the detector overlap. See Section 4.3.3 for more details.

to follow. Over the time delay sequence $\Delta t = (0 \text{ to } 800) \text{ fs}$, the cluster radius expands $\sim 20\%$, or from $r \approx (30 \text{ to } 36) \text{ nm}$. This sequence of events gives insight into the shape of the Xe-cluster as it undergoes the nanoplasma transition and directly confirms theoretical predictions, e.g., [18]. The images clusters have comparable initial sizes as they are selected from the lower end of the cluster size distribution.

For the sake of completeness of these 1D reconstructions, the recovered modulo of the amplitude, $|A|$, and the recovered phase factor are shown in Figure 5.5 for the data at $\Delta t = 800 \text{ fs}$. The amplitudes $|A|$ have been replaced in the space with white background. The data with the green background was interpolated using the anticipated scattering of a sphere. The grayed area indicates the pnCCD detector overlap and the red background data is extrapolated from the scattering of a sphere. The red area therefore increases the resolution. The data points of the k-times iterated Fourier-space function $G'_k(\vec{Q})$ in the white area were replaced with the original data set while $G_k(\vec{Q})$ was allowed to evolve freely in the remaining area. The phase factor retrieval starts with an initial guess of alternating signs per diffraction ring of the sphere and then evolves freely. One can see how the recovered phase factor is alternating as one would expect from the scattering of a sphere.

We may also analyze the Xe-cluster in reciprocal space and analyze the radial projections of the measured diffraction patterns directly. Radial projections of single-shot diffraction

5.1. Structural damage in Xe-clusters induced by intense X-rays

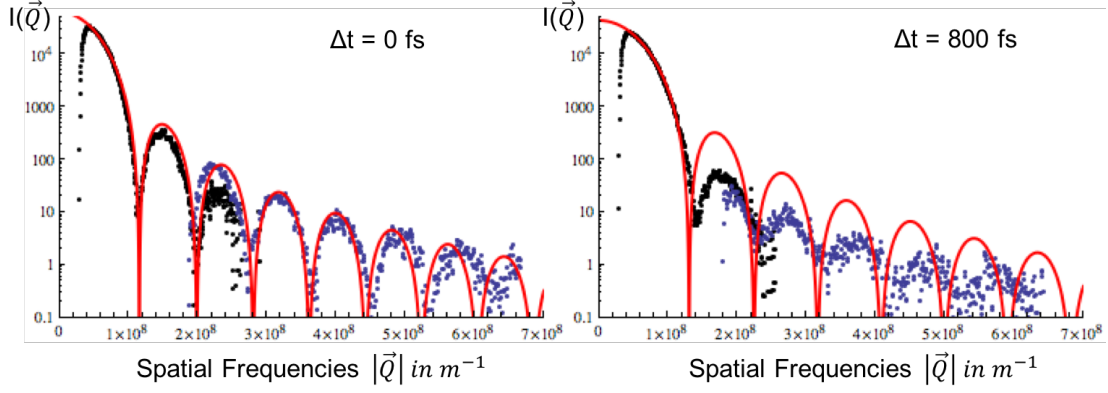


Figure 5.6.: Single shot diffraction pattern at certain pump–probe delays Δt . The red curve simulates the scattering of a sphere, the black data points are from the rear pnCCD detector and the blue data points are from the front pnCCD. The nanoplasma expansion manifests in the scattering intensity I at high spatial-frequencies $|\vec{Q}|$, where I decreases as described in [15].

patterns from single Xe-cluster can be found in Figure 5.6. The figure shows a red line, which is the scattering from a sphere as per Equation (2.36) and (2.39) fitted onto the low- $|\vec{Q}|$ signal of the zeroth diffraction scattering order using the radius and the incident beam intensity variable. The black data points are projected from the rear pnCCD and the blue data points are projected from the front pnCCD using the projection method described in 4.2.1. At $\Delta t = 0$ fs, the scattering of the Xe-cluster can be well approximated with the scattering of a sphere. Hence, the fit (red line) agrees well with the data points up to scattering angles of $\Theta \approx 9^\circ$ or $|\vec{Q}| \approx 6.8 \cdot 10^8 \text{ m}^{-1}$. However, it should be noted that this comparison becomes less good at very large scattering angles due to the flat detector [110] and deviations in the diffraction pattern from a perfect sphere. As the time delay Δt increases, the large- $|\vec{Q}|$ scattering signal decreases and the scattering of a plain sphere does not fit the scattering well anymore. A similar effect is also observed in the previously mentioned IR pump–X-ray probe study [15]. Due to the nanoplasma transition, the Xe-cluster is expanding with the outer layers expanding faster than the core. A mathematical description of this damage model, namely an expanding sphere, has been introduced in Section 4.4. It generally fits the data well, as it is shown in great detail in [15, 173]. Note that the X-ray pump–X-ray probe considerations from Section 4.2.2 would minimize the effect of a decreased scattering at large scattering angles.

5. Results and discussion

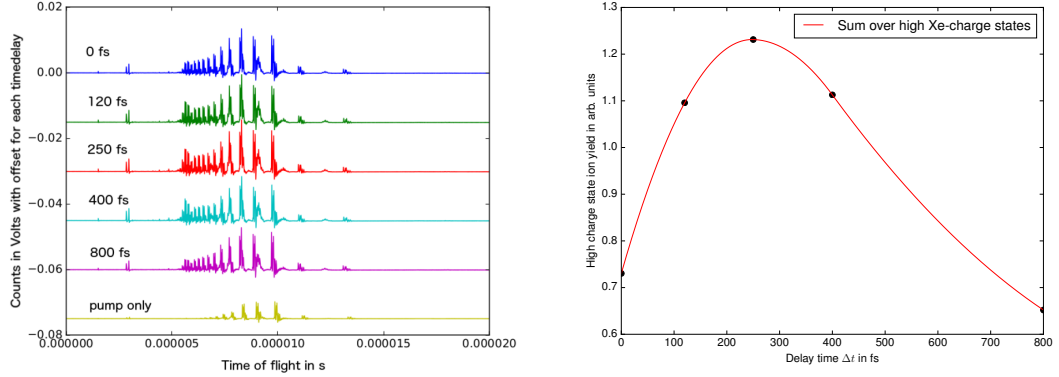


Figure 5.7.: Atomic xenon ion time-of-flight data shows resonant type behavior. As the X-ray pump-pulse traverses through the xenon ions, the 3d-subshell becomes highly ionized and thus the atom becomes increasingly transparent for the probe-pulse ($\Delta t \approx 0 - 120$ fs). The electron-holes have a longer lifetime due to the highly ionized subshell. After the Auger decay populates the 3d-subshell, the atom becomes less transparent and the X-ray probe-pulse efficiently ionizes the atoms ($\Delta t \approx 250$ fs). Eventually, relaxation processes dissipate energy leading to fewer high-charge states.

5.2. Time-dependent response of Xe-atoms due to an X-ray pump–probe beam

Ion time-of-flight traces of atomic xenon at different time delays $\Delta t = (0, 120, 250, 400,$ and $800)$ fs and X-ray pump-pulse only data is shown in Figure 5.7. The time-of-flight data show a resonance behavior as the atomic xenon high-charge states peak at $\Delta t = 250$ fs. The xenon high-charge states start low at $\Delta t = 0$ fs and then peak due to intensity-induced X-ray transparency [14, 174]. In the present study, the xenon 3d-subshell is efficiently ionized by the X-ray pump-pulse. These electron-holes are typically repopulated on the few femtosecond timescale due to the Auger decay, however, the increasingly ionized atom has longer electron-hole lifetimes and the Xe-atoms become increasingly transparent as the X-ray pulse propagates. It has been measured that Ne^{8+} has core-hole lifetimes of 230 fs. But why does the charge state distribution then not level out for later delays $\Delta t > 250$ fs? When the strongly pumped atom does not absorb energy near saturation, relaxation processes catch up and effectively dissipate energy, thus reducing the average ionization level.

5.3. Time-resolved response of highly ionized He- and HeXe-clusters

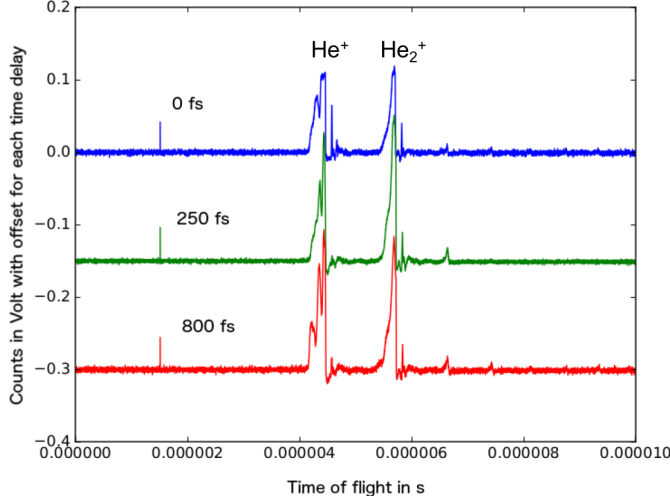


Figure 5.8.: Ion time-of-flight traces of He-cluster with a radius of $r_{\text{He}} \approx 810$ nm. Although minor changes in the charge fragmentation are observed, we shall note that there are no He^{2+} ions in this data. The absorption cross-section of helium are too low to lead to doubly-charged states [96].

5.3. Time-resolved response of highly ionized He-clusters and xenon doped He-clusters

The response of clusters in highly intense X-ray radiation is more complex than the atomic signal. Size-dependent [174, 175] and recombination effects in the nanoplasma [176] alter the sample's ionization pathways. Figure 5.8 shows ion time-of-flight data of pristine He-cluster charge fragments at pump–probe delays $\Delta t = (0, 250, \text{ and } 800)$ fs. The pristine He-droplets have a radius of $r_{\text{He}} \approx 810$ nm or a number of He-atoms of $N_{\text{He}} \approx 5 \cdot 10^{10}$ using the relation [65]

$$r_{\text{He}} = 0.22(N_{\text{He}})^{\frac{1}{3}} \text{ [nm].} \quad (5.2)$$

The data show an overall similar behavior regardless of the delay Δt , although minor changes in the charge fragmentation distribution can be seen. More importantly for referencing purposes, the traces indicate no contribution of doubly-charged helium atoms. The lack of double-charged helium can be explained by the comparably low absorption cross-sections of helium (see Table 2.3) [96].

Xenon doped helium cluster time-of-flight traces are shown in Figure 5.9. Here the He-

5. Results and discussion

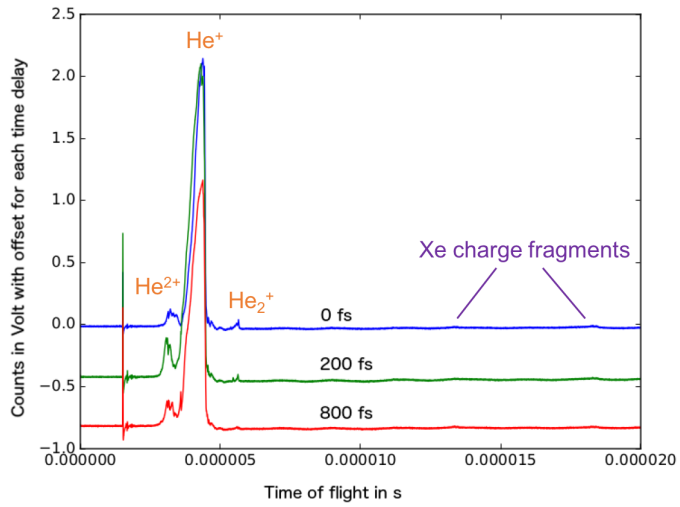


Figure 5.9.: Ion time-of-flight spectra of He-cluster with $r_{\text{He}} \approx 600$ nm radius and Xe-doping levels of $\sim 0.6\%$. The Xe-atoms absorb X-rays efficiently and transfer the absorbed energy to the He-atoms. The Xe-ions recombine and only a few xenon charge fragments are observed. Due to the energy transfer, doubly-charged He-ions are detected and the *kinetic energy release* is increased as well. As the delay time, $\Delta t = (0, 200, \text{ and } 800)$ fs, is varied sequentially, the system undergoes a resonant type behavior that is attributed to the ionization dynamics of Xe-atoms.

5.3. Time-resolved response of highly ionized He- and HeXe-clusters

droplets have a radius of $r_{\text{He}} \approx 600 \text{ nm}$ or a number of He-atoms $N_{\text{He}} \approx 2 \cdot 10^{10}$ with a $\sim 0.6\%$ doping level of xenon. For the sake of completeness, the helium depletion at this doping level is $\sim 62\%$ (see Section 2.2.2). Most notable is the presence of He^{2+} ions and a strongly increased signal from He^+ ions. But, few xenon charge fragments are observed. This is counter-intuitive as the absorption cross-section from xenon is vastly higher than from helium (see Table 2.3). We can therefore hypothesize two points. One, there must be an efficient, ultrafast energy transfer process from the Xe-particles to the He-droplet; two, that the helium atoms function as electron reservoir as the initially photoionized xenon atoms must recombine with trapped electrons to be neutrally charged and thus not detected by the ion TOF. As the time delay Δt is varied, we observe that the He-ion signal shows a resonant behavior. At $\Delta t = 200 \text{ fs}$, the signal from He^{2+} and He^+ peaks. However, the helium signal is less intense at the delay times $\Delta t = 0$ and 800 fs . We can make use of the earlier discussion around the data shown in Figure 5.8 and 5.7 and conclude that this behavior does not originate from the absorption and ionization dynamics of the He-droplet but rather from the Xe-atoms with which the He-droplet is doped. In a theoretic study of HeXe-clusters using optical laser pulses a similar resonant behavior is found [124].

Figure 5.10 shows ion time-of-flight data of with $r_{\text{He}} \approx 775 \text{ nm}$ He-droplets and a $\sim 0.06\%$ doping at pump–probe delays $\Delta t = (0 \text{ and } 800) \text{ fs}$. Here, the helium depletion is measured to be $\sim 13\%$. We note, again, the presence of He^{2+} ions and more signal from He^+ ions. However, compared to the higher doped data these peaks are less intense. Qualitatively this can be explained with the less strong xenon doping. The X-ray absorption from the xenon atoms and subsequent energy transfer to the helium atoms dominate the helium ion characteristics, although the He-droplet is larger in this case. So, less doping results in fewer photon absorption processes and thus less energetic helium ion characteristics. Again, at different time delays Δt , the height of each peak shifts. The He^{2+} and He^+ states become less frequent but a stark increase in He_2^+ and He_3^+ ion peaks is observed. It is likely that the ionization dynamics undergo a resonant type behavior, however, there are too few data points to support this hypothesis.

Summarizing, pristine He-droplets show few dynamics as the time delay Δt is varied and only singly-charged He^+ ions are measured. If the He-droplets are doped with xenon, doubly-charged He^{2+} ions are detected, the kinetic energy release is stronger and the time-of-flight data reveals dynamics that are comparable to atomic xenon, when the delay Δt is varied. As the xenon doping is increased, the presence of He^+ and

5. Results and discussion

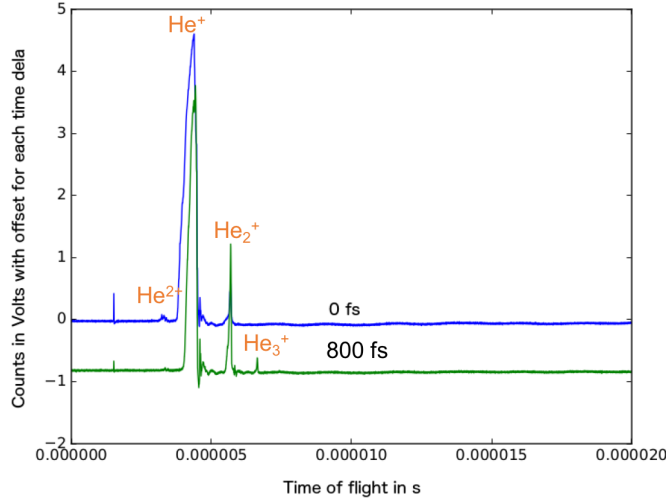


Figure 5.10.: Ion time-of-flight spectra of He-cluster with $r_{\text{He}} \approx 775$ nm radius and $\sim 0.06\%$ xenon doping. These weaker doped HeXe-clusters show a lower He-ion count and kinetic energy release due to overall less absorption from the lower xenon doping. However, He^{2+} , which indicates an energy transport from the xenon to the helium, is still observed.

He^{2+} ions is more frequent. This data suggests an ultrafast and efficient energy transfer from the xenon atoms to the helium atoms. Collisions could drive this transfer. The helium particles furthermore act as an electron reservoir. The initially photoionized xenon atoms recombine and only few xenon charge fragments are detected by the time-of-flight spectrometer. The underlying idea that a low-Z material acts as a electron supplier for the high-Z material has also been studied in [119].

5.4. Condensation of xenon in helium cluster: Plum-pudding type cluster

It is not well known how heterogeneous helium-xenon clusters form a core-shell system. As described in Section 2.2.2, the superfluid helium cluster picks up xenon atoms as it traverses the doping unit. The xenon atoms move unhindered in the superfluid helium and eventually the xenon atoms condense to energetically favorable cluster structures. [11] reports that at a doping level of 0.02 %, i.e., when there are 5000 more helium atoms than xenon atoms, multiple smaller clusters form and locate at vortexes within a rotating helium droplet. However, it is unknown how xenon atoms arrange in non-rotating

5.4. Condensation of xenon in helium cluster: Plum-pudding type cluster

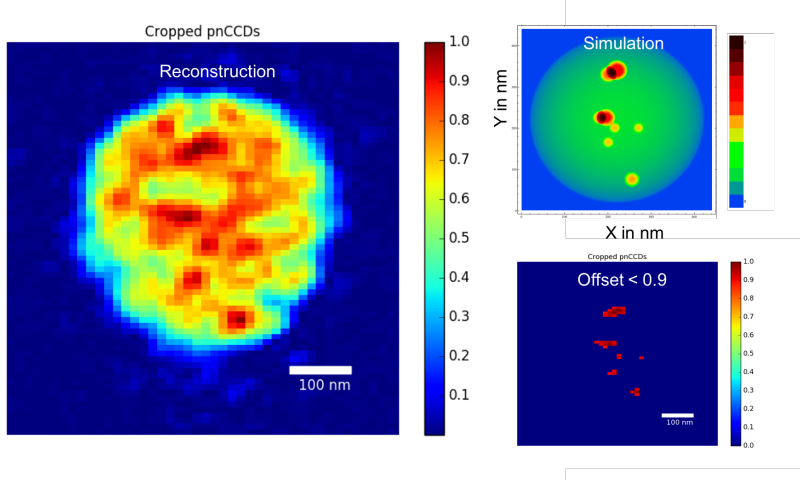


Figure 5.11.: Real-space reconstruction of a HeXe-cluster that has a radius of $r \approx 210$ nm and a Xe-doping level of $\sim 0.5\%$ (left). The electron density indicates a Xe-cluster arrangement of the plum-pudding few scatterers case discussed in Figure 5.12. The normalized intensity map is offset (bottom right image) and mimicked by 2D electron density simulations (top right image).

droplets and also at higher doping levels. The two competing hypotheses are; one, xenon atoms condense to one large cluster within a helium droplet; two, multiple smaller Xe-clusters form within a droplet. Let us call hypothesis two a *plum pudding core-shell system*¹ that we can further divide into a case of few and larger scatterers, or many and smaller scatterers.

Fortunately, single particle imaging is a direct structural measurement technique that allows us to investigate the actual structure of a HeXe-cluster. The left panel of Figure 5.11 shows a reconstruction of a HeXe-cluster that has a radius of $r \approx 210$ nm at a Xe-doping level of $\sim 0.5\%$. The reconstruction indicates a plum-pudding arrangement, where a few Xe-cluster (intense, dark red spots) appear randomly distributed within the He-droplet (less intense, green to orange area). The normalized intensity map from the reconstruction is offset to guide the eye to dense centers (bottom right panel) and these dense center can be used to reverse-engineer the electron density. The reverse engineered electron density can be Fourier transformed to yield a diffraction image that can be compared to data (top right panel). To verify the success of the HeXe-reconstruction, several core-shell arrangements are shown in Figure 5.12 along with their Fourier-space

¹The name plum-pudding model comes from J.J. Thomson's model of the atom in 1904 and has here been reused to describe the arrangement of atoms in heterogeneous (rare-gas) clusters.

5. Results and discussion

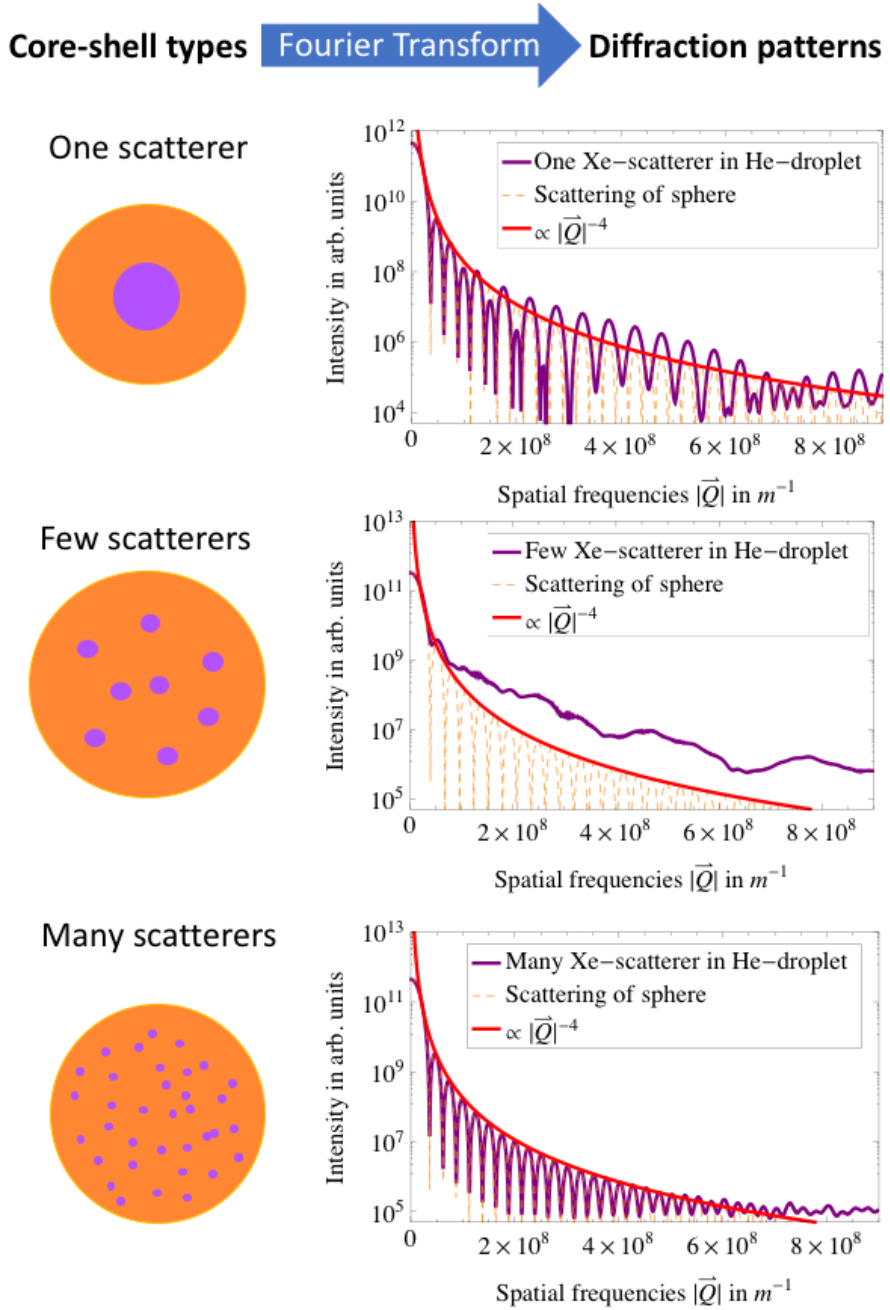


Figure 5.12.: Hypothetical arrangement of Xe-atoms in superfluid He-droplets (left) and corresponding 1D diffraction patterns (right). The He-droplet has a radius of ~ 125 nm and the Xe-doping level is $\sim 20\%$. The case of one xenon scattering center $N_{sc} = 1$ (top), few scatterers $N_{sc} = 8$ (middle), and many scatterers $N_{sc} = 100$ (bottom) are shown. The scattering pattern is dominated by the signal from the He-droplet at low spatial frequencies, but at large $|\vec{Q}|$ -values the signal is dominated by the Xe-clusters. This is mostly due to the size of the Xe-clusters; smaller scattering centers are resolved at larger scattering angles.

5.4. Condensation of xenon in helium cluster: Plum-pudding type cluster

representations in 1D. The shown He-droplet has a radius of $r \approx 125$ nm and a constant xenon doping level of $\sim 20\%$ and the figure shows an artistic representation of the simulated real-space core shell systems. These 2D-simulations are described in more detail in Section 4.4. In the illustration, it becomes obvious that the distribution of the xenon atoms within the He-droplet dominates the scattering pattern, which is due to the Xe-cluster density being ~ 25.8 times larger than the density of liquid He-droplets. The purple curve in the one-scatterer case consists of a large modulation in the diffraction image, which comes from the Xe-core and a small, more intense modulation that comes from the He-shell (similar to the orange, dashed line). At low spatial-frequencies, the He-droplet dominates the signal on the diffraction image and at large spatial-frequencies, the Xe-cluster influence is more prominent. Ultimately, this is related to the size of each cluster and the contributions of their spatial-frequencies to modulations in Fourier-space. In the few scatterers case, with $N_{sc} = 8$ scattering centers, the diffraction pattern (purple line) at low spatial-frequencies $|\vec{Q}|$ is still dominated by the He-shell and at high spatial-frequencies $|\vec{Q}|$ by the Xe-cores. However, the diffraction image appears to contain a more complex structure at large $|\vec{Q}|$ -values due to the delocalized scatterers. Also, the average scattering intensity is well above the envelope of the scattering of a sphere (red line) that has been fitted onto the zeroth diffraction order. The location of the few scattering centers plays a lesser role in the 1D projection of the 2D diffraction image, as long as the scattering centers are distributed throughout the He-droplet. In the many scatterers case, $N_{sc} = 100$ scattering centers are randomly distributed within the He-droplet. The Xe-clusters are significantly reduced in size to match the constant xenon doping level of $\sim 20\%$. For the outer shape, the small clusters appear similar to a constant electron density increase, which is visible at low-to-mid $|\vec{Q}|$ -values. Thus the scattering is practically identical to the scattering of a similar sized sphere (orange, dashed line). Only at large $|\vec{Q}|$ -values that reveal small structures do the Xe-scatterers start to dominate the signal, i.e., signal is above the envelope function of the scattering of the sphere.

To quantify and estimate the effect of Xe-cluster of a certain size contributing to the spatial-frequencies, we can make use of Abbe's criterion (4.9) and the wave vector definition (2.30). In vacuum, we can write down the minimal resolvable feature size d as

$$d = \frac{2\pi}{|\vec{Q}_r|}, \quad (5.3)$$

with $|\vec{Q}_r|$ being the point in reciprocal space, where the signal starts to be dominated by the smaller structures, here the Xe-clusters. We can relate the resolvable feature size d

5. Results and discussion

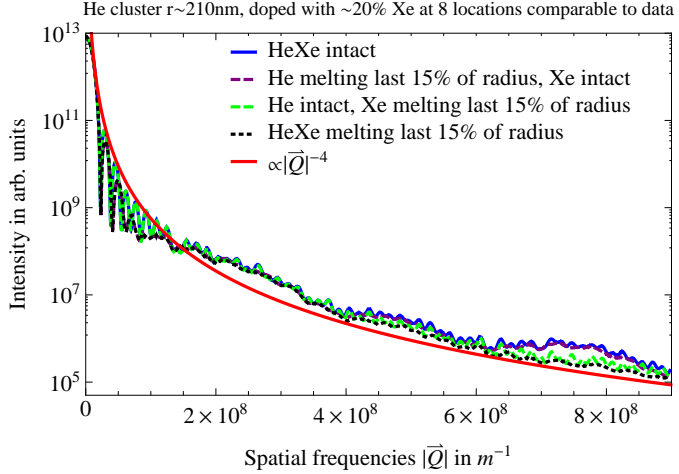


Figure 5.13.: Diffraction images from 2D electron density simulations that illustrate structural damage in HeXe-cluster. Electron densities as per Figure 5.11. In reciprocal space: The blue curve shows the helium droplet as well as Xe-clusters intact. The purple, dashed curve shows an expanding He-droplet, leaving the Xe-clusters intact. The green, dashed curve leaves the He-droplet intact but shows expanding He-clusters. The black, dashed curve shows both cluster types expanding. The red curve is the envelope of the scattering of a sphere fitted to the zeroth order. More in text.

to the radius r of the smaller spherical structures via $d \approx 2r$. This relation works well for the one-scatterer case $r_{\text{Xe}} \approx 15$ nm. However, as the structures become more complex one has more spatial frequency contributions from not only the smaller structures, i.e., the Xe-cluster, but also the space in between smaller structures and the space from the smaller structures to the boundary of the system, i.e., the He-droplet. Multiple smaller structures thus form a *superstructure* that appears larger than its individual components when estimated via Equation (5.3). For the plum-pudding cases the Xe-cluster form superstructures with the He-droplet. This superstructure is ~ 3 times larger in the few scatterers case and ~ 10 times larger in the many scatterers case than its individual, simulated Xe-cluster components.

5.5. Understanding structural damage in the plum-pudding type clusters

Figure 5.13 shows a diffraction pattern from the simulated plum-pudding type electron density shown in Figure 5.11 that illustrates radiation damage. As described in Section 4.4, the radiation damage is simulated via an expansion of the outer layers of a sphere. The He-droplet has a radius $r_{\text{He}} = 210 \text{ nm}$ and a strong Xe-doping of $\sim 20\%$ to illustrate the effects of structural damage. The blue, solid curve describes the scenario, where all spheres, i.e., clusters, are intact and no X-ray induced dynamics are present. The purple, dashed curve shows the case where the last 15% in units of the He-droplet radius r expand, but the Xe-cluster intact are intact. Conversely, the green, dashed curve shows the effect where the last 15% of the radius from Xe-clusters expand, but the He-shell stays intact. Lastly, all spheres are expanding in the last 15% of their radii. It can be clearly seen that the expansion of each cluster type effects either low spatial-frequencies when the He-droplet is expanding, or high spatial-frequencies when the (much smaller) Xe-cluster are expanding. The vast size difference of the Xe-clusters to the He-droplet, which are $r_{\text{Xe}} = (25, 22, 20, 18, 17, 14, 14, \text{ and } 13.5) \text{ nm}$ versus $r_{\text{He}} = 210 \text{ nm}$, allow a strict separation between the spatial frequency contributions from the He-droplet, e.g., the expanding shell, and the contributions from the Xe-clusters, e.g., the intact cores, in the diffraction pattern analysis.

These insights can be used to compare the 2D-simulations to the measured diffraction patterns. Figure 5.14 shows a HeXe-cluster reconstruction, a simulation and corresponding 1D diffraction pattern. This data has been taken at a time delay $\Delta t = 800 \text{ fs}$. The HeXe-cluster has a radius $r_{\text{He}} \approx 113 \text{ nm}$. The dense spots in the reconstruction have been simulated with nine Xe-cluster of radii $r_{\text{Xe}} = (4, 4, 4, 4, 3, 0.5, 0.5, 0.5, \text{ and } 0.5) \text{ nm}$, thus a $\sim 0.5\%$ Xe-doping. In the diffraction pattern, the scattering of a sphere with radius $r = 113 \text{ nm}$ (pink line) and its envelope (red line) are shown as a comparison. The yellow curve is a simulated diffraction pattern that shows an expanding He-droplet, where the last 7% of the shell is exponentially expanding, while the Xe-clusters stay intact. The green curve shows the simulated diffraction pattern, where the He-droplet is expanding at the last 7% of its radius and, to make the effect clear, 90% of the Xe-clusters outer radii are expanding. The simulations show a very good agreement with the expanding He-droplet at low spatial-frequencies $|\vec{Q}|$. At high frequencies, only the yellow curve that uses intact Xe-clusters in the simulation reproduces the scattering image well. It should be noted, however, that structural damage in the Xe-cluster is still possible, but may not

5. Results and discussion

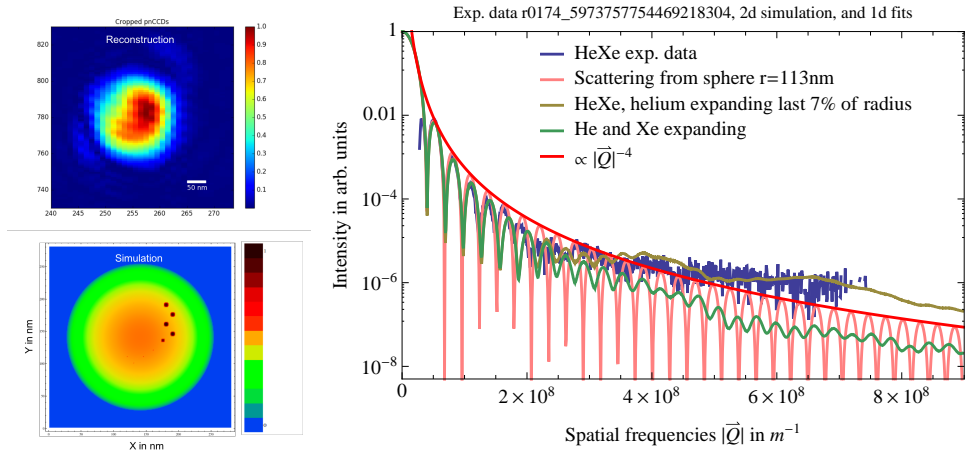


Figure 5.14.: 2D simulations fitted to real-space and Fourier-space data. HeXe-arrangement of 2D simulations (bottom left) matches recovered electron densities of a HeXe-cluster (top left). The diffraction pattern (right) shows the 1D-projected experimental data (blue curve) from the same HeXe-cluster with $r_{\text{He}} \approx 113$ nm. This HeXe-cluster was imaged at $\Delta t = 800$ fs and undergoes a nanoplasma transition. 2D simulations showcase several damage scenarios; in reciprocal space: Xe-cluster are intact (yellow curve) and Xe-cluster expanding (green curve). The simulations of an expanding He-droplet and intact Xe-cluster fit the experimental data best.

5.6. Sacrificial layers: Comparison of structural damage in He- and HeXe-cluster

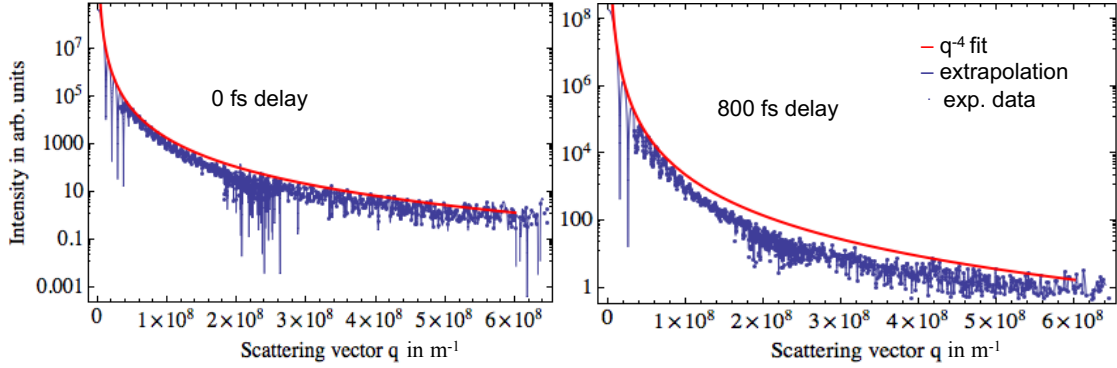


Figure 5.15.: Single-shot diffraction images of pristine He-droplets at various Δt spherically projected into 1D.

be detectable due to current resolution limitations.

5.6. Sacrificial layers: Comparison of structural damage in He- and HeXe-cluster

Single-shot diffraction images of He-droplets with radii $r_{\text{He}} \approx (379 \text{ and } 302) \text{ nm}$, at time delays $\Delta t = (0 \text{ and } 800) \text{ fs}$, respectively, are shown in Figure 5.15. For clarity, only the experimental data (blue points), spherical extrapolation at low $|\vec{Q}|$ -values (blue line) and the envelope of the spherical extrapolation function (red line) are shown. At $\Delta t = 0 \text{ fs}$, the local maxima of the experimental data agree well with the envelope function. This indicates an intact He-droplet, as shown in more detail in Section 5.1. As the time delay is varied to 800 fs, the diffraction pattern of the droplet shows that the local maxima between $|\vec{Q}| \approx (1 \text{ to } 4) \cdot 10^8 \text{ m}^{-1}$ are well below the envelope. As shown in section 5.5, this indicates damage.

Single-shot diffraction images of HeXe-cluster with radii $r_{\text{He}} \approx (116 \text{ and } 113.5) \text{ nm}$, at time delays $\Delta t = (0 \text{ and } 800) \text{ fs}$, respectively, are shown in Figure 5.16. The experimental data at $\Delta t = 800 \text{ fs}$ is the same as in Figure 5.14. The black dots are data points from the rear pnCCD and the blue dots are data points from the front pnCCD. The pink, dashed curve is the scattering from a sphere fitted to the first order of diffraction and the red curve is its envelope. Here, the differences in the diffraction images as the time delay Δt is varied from (0 to 800) fs provide as another indication that helium functions as a sacrificial layer in HeXe-clusters. At $\Delta t = 0 \text{ fs}$, the rear pnCCD data points agree well

5. Results and discussion

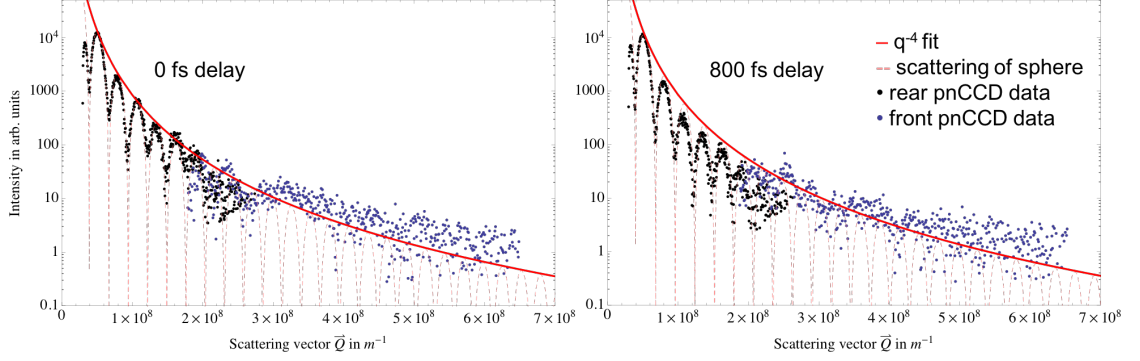


Figure 5.16.: Single-shot diffraction pattern of HeXe-cluster at time delays $\Delta t = (0$ and 800 fs. At $\Delta t = 0$ fs, the diffraction pattern follows the scattering pattern of a sphere at low spatial-frequencies but stays well above the envelope function $|\vec{Q}|^{-4}$ at high spatial-frequencies. At $\Delta t = 800$ fs, the scattering curve deviates from the scattering pattern of a sphere at low spatial frequencies indicating damage to the He-shell structure. At high spatial frequencies, the signal changes little compared to the $\Delta t = 0$ fs data indicating intact Xe-cluster, i.e., cores. This suggests that the He-droplet functions as sacrificial shell keeping the Xe-nanoparticles intact. More in text.

Measured scattering / expected scattering

For sample	At time delay Δt	
	0 fs	800 fs
Xe-cluster	0.91 ± 0.10	0.26 ± 0.10
He-droplet	0.89 ± 0.10	0.65 ± 0.10
HeXe-cluster	1	1.33 ± 0.30

Table 5.1.: Relative comparison of measured scattering versus expected scattering for Xe-, He- and HeXe-cluster at large spatial frequencies.

with the simulated scattering of a sphere, while the data points from the front detector lay well above the scattering envelope function of the sphere. As already discussed, at $\Delta t = 800$ fs the rear pnCCD data points do not agree well with the scattering of a sphere, indicating damage in the He-droplet. However, the blue data points appear to be similar, as in the $\Delta t = 0$ fs event.

A more quantitative comparison provides a challenge as each single-shot event has a certain uniqueness attributed to it. However, an attempt to compare the measured scattering versus expected scattering is made in the following and the results are summarized in Table 5.1. The diffraction pattern of a pristine He- or Xe-cluster can be easily com-

5.6. Sacrificial layers: Comparison of structural damage in He- and HeXe-cluster

pared to the scattering curve of a sphere $f(\vec{Q})$. Hence, we can introduce a function $h(\vec{Q})$ that interpolates between the data points of pristine He- and Xe-cluster. We can calculate a relative difference in the scattering at a certain time delay using the $\frac{\sum h(\vec{Q})}{\sum f(\vec{Q})}|_{\Delta t}^{\text{sample}}$. Since the effect is most visible at large $|\vec{Q}|$ -values, the functions h and f total between $(2.8 \text{ to } 6.4) \cdot 10^8 \text{ m}^{-1}$. For Xe- and He-clusters, we find values close to the expected scattering of similar sized spheres, thus is the measured scattering / expected scattering: $91\%|_{\Delta t=0\text{fs}}^{\text{Xe}}$ and $89\%|_{\Delta t=0\text{fs}}^{\text{He}}$. As already established, the actual scattering is reduced due to the nanoplasma expansion such that $26\%|_{\Delta t=800\text{fs}}^{\text{Xe}}$ and $65\%|_{\Delta t=800\text{fs}}^{\text{He}}$. The interpolating function seems to underestimate the actual scattering by $\sim 10\%$, which gives us an idea of the uncertainty of this estimate. Note that some sources of uncertainty, such as electronic noise, do make up for the underestimate of the interpolating function. HeXe-clusters cannot directly be compared to the scattering of a sphere. However, we may compare similar single-shot events at different time delays. The two single-shot events shown in Figure 5.16 represent similar data points, as they have the same incident beam variable I_0 in the $I_0|\vec{Q}|^{-4}$ fit and a size difference of only $\sim 2\%$ at the same source and doping conditions. When comparing the interpolating functions $h(\vec{Q})|_{\Delta t=800\text{fs}}^{\text{HeXe}}/h(\vec{Q})|_{\Delta t=0\text{fs}}^{\text{HeXe}}$ at different time delays Δt , 33% more scattering at large $|\vec{Q}|$ -values is measured. This leads to the conclusion that Xe-clusters exhibit no measurable damage despite the fact that damage in the He-droplet is visible at low spatial-frequencies $|\vec{Q}|$. The source of uncertainty in this estimation originates likely from a varying pickup pattern of Xe-atoms and the uncertainty must be at least $\sim 30\%$.

Synthesizing, we find a reduction in scattering intensity of $\sim 65\%$ in Xe-cluster and $\sim 24\%$ in He-droplets 800 fs after the beginning of the nanoplasma expansion. We attribute this change to damages in the sample². If Xe-clusters are embedded in a He-droplet, no damage is detected in Xe-clusters 800 fs after the nanosample has been pumped by LCLS, although the He-droplet shows damage. The He-droplet appears to shed atomic layers, which transports energy away from the Xe-clusters and enables them to exhibit no measurable damage patterns that were discussed in Section 5.5.

²The actual intensity loss must be larger due to the loss of electrons that is described in Figure 5.2.

6. Summary and outlook

For the present study, a novel, accelerator-based X-ray pump–X-ray probe technique was pioneered [51] and the new soft X-ray end-station LAMP was built and commissioned [129]. Using this new experimental setup, a coincident single particle imaging (SPI) and time-of-flight mass spectroscopy method was employed. Diffraction images of single, nanometer-sized aerosol particles were measured with thus-far unprecedented resolution. The successful combination of data from multiple detectors increased the “numerical aperture” and extended the dynamic range of the detector system. The developed coincident imaging and spectroscopy, X-ray pump–X-ray probe technique allowed the study of X-ray-induced dynamics on the few-ten-femtosecond timescale with a spatial resolution in diffractive imaging on the few nanometer lengthscale.

The work experimentally investigates the nanoplasma transition in rare-gas clusters. Single, nanometer-sized, rare-gas clusters, namely superfluid He-, solid Xe- and mixed HeXe-cluster are “pumped” with an X-ray pulse to undergo the phase transition to a nanoplasma. This transition is nothing different but the radiation damage that a typical biological sample receives due to the interaction with highly intense X-ray pulses. This transition is “probed” with another X-ray pulse at a later time delay. The here studied delay range is $\Delta t = (0 \text{ to } 800) \text{ fs}$. The coincident imaging and spectroscopy measuring method reveals that pristine He- and Xe-clusters become highly ionized and form a nanoplasma. The nanoplasma from Xe- and He-clusters exhibits stark radiation damage due to an expansion of the plasma. Xe-clusters, for example, undergo a radial expansion that shows in diffraction images at the first delay step at $\Delta t = 120 \text{ fs}$. Over the course of 800 fs, the radial expansion manifests in a $\sim 20\%$ increase of their initial average radius, which is $r \approx 61 \text{ nm}$. The hot Xe-nanoplasma is heated to electron temperatures of $\sim 125 \text{ eV}$. This thesis then shows that mixed HeXe-clusters, generated through the pickup-principle at doping levels up to 0.5 %¹, arrange in a *plum-pudding* configuration. In a plum-pudding cluster structure, multiple Xe-clusters condense within a larger He-droplet at different locations. When these mixed HeXe-clusters are pumped with intense

¹0.5 % as many xenon atoms as helium atoms.

X-rays from LCLS, Xe-clusters are the main absorbent of the radiation. But, data show that Xe-clusters are barely ionized and, at current resolution, appear to be undamaged inside the He-droplet. The weak absorbing helium experiences stark ionization and the He-droplet shows signs of radiation damage. This suggests that the He-droplet functions as a sacrificial shell around the Xe-particles. Two processes are identified that protect the Xe-clusters within the He-droplet; one, a kinetic energy transport from the Xe-clusters to the He-droplet; two, the He-droplet supplies electrons to the initially ionized Xe-particles, minimizing their ionization level.

The results of this work are beneficial to a variety of fields. First, the work from [15, 119] are expanded to include reconstructions of nanoparticles and a time-resolved X-ray pump–X-ray probe study. This study shows that a tamper layer can be used to inhibit effects of radiation damage in the diffraction pattern. This may be interesting for the SPI community, where it is foreseen that radiation damage will be a limiting factor in the ultimate achievable resolution [20]. Second, new and existing SPI data may make use of combining multiple detectors thereby increasing the resolution by a factor ~ 5 . Combined diffraction images unfold their full potential when combined with an EMC algorithm [170]. This allows an orientation and averaging of diffraction images, thus enabling a high-resolution 3D reconstruction of the sample while making use of the asymmetric detector geometry. Finally, the pioneered X-ray pump–X-ray probe technique can be and already has been extended to various other atomic and molecular physics experiments such as [30, 47, 53, 132, 177], allowing entirely new insights in previously unreachable regimes.

7. Appendix

7.1. Matlab code on spherical integrations

Excerpt of the Matlab code that has been used to reduce 2D diffraction images to 1D arrays with the intensity as a function of the scattering vector \vec{Q} .

```
%%% CENTER OF HIT
x_center=xLen/2; % Actually Y-center
y_center=yLen/2; % Actually X-center
for r=(1:1500)
    %looping over points
    for y=(1:yLen)
        for x=(1:xLen)
            %check if in circle
            if (x - x_center)^2 + (y - y_center)^2 < r^2
                %norm
                rnorm(r)=rnorm(r)+1;
                % testing for noise/photon
                if rearpnccd(x,y)>0
                    circleSum(r)=circleSum(r)+rearpnccd(x,y);
                end
            elseif (x - x_center)^2 + (y - y_center)^2 == r^2
                %norm
                rnorm(r)=rnorm(r)+(1/2);
                % testing for noise/photon
                if rearpnccd(x,y)>0
                    circleSum(r)=circleSum(r)+(rearpnccd(x,y)/2);
                end
            end
        end
    end
    if rnorm(r)==0
        rnorm(r)=1;
    end
    if r==1
        plotSum(r)=circleSum(r)/rnorm(r);
    elseif rnorm(r)-rnorm(r-1)>0
```

7.2. Python code on combining detectors

```

    plotSum( r )=( circleSum( r )-circleSum( r -1 ))/( rnorm( r )-rnorm( r -1 ));
else
    plotSum( r )=0;
end
end

```

7.2. Python code on combining detectors

Python code that has been used to combine pnCCD detectors.

```

# Imported Packages
import numpy as np

#### Gaps between front top and bottom pnCCD to middle of rear pnCCD
gapTop =231                         # In pixel
gapBot =252                          # In pixel

#### offset between rear and front pnCCDs
xShift ==-1                           # In pixel

////////////////// Things to adjust per run/experiment
pixelSizePnccd=75*10**-6             # Size of a pixel in meter.

distanceOfRearPnccd=0.74               # Distance IR to front pnCCD in meter
distanceOfFrontPnccd=0.36              # Distance IR to front pnCCD in meter
gainRearPnccd=1./64.                  # Detector gain multiplier
gainFrontPnccd=1.                      # Detector gain multiplier

scatteredWaveLength=1.5*10**-9        # Wavelength of photons in meter

pathToHDF5=                            # Adapt to your needs

#### Functions
# Phi - scattering angle
def PhiScatt(pixel , pixelSize , distanceToDetector):
    return np.arctan( pixel*pixelSize /distanceToDetector )

# Q-vector function
def qVector(pixel , pixelSize , distanceToDetector , waveLength):
    return 4.*np.pi*np.sin(PhiScatt(pixel , pixelSize ,
                                     distanceToDetector)/2)/waveLength

```

7. Appendix

```

### Reading intensity files ,
intFrontTop=    # Adapt to your needs
intRear=         # Adapt to your needs
intFrontBottom= # Adapt to your needs

### Intensity normalization and offset of electronic noise .
# Rear int. normalization
intRear=intRear*(1/gainRearPnccd)*(distanceOfRearPnccd**2)*
(1/distanceOfFrontPnccd**2)

# Offset
intRear[intRear<15*(1/gainRearPnccd)*(distanceOfRearPnccd**2)*
(1/distanceOfFrontPnccd**2)]=0.0
intFrontTop[intFrontTop<350]=0.0
intFrontBottom[intFrontBottom<350]=0.0

### Combining front detector
ztop=np.concatenate((intFrontTop,np.zeros
((gapTop+gapBot,1028)),intFrontBottom))

### Combining rear with front detector
# Creating pixel to Q-vector correlation vectors
yRear, xRear =np.ogrid[(-len(intRear))/2:(len(intRear))/2,
-(len(intRear[0]))/2:(len(intRear[0]))/2]

# To transform Q-values from rear pnCCD to front pnCCD pixel values
qDiv=qVector(1, pixelSize=pixelSizePnccd ,
              distanceToDetector=distanceOfFrontPnccd ,
              waveLength=scatteredWaveLength)

# Spanning Q-space
y_comb=len(ztop)/2
x_comb=len(ztop[0])/2

qyRear=np.round(qVector(yRear, pixelSize=pixelSizePnccd ,
                        distanceToDetector=distanceOfRearPnccd ,
                        waveLength=scatteredWaveLength)/qDiv).astype(int) + y_comb
qxRear=np.round(qVector(xRear, pixelSize=pixelSizePnccd ,
                        distanceToDetector=distanceOfRearPnccd ,
                        waveLength=scatteredWaveLength)/qDiv).astype(int) + x_comb + xShift

# Keep track of per pixel additions to create mean intensities
norm=np.zeros(ztop.shape)

```

7.2. Python code on combining detectors

```
# Iterating over the array, slow but works
it=np.nditer(intRear, flags=['multi_index'])

while not it.finished:
    # read pixel transform coordinates
    y_idx = qyRear[it.multi_index[0],0]
    x_idx = qxRear[0,it.multi_index[1]]

    # add intensities and add to norm
    ztop[y_idx,x_idx] += it[0]
    norm[y_idx,x_idx] += 1

    it.iternext()

# Corrections to norm so not 1/0, seems inefficient but is fast enough.
norm -= 1
norm[norm<0]=0
norm += 1

#### Combined mean intensities of front and rear detector.
ztop = ztop/norm
```

8. Bibliography

- [1] W. C. Röntgen, *The Nobel Prize in Physics*, The Nobel Foundation, “In recognition of the extraordinary services he has rendered by the discovery of the remarkable rays subsequently named after him”, 1901.
- [2] K. M. G. Siegbahn, *The Nobel Prize in Physics*, The Nobel Foundation, “For his discoveries and research in the field of X-ray spectroscopy”, 1924.
- [3] M. von Laue, *The Nobel Prize in Physics*, The Nobel Foundation, “For his discovery of the diffraction of X-rays by crystals”, 1914.
- [4] S. W. H. Bragg, and W. L. Bragg, *The Nobel Prize in Physics*, The Nobel Foundation, “For their services in the analysis of crystal structure by means of X-rays”, 1915.
- [5] W. a. Ackermann, G. Asova, V. Ayvazyan, A. Azima, N. Baboi, J. Bähr, V. Balandin, B. Beutner, A. Brandt, A. Bolzmann, et al., “Operation of a free-electron laser from the extreme ultraviolet to the water window,” *Nature Photonics* **1**, 336 (2007).
- [6] H. N. Chapman, P. Fromme, A. Barty, T. A. White, R. A. Kirian, A. Aquila, M. S. Hunter, J. Schulz, D. P. DePonte, U. Weierstall, et al., “Femtosecond x-ray protein nanocrystallography,” *Nature* **470**, 73 (2011).
- [7] P. Emma, R. Akre, J. Arthur, R. Bionta, C. Bostedt, J. Bozek, A. Brachmann, P. Bucksbaum, R. Coffee, F.-J. Decker, et al., “First lasing and operation of an ångstrom-wavelength free-electron laser,” *Nature Photonics* **4**, 641 (2010).
- [8] C. Bostedt, S. Boutet, D. M. Fritz, Z. Huang, H. J. Lee, H. T. Lemke, A. Robert, W. F. Schlotter, J. J. Turner, and G. J. Williams, “Linac coherent light source: the first five years,” *Reviews of Modern Physics* **88**, 015007 (2016).
- [9] H. N. Chapman, A. Barty, M. J. Bogan, S. Boutet, M. Frank, S. P. Hau-Riege, S. Marchesini, B. W. Woods, S. Bajt, W. H. Benner, et al., “Femtosecond diffractive imaging with a soft-x-ray free-electron laser,” *Nature Physics* **2**, 839 (2006).

- [10] M. M. Seibert, T. Ekeberg, F. R. Maia, M. Svenda, J. Andreasson, O. Jonsson, D. Odic, B. Iwan, A. Rocker, D. Westphal, et al., “Single mimivirus particles intercepted and imaged with an x-ray laser,” *Nature* **470**, 78 (2011).
- [11] L. F. Gomez, K. R. Ferguson, J. P. Cryan, C. Bacellar, R. M. P. Tanyag, C. Jones, S. Schorb, D. Anielski, A. Belkacem, C. Bernando, et al., “Shapes and vorticities of superfluid helium nanodroplets,” *Science* **345**, 906 (2014).
- [12] T. Ekeberg, M. Svenda, C. Abergel, F. R. Maia, V. Seltzer, J.-M. Claverie, M. Hantke, O. Jonsson, C. Nettelblad, G. van der Schot, et al., “Three-dimensional reconstruction of the giant mimivirus particle with an x-ray free-electron laser,” *Physical Review Letter* **114**, 098102 (2015).
- [13] I. Barke, H. Hartmann, D. Rupp, L. Flückiger, M. Sauppe, M. Adolph, S. Schorb, C. Bostedt, R. Treusch, C. Peltz, et al., “The 3D-architecture of individual free silver nanoparticles captured by X-ray scattering,” *Nature Communications* **6**, 6187 (2015).
- [14] L. Young, E. P. Kanter, B. Krassig, Y. Li, A. M. March, S. T. Pratt, R. Santra, S. H. Southworth, N. Rohringer, L. F. Dimauro, et al., “Femtosecond electronic response of atoms to ultra-intense x-rays,” *Nature* **466**, 56 (2010).
- [15] T. Gorkhover, S. Schorb, R. Coffee, M. Adolph, L. Foucar, D. Rupp, A. Aquila, J. D. Bozek, S. W. Epp, B. Erk, et al., “Femtosecond and nanometre visualization of structural dynamics in superheated nanoparticles,” *Nature Photonics* **10**, 93 (2016).
- [16] H. M. Quiney, and K. A. Nugent, “Biomolecular imaging and electronic damage using X-ray free-electron lasers,” *Nature Physics* **6**, 16 (2010).
- [17] J. Küpper, S. Stern, L. Holmegaard, F. Filsinger, A. Rouzée, A. Rudenko, P. Johnsson, A. V. Martin, M. Adolph, A. Aquila, et al., “X-ray diffraction from isolated and strongly aligned gas-phase molecules with a free-electron laser,” *Physical Review Letter* **112**, 083002 (2014).
- [18] S. P. Hau-Riege, R. a. London, and A. Szoke, “Dynamics of biological molecules irradiated by short x-ray pulses,” *Physical Review E* **69**, 051906 (2004).
- [19] S. P. Hau-Riege, S. Boutet, A. Barty, S. Bajt, M. J. Bogan, M. Frank, J. Andreasson, B. Iwan, M. M. Seibert, J. Hajdu, et al., “Sacrificial tamper slows down sample explosion in FLASH dffraction eperiments,” *Physical Review Letters* **104**, 1 (2010).

8. Bibliography

- [20] A. Aquila, A. Barty, C. Bostedt, S. Boutet, G. Carini, D. dePonte, P. Drell, S. Doniach, K. H. Downing, T. Earnest, et al., “The linac coherent light source single particle imaging road map,” *Structural Dynamics* **2**, 041701, 041701 (2015).
- [21] D. M. Mills, J. R. Hellwell, Å. Kvick, T. Ohta, I. A. Robinson, and A. Authier, “Report of the working group on synchrotron radiation nomenclature - Brightness, spectral brightness or brilliance?” *Journal of Synchrotron Radiation* **12**, 385 (2005).
- [22] J. Als-Nielsen, and D. McMorrow, *Elements of modern x-ray physics* (John Wiley & Sons, Mar. 2011).
- [23] S. N. A. Laboratory, *LCLS Aerial Overlay*, (2009) <https://www.flickr.com/photos/slaclab/8577624017/>.
- [24] P. H. Bucksbaum, R. Coffee, and N. Berah, “Chapter 5 - The First Atomic and Molecular Experiments at the Linac Coherent Light Source X-Ray Free Electron Laser,” in *Advances in atomic, molecular, and optical physics*, Vol. Volume 60 (Academic Press, 2011), pp. 239–289.
- [25] G. J. Williams, personal communication, June 16, 2016.
- [26] J. M. J. Madey, “Stimulated Emission of Bremsstrahlung in a Periodic Magnetic Field,” *Journal of Applied Physics* **42**, 1906 (1971).
- [27] A. Kondratenko, and E. L. Saldin, “Generation of coherent radiation by a relativistic electron beam in an undulator*,” *Particle Accelerators* **10**, 207 (1980).
- [28] R. Bonifacio, C. Pellegrini, and L. M. Narducci, “Collective instabilities and high-gain regime in a free electron laser,” *Optics Communications* **50**, 373 (1984).
- [29] M. Dell’Angela, T. Anniyev, M. Beye, R. Coffee, A. Fohlisch, J. Gladh, T. Katayama, S. Kaya, O. Krupin, J. LaRue, et al., “Real-Time Observation of Surface Bond Breaking with an X-ray Laser,” *Science* **339**, 1302 (2013).
- [30] A. Picón, C. S. Lehmann, C. Bostedt, A. Rudenko, A. Marinelli, T. Osipov, D. Rolles, N. Berah, C. Bomme, **M. Bucher**, et al., “Hetero-site-specific X-ray pump-probe spectroscopy for femtosecond intramolecular dynamics,” *Nature Communications* **7**, 11652 (2016).
- [31] N. Rohringer, D. Ryan, R. A. London, M. Purvis, F. Albert, J. Dunn, J. D. Bozek, C. Bostedt, A. Graf, R. Hill, et al., “Atomic inner-shell x-ray laser at 1.46 nanometres pumped by an x-ray free-electron laser,” *Nature* **481**, 488 (2012).

- [32] N. Berrah, L. Fang, B. Murphy, T. Osipov, K. Ueda, E. Kukk, R. Feifel, P. van der Meulen, P. Salen, H. T. Schmidt, et al., “Double-core-hole spectroscopy for chemical analysis with an intense x-ray femtosecond laser,” Proceedings of the National Academy of Sciences **108**, 16912 (2011).
- [33] T. Gorkhover, M. Adolph, D. Rupp, S. Schorb, S. W. Epp, B. Erk, L. Foucar, R. Hartmann, N. Kimmel, K. U. Kuhnel, et al., “Nanoplasma dynamics of single large xenon clusters irradiated with superintense x-ray pulses from the linac coherent light source free-electron laser,” Physical Review Letter **108**, 245005 (2012).
- [34] D. Rupp, “Ionization and plasma dynamics of single large xenon clusters in superintense xuv pulses,” Thesis (Technische Universität Berlin, 2013).
- [35] G. Brown, K. Halbach, J. Harris, and H. Winick, “Wiggler and undulator magnets — A review,” Nuclear Instruments and Methods in Physics Research **208**, 65 (1983).
- [36] G. P. Williams, ed., *X-ray data booklet* (Lawrence Berkeley National Laboratory, Apr. 2009).
- [37] Z. Huang, and K.-J. Kim, “Review of x-ray free-electron laser theory,” Physical Review Special Topics - Accelerators and Beams **10**, 034801 (2007).
- [38] K.-J. Kim, “Angular distribution of undulator power for an arbitrary deflection parameter K,” Nuclear Instruments and Methods in Physics Research Section A **246**, 67 (1986).
- [39] D. Rupp, *Ionization and plasma dynamics of single large xenon clusters in super-intense XUV pulses* (Springer, 2016).
- [40] **M. Bucher**, K. R. Ferguson, T. Gorkhover, and C. Bostedt, “A transmissive single-shot soft x-ray spectrometer,” Unpublished study on feasibility of a spectrometer that is based on photoemission., 2017.
- [41] K.-J. Kim, Y. Shvyd’ko, and S. Reiche, “A proposal for an x-ray free-electron laser oscillator with an energy-recovery linac,” Physical Review Letter **100**, 244802 (2008).
- [42] D. Ratner, R. Abela, J. Amann, C. Behrens, D. Bohler, G. Bouchard, C. Bostedt, M. Boyes, K. Chow, D. Cocco, et al., “Experimental demonstration of a soft x-ray self-seeded free-electron laser,” Physical Review Letter **114**, 054801 (2015).

8. Bibliography

- [43] L. B. Fletcher, H. J. Lee, T. Döppner, E. Galtier, B. Nagler, P. Heimann, C. Fortmann, S. LePape, T. Ma, M. Millot, et al., “Ultrabright x-ray laser scattering for dynamic warm dense matter physics,” *Nature Photonics* (2015) **10** . 1038 / nphoton.2015.41.
- [44] J. Amann, W. Berg, V. Blank, F. J. Decker, Y. Ding, P. Emma, Y. Feng, J. Frisch, D. Fritz, J. Hastings, et al., “Demonstration of self-seeding in a hard-x-ray free-electron laser,” *Nature Photonics* **6**, 693 (2012).
- [45] E. Allaria, R. Appio, L. Badano, W. A. Barletta, S. Bassanese, S. G. Biedron, A. Borga, E. Busetto, D. Castronovo, P. Cinquegrana, et al., “Highly coherent and stable pulses from the fermi seeded free-electron laser in the extreme ultraviolet,” *Nature Photonics* **6**, 699 (2012).
- [46] K. R. Ferguson, **M. Bucher**, T. Gorkhover, and C. Bostedt, “Absorption spectroscopy on CO and CO₂ molecules,” Unpublished study on CO and CO₂ molecules using an ion time of flight spectrometer., 2014.
- [47] V. Kimberg, A. Sanchez-Gonzalez, L. Mercadier, C. Weninger, A. Lutman, D. Ratner, R. Coffee, **M. Bucher**, M. Mucke, M. Agaker, et al., “Stimulated x-ray raman scattering - a critical assessment of the building block of nonlinear x-ray spectroscopy,” *Faraday Discussions* **194**, 305 (2016).
- [48] J. C. Castagna, B. Murphy, J. Bozek, and N. Berrah, “X-ray split and delay system for soft x-rays at lcls,” *Journal of Physics: Conference Series* **425**, 152021 (2013).
- [49] S. P. Moeller, M. Yabashi, and S. P. Hau-Riege, eds., *Mirror-based soft x-ray split-and-delay system for femtosecond pump-probe experiments at LCLS*, Vol. 8504 (SPIE Proceedings, Oct. 2012), p. 850409.
- [50] N. Berrah, L. Fang, B. F. Murphy, E. Kukk, T. Y. Osipov, R. Coffee, K. R. Ferguson, H. Xiong, J.-C. Castagna, V. S. Petrovic, et al., “Two mirror X-ray pulse split and delay instrument for femtosecond time resolved investigations at the LCLS free electron laser facility,” *Optics Express* **24**, 11768 (2016).
- [51] A. A. Lutman, R. Coffee, Y. Ding, Z. Huang, J. Krzywinski, T. Maxwell, M. Messerschmidt, and H. D. Nuhn, “Experimental demonstration of femtosecond two-color x-ray free-electron lasers,” *Physical Review Letter* **110**, 134801 (2013).
- [52] A. Marinelli, D. Ratner, A. Lutman, J. Turner, J. Welch, F.-J. Decker, H. Loos, C. Behrens, S. Gilevich, A. Miahnahri, et al., “High-intensity double-pulse x-ray free-electron laser,” *Nature Communications* **6**, 6369 (2015).

- [53] K. R. Ferguson, **M. Bucher**, T. Gorkhover, S. Boutet, H. Fukuzawa, J. E. Koglin, Y. Kumagai, A. Lutman, A. Marinelli, M. Messerschmidt, et al., “Transient lattice contraction in the solid-to-plasma transition,” *Science Advances* **2** (2016) 10 . 1126/sciadv.1500837.
- [54] C. E. Liekhus-Schmaltz, I. Tenney, T. Osipov, A. Sanchez-Gonzalez, N. Berrah, R. Boll, C. Bomme, C. Bostedt, J. D. Bozek, S. Carron, et al., “Ultrafast isomerization initiated by X-ray core ionization,” *Nature Communications* **6**, 8199 (2015).
- [55] P. Emma, K. Bane, M. Cornacchia, Z. Huang, H. Schlarb, G. Stupakov, and D. Walz, “Femtosecond and subfemtosecond x-ray pulses from a self-amplified spontaneous-emission-based free-electron laser,” *Physical Review Letter* **92**, 074801 (2004).
- [56] H. Haberland, ed., *Clusters of atoms and molecules*, Vol. 52, Chemical Physics (Springer, 1994), 444 pp.
- [57] W. Miehle, O. Kandler, T. Leisner, and O. Echt, “Mass spectrometric evidence for icosahedral structure in large rare gas clusters: Ar, Kr, Xe,” *The Journal of Chemical Physics* **91**, 5940 (1989).
- [58] B. W. Vandewaal, “Icosahedral, decahedral, fcc, and defect-fcc structural models for Ar-N clusters, n=500 - how plausible are they?” *The Journal of Chemical Physics* **98**, 4909 (1993).
- [59] N. V. Krainyukova, “The crystal structure problem in noble gas nanoclusters,” *Thin Solid Films* **515**, 1658 (2006).
- [60] D. Lippmann, W. C. Schieve, and C. Canestaro, “Clustering time dependence in molecular dynamics: A kinetic model,” *The Journal of Chemical Physics* **81**, 4969 (1984).
- [61] W.H. Zurek, and W.C. Schieve, “Multistep Clustering and Nucleation,” *Journal of Physical Chemistry* **84**, 1479 (1980).
- [62] J. M. Soler, N. García, O. Echt, K. Sattler, and E. Recknagel, “Microcluster growth: transition from successive monomer addition to coagulation,” *Physical Review Letter* **49**, 1857 (1982).
- [63] J. Farges, M. F. de Feraudy, B. Raoult, and G. Torchet, “Structure and temperature of rare gas clusters in a supersonic expansion,” *Surface Science* **106**, 95 (1981).
- [64] J. Gspann, “On the phase of metal clusters,” in Metal clusters, edited by F. Träger, and G. zu Putlitz, (Apr. 1986), pp. 43–45.

8. Bibliography

- [65] L. F. Gomez, E. Loginov, R. Sliter, and A. F. Vilesov, “Sizes of large He droplets,” Journal of Chemical Physics **135**, 154201 (2011).
- [66] D. R. Miller, *Free jet sources*, edited by G. Scoles, (Oxford University Press, Inc., 1988) Chap. 2, pp. 14–53.
- [67] I. Yamada, J. Matsuo, N. Toyoda, and A. Kirkpatrick, “Materials processing by gas cluster ion beams,” Materials Science and Engineering: R: Reports **34**, 231 (2001).
- [68] S. Schorb, “Size-dependent ultrafast ionization dynamics of nanoscale samples in intense femtosecond x-ray free-electron laser pulses,” Thesis (Technische Universität Berlin, 2012).
- [69] O. F. Hagena, “Cluster Formation in Expanding Supersonic Jets: Effect of Pressure, Temperature, Nozzle Size, and Test Gas,” The Journal of Chemical Physics **56**, 1793 (1972).
- [70] O. F. Hagena, “Nucleation and growth of clusters in expanding nozzle flows,” Surface Science **106**, 101 (1981).
- [71] O. F. Hagena, “Condensation in free jets: Comparison of rare gases and metals,” Zeitschrift für Physik D Atoms, Molecules and Clusters **4**, 291 (1987).
- [72] U. Buck, and R. Krohne, “Cluster size determination from diffractive He atom scattering,” The Journal of Chemical Physics **105**, 5408 (1996).
- [73] F. Dorchies, F. Blasco, T. Caillaud, J. Stevefelt, C. Stenz, A. S. Boldarev, and V. A. Gasilov, “Spatial distribution of cluster size and density in supersonic jets as targets for intense laser pulses,” Physical Review A **68**, 023201 (2003).
- [74] O. F. Hagena, “Cluster ion sources (invited),” Review of Scientific Instruments **63**, 2374 (1992).
- [75] A. M. Bush, A. J. Bell, J. G. Frey, and J.-M. Mestdagh, “Rayleigh Scattering of Laser and Synchrotron Radiation from Pulsed Free Jets of Ar n and (N₂O)_n Clusters,” The Journal of Physical Chemistry A **102**, 6457 (1998).
- [76] D. Rupp, M. Adolph, L. Flückiger, T. Gorkhov, J. P. Müller, M. Müller, M. Sauppe, D. Wolter, S. Schorb, R. Treusch, et al., “Generation and structure of extremely large clusters in pulsed jets,” Journal of Chemical Physics **141**, 044306 (2014).
- [77] L. S. Bartell, “Diffraction studies of clusters generated in supersonic flow,” Chemical Reviews **86**, 491 (1986).

- [78] D. Rupp, M. Adolph, T. Gorkhover, S. Schorb, D. Wolter, R. Hartmann, N. Kimmel, C. Reich, T. Feigl, A. R. B. de Castro, et al., “Identification of twinned gas phase clusters by single-shot scattering with intense soft x-ray pulses,” *New Journal of Physics* **14**, 055016 (2012).
- [79] T. E. Gough, M. Mengel, P. a. Rowntree, and G. Scoles, “Infrared spectroscopy at the surface of clusters: SF 6 on Ar,” *The Journal of Chemical Physics* **83**, 4958 (1985).
- [80] K. R. Ferguson, “Crystal structure determinations of xenon nanoparticles and x-ray induced transient lattice contraction in the solid-to-plasma transition,” PhD thesis (Stanford University, Feb. 2016).
- [81] R. Pugliese, and G. Paolucci, *Atomic calculation of photoionization cross-sections and asymmetry parameters*, (Aug. 2016) <https://vuo.elettra.eu/services/elements/WebElements.html>.
- [82] J. Yeh, and I. Lindau, “Atomic subshell photoionization cross sections and asymmetry parameters: $1 \leq Z \leq 103$,” *Atomic Data and Nuclear Data Tables* **32**, 1 (1985).
- [83] J.-J. Yeh, *Atomic calculation of photoionization cross-sections and asymmetry parameters* (Gordon & Breach Science Publ.; AT&T Bell Laboratories, 1993).
- [84] R. D. Cowan, *The theory of atomic structure and spectra* (University of California Press, Sept. 11, 1981), 650 pp.
- [85] W. Demtröder, *Experimentalphysik 3: Atome, Moleküle und Festkörper* (Springer, 2005).
- [86] **M. Bucher**, K. R. Ferguson, G. T., and B. C., “The LAMP endstation in the AMO instrument at the Linac Coherent Light Source,” Unpublished study on the LAMP endstation with focus on the pnCCD detectors., 2017.
- [87] B. Rudek, S. K. Son, L. Foucar, S. W. Epp, B. Erk, R. Hartmann, M. Adolph, R. Andritschke, A. Aquila, N. Berrah, et al., “Ultra-efficient ionization of heavy atoms by intense x-ray free-electron laser pulses,” *Nature Photonics* **6**, 858 (2012).
- [88] M. Krause, F. Stevie, L. Lewis, T. Carlson, and W. Moddeman, “Multiple excitation of neon by photon and electron impact,” *Physics Letters A* **31**, 81 (1970).
- [89] V. Schmidt, “Auger spectrum of neon following 1s ionization,” in *Electron spectrometry of atoms using synchrotron radiation:* (Cambridge University Press, May 1997), pp. 73–94.

8. Bibliography

- [90] C. Buth, R. Santra, and L. S. Cederbaum, “Impact of interatomic electronic decay processes on Xe 4d hole decay in the xenon fluorides,” *The Journal of Chemical Physics* **119**, 10575 (2003).
- [91] J. P. Briand, P. Chevallier, M. Tavernier, and J. P. Rozet, “Observation of K Hypersatellites and KL Satellites in the X-Ray Spectrum of Doubly K-Ionized Gallium,” *Physical Review Letter* **27**, 777 (1971).
- [92] D. Coster, and R. D. L. Kronig, “New type of Auger effect and its influence on the X-ray spectrum,” *Physica* **2**, 13 (1935).
- [93] M. M. Y. Berezin, and S. Achilefu, “Fluorescence Lifetime Measurements and Biological Imaging,” *Chemical Reviews* **110**, 2641 (2011).
- [94] A. Guinier, and G. Fournet, *Small-angle scattering of x-rays* (John Wiley & Sons, New York, 1955).
- [95] I. A. Vartanyants, and I. K. Robinson, “Partial coherence effects on the imaging of small crystals using coherent x-ray diffraction,” *Journal of Physics: Condensed Matter* **13**, 10593 (2001).
- [96] P. J. Ho, personal communication, Aug. 2016.
- [97] D. Attwood, *Soft X-Rays and Extreme Ultraviolet Radiation: Principles and Applications* (Cambridge University Press, 2012).
- [98] T. Fennel, K.-H. Meiwes-Broer, J. Tiggesbaumker, P.-G. Reinhard, P. M. Dinh, and E. Suraud, “Laser-driven nonlinear cluster dynamics,” *Reviews of Modern Physics* **82**, 1793 (2010).
- [99] M. Arbeiter, and T. Fennel, “Rare-gas clusters in intense VUV, XUV and soft x-ray pulses: signatures of the transition from nanoplasma-driven cluster expansion to Coulomb explosion in ion and electron spectra,” *New Journal of Physics* **13**, 053022 (2011).
- [100] C. Bostedt, M. Adolph, E. Eremina, M. Hoener, D. Rupp, S. Schorb, H. Thomas, A. R. B. de Castro, and T. Möller, “Clusters in intense FLASH pulses: ultrafast ionization dynamics and electron emission studied with spectroscopic and scattering techniques,” *Journal of Physics B* **43**, 194011 (2010).
- [101] H. Wabnitz, L. Bittner, a. R. B. de Castro, R. Döhrmann, P. Gürtler, T. Laarmann, W. Laasch, J. Schulz, A. Swiderski, K. von Haeften, et al., “Multiple ionization of atom clusters by intense soft X-rays from a free-electron laser.,” *Nature* **420**, 482 (2002).

- [102] T. Laarmann, A. R. B. De Castro, P. Gürler, W. Laasch, J. Schulz, H. Wabnitz, and T. Möller, “Interaction of Argon clusters with intense VUV-laser radiation: The role of electronic structure in the energy-deposition process,” Physical Review Letters **92**, 143401 (2004).
- [103] C. Bostedt, H. Thomas, M. Hoener, E. Eremina, T. Fennel, K. H. Meiwes-Broer, H. Wabnitz, M. Kuhlmann, E. Plönjes, K. Tiedtke, et al., “Multistep ionization of argon clusters in intense femtosecond extreme ultraviolet pulses,” Physical Review Letters **100**, 12 (2008).
- [104] T. Laarmann, M. Rusek, H. Wabnitz, J. Schulz, A. R. B. De Castro, P. Gürler, W. Laasch, and T. Möller, “Emission of thermally activated electrons from rare gas clusters irradiated with intense VUV light pulses from a free electron laser,” Physical Review Letters **95**, 3 (2005).
- [105] C. Bostedt, H. Thomas, M. Hoener, T. Möller, U. Saalmann, I. Georgescu, C. Gnadtke, and J. M. Rost, “Fast electrons from multi-electron dynamics in xenon clusters induced by inner-shell ionization,” New Journal of Physics **12** (2010) 10. 1088/1367-2630/12/8/083004.
- [106] M. Arbeiter, and T. Fennel, “Ionization heating in rare-gas clusters under intense XUV laser pulses,” Physical Review A **82**, 1 (2010).
- [107] M. Lezius, S. Dobosz, D. Normand, and M. Schmidt, “Explosion Dynamics of Rare Gas Clusters in Strong Laser Fields,” Physical Review Letters **80**, 261 (1998).
- [108] E. Springate, N. Hay, J. W. G. Tisch, M. B. Mason, T. Ditmire, M. H. R. Hutchinson, and J. P. Marangos, “Explosion of atomic clusters irradiated by high-intensity laser pulses: scaling of ion energies with cluster and laser parameters,” Physical Review A **61**, 063201 (2000).
- [109] R. Neutze, R. Wouts, D. van der Spoel, E. Weckert, and J. Hajdu, “Potential for biomolecular imaging with femtosecond x-ray pulses,” Nature **406**, 752 (2000).
- [110] C. Bostedt, E. Eremina, D. Rupp, M. Adolph, H. Thomas, M. Hoener, A. R. de Castro, J. Tiggesbaumker, K. H. Meiwes-Broer, T. Laarmann, et al., “Ultrafast x-ray scattering of xenon nanoparticles: imaging transient states of matter,” Physical Review Letter **108**, 093401 (2012).
- [111] D. Rupp, L. Flückiger, M. Adolph, T. Gorkhover, M. Krikunova, J. P. Müller, M. Müller, T. Oelze, Y. Ovcharenko, B. Röben, et al., “Recombination-enhanced surface expansion of clusters in intense soft x-ray laser pulses,” Physical Review Letter **117**, 153401 (2016).

8. Bibliography

- [112] S. Schorb, T. Gorkhover, J. P. Cryan, J. M. Glownia, M. R. Bionta, R. N. Coffee, B. Erk, R. Boll, C. Schmidt, D. Rolles, et al., “X-ray–optical cross-correlator for gas-phase experiments at the linac coherent light source free-electron laser,” *Applied Physics Letters* **100**, 121107 (2012).
- [113] S. P. Hau-Riege, and H. N. Chapman, “Modeling of the damage dynamics of nanospheres exposed to x-ray free-electron-laser radiation,” *Physical Review E* **77**, 1 (2008).
- [114] C. Peltz, C. Varin, T. Brabec, and T. Fennel, “Time-resolved x-ray imaging of anisotropic nanoplasma expansion,” *Physical Review Letters* **113**, 1 (2014).
- [115] S. P. Hau-Riege, R. A. London, G. Huldt, and H. N. Chapman, “Pulse requirements for x-ray diffraction imaging of single biological molecules,” *Physical Review E* **71**, 061919 (2005).
- [116] G. Huldt, A. Szőke, and J. Hajdu, “Diffraction imaging of single particles and biomolecules,” *Journal of Structural Biology* **144**, 219 (2003).
- [117] S. P. Hau-Riege, R. A. London, H. N. Chapman, A. Szoke, and N. Timneanu, “Encapsulation and diffraction-pattern-correction methods to reduce the effect of damage in x-ray diffraction imaging of single biological molecules,” *Physical Review Letter* **98**, 198302 (2007).
- [118] F. R. N. C. Maia, T. Ekeberg, N. Timneanu, D. van der Spoel, and J. Hajdu, “Structural variability and the incoherent addition of scattered intensities in single-particle diffraction,” *Physical Review E* **80**, 031905 (2009).
- [119] M. Hoener, C. Bostedt, H. Thomas, L. Landt, E. Eremina, H. Wabnitz, T. Laarmann, R. Treusch, A. R. B. De Castro, and T. Möller, “Charge recombination in soft x-ray laser produced nanoplasmas,” *Journal of Physics B* **41**, 181001 (2008).
- [120] K. von Haeften, A. R. B. de Castro, M. Joppien, L. Moussavizadeh, R. von Pietrowski, and T. Möller, “Discrete visible luminescence of helium atoms and molecules desorbing from helium clusters: the role of electronic, vibrational, and rotational energy transfer,” *Physical Review Letters* **78**, 4371 (1997).
- [121] R. von Pietrowski, K. von Haeften, T. Laarmann, T. Möller, L. Museur, and A. V. Kanaev, “Electronic and geometric structure of doped rare-gas clusters: surface, site and size effects studied with luminescence spectroscopy,” *The European Physical Journal D* **38**, 323 (2006).
- [122] F. Stienkemeier, and K. K. Lehmann, “Spectroscopy and dynamics in helium nanodroplets,” *Journal of Physics B* **39**, R127 (2006).

- [123] D. Buchta, S. R. Krishnan, N. B. Brauer, M. Drabbels, P. O’Keeffe, M. Devetta, M. Di Fraia, C. Callegari, R. Richter, M. Coreno, et al., “Charge Transfer and Penning Ionization of Dopants in or on Helium Nanodroplets Exposed to EUV Radiation,” *The Journal of Physical Chemistry A* **117**, 4394 (2013).
- [124] A. Mikaberidze, U. Saalmann, and J. M. Rost, “Energy absorption of xenon clusters in helium nanodroplets under strong laser pulses,” *Physical Review A* **77**, 041201 (2008).
- [125] J. .-E. Augustin, A. M. Boyarski, M. Breidenbach, F. Bulos, J. T. Dakin, G. J. Feldman, G. E. Fischer, D. Fryberger, G. Hanson, B. Jean-Marie, et al., “Discovery of a Narrow Resonance in $e^+ - e^-$ Annihilation,” *Physical Review Letter* **33**, 1406 (1974).
- [126] R. E. Taylor, *Nucleon form factors above 6 GeV*, tech. rep. (Sept. 1967).
- [127] M. L. Perl, G. S. Abrams, A. M. Boyarski, M. Breidenbach, D. D. Briggs, F. Bulos, W. Chinowsky, J. T. Dakin, G. J. Feldman, C. E. Friedberg, et al., “Evidence for Anomalous Lepton Production in $e^+ - e^-$ Annihilation,” *Physical Review Letter* **35**, 1489 (1975).
- [128] C. Bostedt, J. D. Bozek, P. H. Bucksbaum, R. N. Coffee, J. B. Hastings, Z. Huang, R. W. Lee, S. Schorb, J. N. Corlett, P. Denes, et al., “Ultra-fast and ultra-intense x-ray sciences: first results from the linac coherent light source free-electron laser,” *Journal of Physics B* **46**, 164003 (2013).
- [129] K. R. Ferguson, **M. Bucher**, J. D. Bozek, S. Carron, J.-C. Castagna, R. Coffee, G. I. Curiel, M. Holmes, J. Krzywinski, M. Messerschmidt, et al., “The Atomic, Molecular and Optical Science instrument at the Linac Coherent Light Source,” *Journal of Synchrotron Radiation* **22**, 492 (2015).
- [130] A. Munke, J. Andreasson, A. Aquila, S. Awel, K. Ayyer, A. Barty, R. J. Bean, P. Berntsen, J. Bielecki, S. Boutet, et al., “Coherent diffraction of single Rice Dwarf virus particles using hard X-rays at the Linac Coherent Light Source,” *Scientific Data* **3**, 160064 (2016).
- [131] A. Sanchez-Gonzalez, T. R. Barillot, R. J. Squibb, P. Kolorenč, M. Agaker, V. Averbukh, M. J. Bearpark, C. Bostedt, J. D. Bozek, S. Bruce, et al., “Auger electron and photoabsorption spectra of glycine in the vicinity of the oxygen K-edge measured with an X-FEL,” *Journal of Physics B* **48**, 234004 (2015).

8. Bibliography

- [132] C. S. Lehmann, A. Picon, C. Bostedt, A. Rudenko, A. Marinelli, D. Moonshiram, T. Osipov, D. Rolles, N. Berrah, C. Bomme, et al., “Ultrafast x-ray-induced nuclear dynamics in diatomic molecules using femtosecond x-ray-pump-x-ray-probe spectroscopy,” *Physical Review A* **94**, 1 (2016).
- [133] M. J. MacDonald, T. Gorkhover, B. Bachmann, **M. Bucher**, S. Carron, R. N. Coffee, R. P. Drake, K. R. Ferguson, L. B. Fletcher, E. J. Gamboa, et al., “Measurement of high-dynamic range x-ray Thomson scattering spectra for the characterization of nano-plasmas at LCLS,” *Review of Scientific Instruments* **87**, 11E709 (2016).
- [134] E. Gamboa, B. Bachmann, D. Kraus, M. MacDonald, **M. Bucher**, S. Carron, R. Coffee, R. Drake, J. Emig, K. Ferguson, et al., “Dual crystal x-ray spectrometer at 1.8 keV for high repetition-rate single-photon counting spectroscopy experiments,” *Journal of Instrumentation* **11**, P08015 (2016).
- [135] C. Bernado, **M. Bucher**, C. Bostedt, and O. Gessner, “Shapes of rotating superfluid helium nanodroplets,” *Physical Review B* (2017).
- [136] J. D. Bozek, “AMO instrumentation for the LCLS x-ray FEL,” *The European Physical Journal Special Topics* **169**, 129 (2009).
- [137] C. Behrens, F. J. Decker, Y. Ding, V. A. Dolgashev, J. Frisch, Z. Huang, P. Krejcik, H. Loos, A. Lutman, T. J. Maxwell, et al., “Few-femtosecond time-resolved measurements of x-ray free-electron lasers,” *Nature Communications* **5**, 3762 (2014).
- [138] S. Moeller, J. Arthur, A. Brachmann, R. Coffee, F. J. Decker, Y. Ding, D. Dowell, S. Edstrom, P. Emma, Y. Feng, et al., “beamlines and diagnostics at LCLS,” *Nuclear Instruments and Methods in Physics Research Section A* **635**, S6 (2011).
- [139] S. P. Hau-Riege, R. M. Bionta, D. D. Ryutov, R. A. London, E. Ables, K. I. Kishiyama, S. Shen, M. A. McKernan, D. H. McMahon, M. Messerschmidt, et al., “Near-Ultraviolet Luminescence of N₂ Irradiated by Short X-Ray Pulses,” *Physical Review Letter* **105**, 043003 (2010).
- [140] W. F. Schlatter, J. J. Turner, M. Rowen, P. Heimann, M. Holmes, O. Krupin, M. Messerschmidt, S. Moeller, J. Krzywinski, R. Soufli, et al., “The soft x-ray instrument for materials studies at the linac coherent light source x-ray free-electron laser,” *Review of Scientific Instruments* **83**, 043107 (2012).

- [141] R. Souffli, M. Fernández-Perea, S. L. Baker, J. C. Robinson, E. M. Gullikson, P. Heimann, V. V. Yashchuk, W. R. McKinney, W. F. Schlotter, and M. Rowen, “Development and calibration of mirrors and gratings for the soft x-ray materials science beamline at the Linac Coherent Light Source free-electron laser,” *Applied Optics* **51**, 2118 (2012).
- [142] G. L. Dakovski, P. Heimann, M. Holmes, O. Krupin, M. P. Minitti, A. Mitra, S. Moeller, M. Rowen, W. F. Schlotter, and J. J. Turner, “The soft x-ray research instrument at the linac coherent light source,” *Journal of Synchrotron Radiation* **22**, 498 (2015).
- [143] L. Strüder, S. Epp, D. Rolles, R. Hartmann, P. Holl, G. Lutz, H. Soltau, R. Eckart, C. Reich, K. Heinzinger, et al., “Large-format, high-speed, x-ray pnccds combined with electron and ion imaging spectrometers in a multipurpose chamber for experiments at 4th generation light sources,” *Nuclear Instruments and Methods in Physics Research Section A* **614**, 483 (2010).
- [144] J. Turner, personal communication, June 2, 2016.
- [145] P. Kirkpatrick, and A. V. Baez, “Formation of optical images by X-rays.,” *Journal of the Optical Society of America* **38**, 766 (1948).
- [146] L. Juha, S. Bajt, and R. A. London, eds., *X-ray laser-induced ablation of lead compounds*, Vol. 8077, Damage to VUV, EUV, and X-ray Optics III 807718 (SPIE Proceedings, May 2011), p. 807718.
- [147] J. Chalupský, P. Bohacek, V. Hajkova, S. P. Hau-Riege, P. A. Heimann, L. Juha, J. Krzywinski, M. Messerschmidt, S. P. Moeller, B. Nagler, et al., “Comparing different approaches to characterization of focused x-ray laser beams,” *Nuclear Instruments and Methods in Physics Research Section A* **631**, 130 (2011).
- [148] P. Krejcik, S. Allison, R. Akre, K. Kotturi, M. Browne, J. Dusatko, W. White, D. Rogind, A. Gromme, L. Dalesio, et al., *Timing and Synchronization at the LCLS*, tech. rep. SLAC-PUB-12593, presented at 8th European Workshop on Beam Diagnostics and Instrumentation for Particle Accelerators (SLAC National Accelerator Laboratory, June 2007).
- [149] P. J. Ho, C. Bostedt, S. Schorb, and L. Young, “Theoretical Tracking of Resonance-Enhanced Multiple Ionization Pathways in X-ray Free-Electron Laser Pulses,” *Physical Review Letter* **113**, 253001 (2014).
- [150] T. Osipov, personal communication, Aug. 13, 2013.

8. Bibliography

- [151] G. Doumy, C. Roedig, S.-K. Son, C. I. Blaga, A. D. DiChiara, R. Santra, N. Berrah, C. Bostedt, J. D. Bozek, P. H. Bucksbaum, et al., “Nonlinear atomic response to intense ultrashort x rays,” *Physical Review Letter* **106**, 083002 (2011).
- [152] B. Henke, E. Gullikson, and J. Davis, *X-Ray interactions: photoabsorption, scattering, transmission, and reflection at E = 50-30,000 eV, Z = 1-92*, 1993.
- [153] J. M. Liu, “Simple technique for measurements of pulsed gaussian-beam spot sizes,” *Optics Letters* **7**, 196 (1982).
- [154] J. Chalupský, J. Krzywinski, L. Juha, V. Hájková, J. Cihelka, T. Burian, L. Vyšín, J. Gaudin, A. Gleeson, M. Jurek, et al., “Spot size characterization of focused non-Gaussian X-ray laser beams,” *Optics Express* **18**, 27836 (2010).
- [155] J. Chalupský, T. Burian, V. Hájková, L. Juha, T. Polcar, J. Gaudin, M. Nagasano, R. Sobierajski, M. Yabashi, and J. Krzywinski, “Fluence scan: an unexplored property of a laser beam.,” *Optics express* **21**, 26363 (2013).
- [156] A. Perazzo, *LCLS Data Analysis Strategy*, tech. rep. (SLAC National Accelerator Laboratory, Feb. 2016).
- [157] D. Damiani, M. Dubrovin, I. Gaponenko, W. Kroeger, T. J. Lane, A. Mitra, C. P. O’Grady, A. Salnikov, A. Sanchez-Gonzalez, D. Schneider, et al., “Linac Coherent Light Source data analysis using psana,” *Journal of Applied Crystallography* **49**, 672 (2016).
- [158] M. F. Hantke, and L. Foucar, personal communication, June 2016.
- [159] Y. Bruck, and L. Sodin, “On the ambiguity of the image reconstruction problem,” *Optics Communications* **30**, 304 (1979).
- [160] R. Bates, *Fourier phase problems are uniquely solvable in more than one dimension, 1. Underlying theory*, Stuttgart, 1981.
- [161] D. Sayre, “Some implications of a theorem due to Shannon,” *Acta Crystallographica* **5**, 843 (1952).
- [162] G. J. Williams, H. M. Quiney, A. G. Peele, and K. A. Nugent, “Fresnel coherent diffractive imaging: treatment and analysis of data,” *New Journal of Physics* **12**, 035020 (2010).
- [163] J. R. Fienup, “Phase retrieval algorithms: a comparison,” *Applied Optics* **21**, 2758 (1982).
- [164] J. R. Fienup, “Reconstruction of an object from the modulus of its Fourier transform,” *Optics letters* **3**, 27 (1978).

- [165] F. R. N. C. Maia, T. Ekeberg, D. van der Spoel, and J. Hajdu, “Hawk: the image reconstruction package for coherent X-ray diffractive imaging,” *Journal of Applied Crystallography* **43**, 1535 (2010).
- [166] M. M. Seibert, S. Boutet, M. Svenda, T. Ekeberg, F. R. N. C. Maia, M. J. Bogan, N. Tîmneanu, A. Barty, S. Hau-Riege, C. Caleman, et al., “Femtosecond diffractive imaging of biological cells,” *Journal of Physics B* **43**, 194015 (2010).
- [167] F. R. Maia, “The coherent x-ray imaging data bank,” *Nature Methods* **9**, 854 (2012).
- [168] D. R. Luke, “Relaxed averaged alternating reflections for diffraction imaging,” *Inverse Problems* **21**, 37 (2005).
- [169] M. F. Hantke, D. Hasse, F. R. N. C. Maia, T. Ekeberg, K. John, M. Svenda, N. D. Loh, A. V. Martin, N. Timneanu, D. S. D. Larsson, et al., “High-throughput imaging of heterogeneous cell organelles with an X-ray laser,” *Nature Photonics* **8**, 943 (2014).
- [170] N. T. D. Loh, and V. Elser, “Reconstruction algorithm for single-particle diffraction imaging experiments,” *Physical Review E* **80**, 1 (2009).
- [171] A. Technologies, ed., *Agilent acqiris programmer’s guide*, XZ130, Agilent Technologies Inc. (June 2007).
- [172] S. Schütte, and U. Buck, “Strong fragmentation of large rare gas clusters by high energy electron impact,” *International Journal of Mass Spectrometry* **220**, 183 (2002).
- [173] T. Gorkhover, “Ultrafast light induced dynamics of xe nanoparticles studies with a combination of intense infrared and x-ray pulses,” Thesis (Technische Universität Berlin, 2014).
- [174] S. Schorb, D. Rupp, M. L. Swiggers, R. N. Coffee, M. Messerschmidt, G. Williams, J. D. Bozek, S.-I. Wada, O. Kornilov, T. Möller, et al., “Size-dependent ultrafast ionization dynamics of nanoscale samples in intense femtosecond X-ray free-electron-laser pulses,” *Physical Review Letter* **108**, 233401 (2012).
- [175] B. Schütte, T. Oelze, M. Krikunova, M. Arbeiter, T. Fennel, M. J. J. Vrakking, and A. Rouzée, “Real-time fragmentation dynamics of clusters ionized by intense extreme-ultraviolet pulses,” *Journal of Physics B* **48**, 185101 (2015).
- [176] B. Schütte, F. Campi, M. Arbeiter, T. Fennel, M. J. J. Vrakking, and A. Rouzée, “Tracing Electron-Ion Recombination in Nanoplasmas Produced by Extreme-Ultraviolet Irradiation of Rare-Gas Clusters,” *Physical Review Letters* **112**, 253401 (2014).

8. Bibliography

- [177] A. Al-Haddad, A. Picon, **M. Bucher**, G. Doumy, A. Luttmann, A. Marinelli, T. Maxwell, S. Moeller, D. Ray, T. Osipov, et al., “Working title: Measurement of the ultrafast electronic reconfiguration in atomic CO after ionization,” unpublished work, 2016-2017.

A. Publikationsliste

- C. Bernado, **M. Bucher**, C. Bostedt, and O. Gessner, “Shapes of rotating superfluid helium nanodroplets,” *Physical Review B* (2017).
- K. R. Ferguson, **M. Bucher**, T. Gorkhover, S. Boutet, H. Fukuzawa, J. E. Koglin, Y. Kumagai, A. Lutman, A. Marinelli, M. Messerschmidt, K. Nagaya, J. Turner, K. Ueda, G. J. Williams, P. H. Bucksbaum, and C. Bostedt, “Transient lattice contraction in the solid-to-plasma transition,” *Science Advances* **2** (2016) 10.1126/sciadv.1500837.
- E. Gamboa, B. Bachmann, D. Kraus, M. MacDonald, **M. Bucher**, S. Carron, R. Coffee, R. Drake, J. Emig, K. Ferguson, S. Glenzer, T. Gorkhover, S. Hau-Riege, J. Krzywinski, A. Levitan, K.-H. Meiwes-Broer, T. Osipov, T. Pardini, C. Peltz, S. Skruszewicz, C. Bostedt, T. Fennel, and T. Döppner, “Dual crystal x-ray spectrometer at 1.8 keV for high repetition-rate single-photon counting spectroscopy experiments,” *Journal of Instrumentation* **11**, P08015 (2016).
- V. Kimberg, A. Sanchez-Gonzalez, L. Mercadier, C. Weninger, A. Lutman, D. Ratner, R. Coffee, **M. Bucher**, M. Mucke, M. Agaker, C. Sathe, C. Bostedt, J. Nordgren, J. E. Rubensson, and N. Rohringer, “Stimulated x-ray raman scattering - a critical assessment of the building block of nonlinear x-ray spectroscopy,” *Faraday Discussions* **194**, 305 (2016).
- C. S. Lehmann, A. Picon, C. Bostedt, A. Rudenko, A. Marinelli, D. Moonshiram, T. Osipov, D. Rolles, N. Berrah, C. Bomme, **M. Bucher**, G. Doumy, B. Erk, K. R. Ferguson, T. Gorkhover, P. J. Ho, E. P. Kanter, B. Krässig, J. Krzywinski, A. A. Lutman, A. M. March, D. Ray, L. Young, S. T. Pratt, and S. H. Southworth, “Ultrafast x-ray-induced nuclear dynamics in diatomic molecules using femtosecond x-ray-pump-x-ray-probe spectroscopy,” *Physical Review A* **94**, 1 (2016).
- M. J. MacDonald, T. Gorkhover, B. Bachmann, **M. Bucher**, S. Carron, R. N. Coffee, R. P. Drake, K. R. Ferguson, L. B. Fletcher, E. J. Gamboa, S. H. Glenzer, S. Göde, S. P. Hau-Riege, D. Kraus, J. Krzywinski, A. L. Levitan, K.-H. Meiwes-Broer, C. P. O’Grady, T. Osipov, T. Pardini, C. Peltz, S. Skruszewicz, M. Swiggers, C. Bostedt, T. Fennel, and T. Döppner, “Measurement of high-dynamic range x-ray Thomson scat-

A. Publikationsliste

- tering spectra for the characterization of nano-plasmas at LCLS,” Review of Scientific Instruments **87**, 11E709 (2016).
- A. Munke, J. Andreasson, A. Aquila, S. Awel, K. Ayyer, A. Barty, R. J. Bean, P. Berntsen, J. Bielecki, S. Boutet, **M. Bucher**, H. N. Chapman, B. J. Daurer, H. DeMirci, V. Elser, P. Fromme, J. Hajdu, M. F. Hantke, A. Higashiura, B. G. Hogue, A. Hosseiniزاده, Y. Kim, R. A. Kirian, H. K. Reddy, T.-Y. Lan, D. S. Larsson, H. Liu, N. D. Loh, F. R. Maia, A. P. Mancuso, K. Mühlig, A. Nakagawa, D. Nam, G. Nelson, C. Nettelblad, K. Okamoto, A. Ourmazd, M. Rose, G. van der Schot, P. Schwander, M. M. Seibert, J. A. Sellberg, R. G. Sierra, C. Song, M. Svenda, N. Timneanu, I. A. Vartanyants, D. Westphal, M. O. Wiedorn, G. J. Williams, P. L. Xavier, C. H. Yoon, and J. Zook, “Coherent diffraction of single Rice Dwarf virus particles using hard X-rays at the Linac Coherent Light Source,” Scientific Data **3**, 160064 (2016).
- A. Picón, C. S. Lehmann, C. Bostedt, A. Rudenko, A. Marinelli, T. Osipov, D. Rolles, N. Berrah, C. Bomme, **M. Bucher**, G. Doumy, B. Erk, K. R. Ferguson, T. Gorkhover, P. J. Ho, E. P. Kanter, B. Krässig, J. Krzywinski, A. A. Lutman, A. M. March, D. Moonshiram, D. Ray, L. Young, S. T. Pratt, and S. H. Southworth, “Hetero-site-specific X-ray pump-probe spectroscopy for femtosecond intramolecular dynamics,” Nature Communications **7**, 11652 (2016).
- K. R. Ferguson, **M. Bucher**, J. D. Bozek, S. Carron, J.-C. Castagna, R. Coffee, G. I. Curiel, M. Holmes, J. Krzywinski, M. Messerschmidt, M. Miniti, A. Mitra, S. Moeller, P. Noonan, T. Osipov, S. Schorb, M. Swiggers, A. Wallace, J. Yin, and C. Bostedt, “The Atomic, Molecular and Optical Science instrument at the Linac Coherent Light Source,” Journal of Synchrotron Radiation **22**, 492 (2015).
- M. A. Alcalde, **M. Bucher**, C. Emery, and T. Brandes, “Thermal phase transitions for Dicke-type models in the ultrastrong-coupling limit,” Physical Review E **86**, 4 (2012).

B. Eidestattliche Versicherung

Hiermit erkläre ich, dass ich die vorliegende Arbeit selbständig und eigenhändig, sowie ohne unerlaubte fremde Hilfe und ausschließlich unter Verwendung der aufgeführten Quellen und Hilfsmittel angefertigt habe.

Chicago, den 29. Januar 2017

Maximilian Jakob Bucher

Ort, Datum

C. Acknowledgment

This has to be written.

D